Title

Exciton Effects in Hybrid Organic-Inorganic Perovskites and One-Dimensional Organic Metal Halide Hybrids

Author

McClintock, Luke

Publication Date

2023

Peer reviewed|Thesis/dissertation

Exciton Effects in Hybrid Organic-Inorganic Perovskites and One-Dimensional Organic Metal Halide Hybrids

By

LUKE MCCLINTOCK

DISSERTATION

Submitted in partial satisfaction of the requirements for the degree of

DOCTOR OF PHILOSOPHY

in

Physics and Astronomy

in the

OFFICE OF GRADUATE STUDIES

of the

UNIVERSITY OF CALIFORNIA

DAVIS

Approved:

_____

Dong Yu, Chair

_____

Nicholas Curro

_____

Gergely Zimanyi

Committee in Charge

2023

Table of Contents

Acknowledgements

To start, I would like to deeply thank my graduate research advisor, **Prof. Dong Yu**, a mentor of great patience and intellect. He not only tolerated my strange hair styles and mannerisms for years on end, but also continuously supported me academically and financially. Working with his research team gave me the chance to hone my skills as a condensed matter experimentalist and allowed me to make my mark on the world of photovoltaics.

Next, the following list of people is much too short to fully represent all the help I have received over the last decade of study, but I will do my best to name most of the major players, in a pseudo-chronological order. My heartfelt thanks to...

The Mighty Doc Scheirer - Who inspired me to pursue a deeper level of scientific investigation and correctly recognized that my plutonium-fun-facts-icosahedron was better than everyone else's.

Prof. David Hilton - Who literally kick-started my career in physics and forced me, in the best way possible, to reach for higher and higher academic goals. I could not have made it this far without his support, whether he thinks so or not.

Dr. Dmitry Yarotski and Dr. Rohit Prasankumar - Who, across both undergraduate and graduate scenarios, made time in their absurdly busy schedules to meet with me regularly, give me copious amounts of life and career advice, and assist me in my experiments at the national laboratory.

Dr. Yasen Hou, Dr. Rui Xiao, Clark Travaglini, Bob Wang, Tony Song, and Clinton Taylor Gibson - Who assisted me in any number of experimental, psychological, emotional, and mathematical conundrums. They have all been incredible labmates, colleagues, and friends.

Dr. Prashant Padmanabhan, Dr. Jake Pettine, Dr. Long Yuan, and Dr. Nick Sirica - Who regularly assisted and mentored me during my LANL fellowship, and will

hopefully continue to do so during my postdoc. I will strive to continue learning from them as best I can.

The collective Davis Physics Squad and the Birmingham Horsemen (you all know who you are) - Who gamed with me on Wednesday nights, slayed dragons with me on Saturday mornings, and traveled with me to cities around the country just to lose in Pokémon tournaments - You're all irreplaceable friends and you helped keep me near some semblance of 'sane.'

Stephanie, Randy, and Zack Lawson - Who helped me in times of immense stress and let me eat all of their leftovers while watching Battleship, featuring Rihanna.

Finally, enormous thanks go to my wife **Caitlin Lawson**, my father **Dr. James McClintock**, my mother **Ferne McClintock**, my sister **Jamie McClintock**, and my best man **Jacob Mayhew** - Who were there for me every single step of the arduous way. I would not be here, or anywhere for that matter, without them.

List of Acronyms

1D = One-dimensional

BSE = Bethe-Salpeter Equation

CBM = Conduction band minimum

CINT = Center for Integrated Nano-Technology

CNM2 = Center of Nano and Micro-Manufacturing

CW = Continuous wave

DBR = Distributed Bragg reflector

DFT = Density-functional theory

DMEDA = N,N'-dimethylethylenediammonium

EBIC = Electron beam induced current

EQE = External quantum efficiency

FE = Free exciton

FET = Field-effect transistor

FTO = Fluorine-doped tin oxide

FWHM = Full width half max

HOIP = Hybrid organic-inorganic perovskite

ISC = Intersystem crossing

LANL = Los Alamos National Laboratory

LED = Light emitting diode

LO = Longitudinal optical

MA = Methylammonium

ND = Neutral density

OMHH = Organic metal halide hybrid

PBE = Perdew-Burke-Ernzerhof

PCE = Power conversion efficiency

PDOS = Partial density of states

PEM = Photo-elastic modulator

PL = Photoluminescence

RPA = Random phase approximation

RPP = Ruddlesden-Popper halide perovskite

SCF = Self-consistent field

SEM = Scanning electron microscopy

SRH = Shockley-Read-Hall

SNL = Sandia National Laboratory

SPCM = Scanning photocurrent microscopy

STE = Self-trapped exciton

T-REx = Time-Resolved Experimental

TRPC = Time-resolved photocurrent

TRPL = Time-resolved photoluminescence

UV = Ultraviolet

VBM = Valence band maximum

XRD = X-ray diffraction

Abstract

We investigated temperature and gate-dependent photogenerated carrier diffusion in single-crystal microstructures of the hybrid organic-inorganic perovskite (HOIP) methylammonium lead trihalide ($MAPbX_3$, where X = I, Br) via scanning photocurrent microscopy (SPCM). In both materials, carrier diffusion lengths (L_D) were found to increase abruptly across the tetragonal to orthorhombic phase transition, coincident with an abrupt increase in exciton binding energy (E_B), and reached over 100 μm by 80 K. Combined with relatively short carrier lifetimes, the low temperature L_D measurements implied an enormous carrier mobility ($\sim 10^4\ Vs/cm^2$) in both materials, too high in fact to be typical electron or hole diffusion. Thus, we attributed this fascinating behavior to fast, efficient transport of charge-neutral excitons, where the dipolar nature of the excitons massively reduces their optical phonon scattering, allowing them to diffuse unhindered through these materials.

We also discovered the ability to tune the low temperature exciton diffusion via an applied gate voltage (V_G). Depending on the material, as well as the sign and magnitude of V_G, L_D could be increased or decreased by a significant margin. In addition, $MAPbBr_3$'s intrinsically larger E_B made this value directly observable through photocurrent spectroscopy. The measured E_B values were temperature-dependent (E_B increased as T decreased) with the sharpest change occurring at the low temperature phase transition.

Finally, we branched out from our HOIP studies to investigate polarization-dependent anisotropic photoluminescence of self-trapped excitons (STEs) in the one-dimensional (1D) organic metal halide hybrid (OMHH) $C_4N_2H_{14}PbBr_4$. 1D materials can exhibit strongly anisotropic optical properties and highly efficient light emission, making them promising candidates for novel photodetection and lighting applications. We discovered that the sample emission intensity can shift between being maximum under parallel-to-1D chain versus perpendicular-to-1D chain excitation, depending on the excitation wavelength (λ_{EX}). We attributed this λ_{EX}-dependent emission to fast surface recombination, supported by first-principles calculations of optical absorption and a fast emission decay component seen with time-resolved photoluminescence (TRPL) only when absorption was located near the surface.

Chapter 1. Introduction

The severity with which the world needs continued advancement in clean energy generation and efficient energy consumption cannot be understated. It is infuriatingly difficult for the individual to feel as though they can make a difference, when faced with uncaring mega-corporations that pump out 99% of the emissions that are rapidly destroying our planet. That being said, scientists hold a special kind of power against these destructive entities, in that we have the opportunity to change the fundamentals that the rest of the economic world must rely on, in order to keep making their profits. If solar energy becomes the cheapest way to power your country, legislation that favors it will follow suit. Reliance on oil and gas will fade away. Similarly, if better, higher efficiency lighting technology is developed for our smart-phones and televisions, Samsung and Apple get to advertise a longer battery life and cleaner picture. Higher efficiency means less heat lost to the environment, and when one pulls even a little heat waste away from 100 billion screens and appliances, the effect is significant. I have spent these last 6 years working to advance the fields of solar energy and efficient light generation through fundamental materials research, with specific interest in how excitons affect various optoelectronic semiconductor properties. The two main classes of materials I have studied, hybrid organic-inorganic perovskites and organic metal halide hybrids, are among the vanguard of hopeful next-generation materials to be applied to the ongoing energy crisis. Let's start with some background...

1.1 Materials Background

1.1.1 Hybrid Organic-Inorganic Perovskites

Over the last decade, hybrid organic-inorganic perovskites (HOIPs), including methylammonium lead halide $MAPbX_3$ (M=CH_3, A=NH_3, and X=Cl, Br, I), have garnered global attention due to their incredible potential for cost-effective solar energy conversion,[1] [2] with photovoltaic conversion efficiencies (PCE) now reaching over 25%.[3] [4] These hybrid compounds, with the general chemical structure ABX_3 (**Figure 1.1**), are highly versatile; the

cations and anions may be interchanged and/or mixed to achieve an adjustable bandgap, higher stability, and a lower defect density.[2] [5] [6] $MAPbX_3$ in particular can exist in three different, temperature-dependent structural phases as well, each displaying unique optoelectronic properties. $MAPbI_3$, for example, is cubic (Pm-3m) above 330 K, tetragonal (I4/mcm) between 330 K and 160 K, and orthorhombic (Pnma) below 160 K.[7] $MAPbBr_3$ follows a very similar trend to $MAPbI_3$, just with slightly shifted critical temperatures, and $MAPbCl_3$ too goes through the same three phases, but only exists in the tetragonal phase for a few degrees (173 K - 179 K).[8] These HOIPs can be solution-processed at near room temperature, thus enabling inexpensive and large-scale production of solar panels and instilling the dream of being able to print photovoltaic devices like newspaper. HOIPs also show promise in light emitting diode (LED), indoor light harvesting, and laser applications.[3] [9]

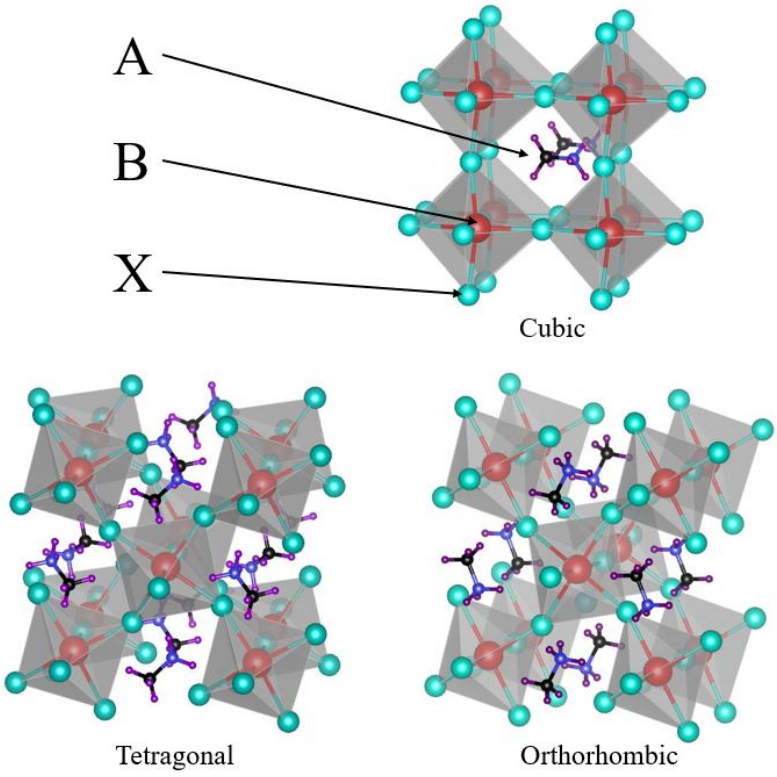

Figure 1.1: Temperature-dependent structural phases of $MAPbI_3$. The A, B, and X sites represent the central cation (can be organic or inorganic), metal ion, and halide sites, respectively. For $MAPbI_3$ in particular, A = $CH_3NH_3^+$ (black spheres = carbon, blue spheres = nitrogen, purple spheres = hydrogen), B = Pb^{+2}, and X = I^-.

The high PCE (now competitive with silicon photovoltaics) in these vanguard HOIPs has been attributed to several apparent factors, including an ideal bandgap (about 1.5 eV for $MAPbI_3$), high absorption coefficients, reasonably high electron/hole mobilities (10 - 100 cm^2/Vs), unexpectedly long carrier lifetimes (100 ns - 100 μs), and large carrier diffusion lengths (100 nm - 175 μm),[10] [11] [12] even with relatively high defect densities as expected from the low-temperature solution growth processes. HOIPs have been shown to have a soft lattice with a Young's modulus approximately 10 times lower than common inorganic semiconductors.[13] As a result of the highly polarizable lattice, a charge carrier can effectively form a large polaron with a diameter much larger than the unit cell size.[14] Large polarons in HOIPs may account for the unique optoelectronic properties of the materials, including electric field screening, defect tolerance, slow hot carrier cooling, and moderate charge carrier mobility.[15] [16] However, large polarons are but one of many theories as to why these compounds display such special properties, in particular, the long carrier lifetimes and large diffusion lengths. While several possible mechanisms such as local polar fluctuations,[17] polaron formation,[15] spin-orbital coupling,[18] ion migration,[19] and ferroelectricity[20] have been proposed to understand these unique HOIP properties, the true origins are still under intense debate. The intrinsic material physics happening here is rich with information that could be crucial to fundamental semiconductor science and the development of better photovoltaic technologies, including new HOIP-based solar cell architectures.

1.1.2 1-Dimensional Organic Metal Halide Hybrids

Charge carriers and excitons (described in detail below) in materials with weak electric field screening can interact strongly with the crystal lattice and be heavily dressed by phonons via a self-trapping mechanism, leading to lower mobility and large Stokes shifts.[21] [22] [23] Strong couplings between excitons and specific phonon modes have been directly observed, such as those seen in stack-engineered $WSe_2/MoSe_2$ heterojunction photodiodes,[24] monolayer WSe_2,[25] various forms of boron nitride,[26] [27] and chiral one-dimensional (1D) lead-free

hybrid metal halides.[28] Similar to HOIPS, perovskite-related materials such as organic metal halide hybrids (OMHHs) have become one of the most promising classes of photoactive materials being studied, with potential applications in solar energy, photodetection, LEDs, and lasers.[29] [30] As a result of the formation of self-trapped excitons (STEs; discussed in detail in Section 1.2.2) with high binding energies, low-dimensional OMHHs exhibit bright white-light emission.[21] [31] [32] [33] It has also been demonstrated that the photoluminescence (PL) quantum yields can be further enhanced to up to 90% by high pressure.[34] This broadband and efficient emission, typically occurring only in materials with sufficient electron-phonon coupling, shows promise for uses in solid-state lighting devices.

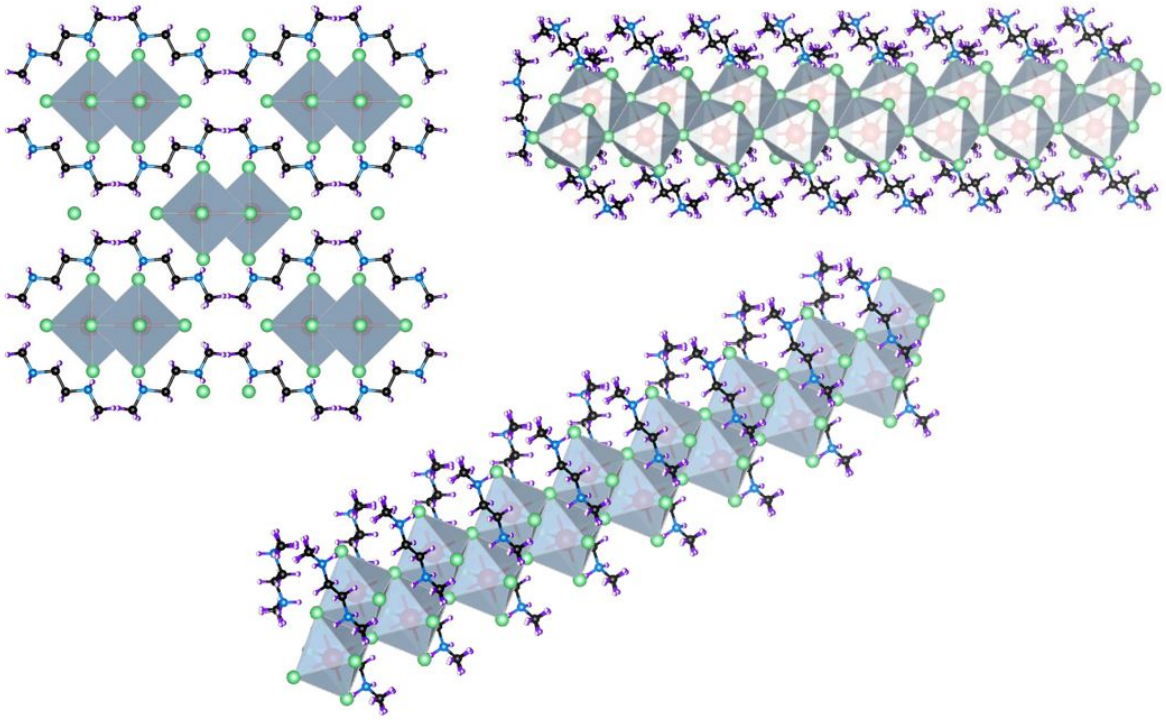

Figure 1.2: Example of a relevant 1D structure ($C_4N_2H_{14}PbBr_4$): quantum wires composed of metal halide octahedra (green and red spheres), wrapped by organic cations (black, blue, and purple spheres). The exact atomic constituents of this structure are discussed in Chapter 4.

1D OMHHs consist of corner, edge, and face-sharing metal halide octahedra which create 1D networks, glued together by organic cations (**Figure 1.2**).[29] These 1D networks can form in zigzag, linear, bilinear, and tubular shapes. The bulk material is considered an assem-

bly of core-shell nano-structures, where the positively charged cations form the shell and the negatively charged octahedra chains form the core. Such materials can exhibit strong optical anisotropy, offering additional exciting application opportunities.[29] Fluorescence anisotropy has been observed in stretch-oriented poly(p–phenylenevinylene) (PPV),[35] J-aggregates of thiacarbocyanine dyes,[36] and 1D halogen-bridged Pt chains.[37] Anisotropic optical properties have been observed in single-walled carbon nanotubes through spectroscopic ellipsometry measurements.[38] Linear dichroism conversion has been reported in quasi-1D hexagonal perovskite chalcogenide $BaTiS_3$,[39] and the introduction of chiral cations in 1D perovskites has enabled direct detection of circularly polarized light.[40] A theoretical first-principles study confirmed the formation of STEs in 1D OMHHs $C_4N_2H_{14}PbX_4$ and established a polarization-luminescence relationship.[41] Experimentally, linear polarization-dependent PL has been reported in $C_4N_2H_{14}PbI_4$,[42] but how the PL polarization relates to the 1D metal halide chains of this 1D OMHH is not reported. Another 1D OMHH, $C_3H_{10}NPbI_3$,[43] has been reported to show PL linearly polarized along the 1D chain. However, this work applied only a fixed photoexcitation energy close to the exciton resonance energy of the 1D perovskite material and did not provide a clear physical mechanism accounting for the observed anisotropy. It is crucial to understand the fundamental mechanisms in anisotropic excitons and the self-trapping process in 1D OMHHs to advance their potential broad applications in lighting, polarization optics, sensing, imaging, and communication technologies.

1.2 Excitons

1.2.1 Excitons in Semiconductors

Excitons are electron-hole pair quasi-particles bound by Coulombic attraction, and they have major impacts on the optoelectronic properties of semiconductor materials.[44] When a semiconducting material absorbs a photon with sufficient energy (greater than the bandgap energy), a negatively charged electron is excited from the valence band to the

conduction band, leaving behind a positively charged hole (essentially the absence of the electron). The excited electron is drawn toward the hole through the electrostatic force, but is simultaneously repelled by other surrounding electrons, leading to an equilibrium state of the correlated electron and hole - an exciton. Consequently, the exciton state in this electrostatic balance is lower in energy than either of the free charge species, and can therefore be favorable under certain conditions. Excitons can be thought of as elementary excitations of condensed matter that have the ability to transport energy without transporting net charge.[45] Fundamental research on these charge-neutral quasi-particles has revealed rich and intriguing physics. Under the right conditions, excitons can form more complicated quasi-particle structures, such as trions, biexcitons,[46] [47] exciton polarons,[48] and exciton polaritons.[49] Excitons can also undergo a gas-liquid phase transition[50] and condense into an electronic insulator or a superfluidic quantum state.[51] [52] Analogous to charged polarons (electrons or holes interacting with the charged lattice surrounding them), excitons may also interact with the crystal lattice and form polaronic excitons. The phonon-scattering of charged carriers in semiconductors is typically believed to be dominated by longitudinal optical phonons, but the scattering of exciton polarons is fundamentally different from charged polarons and is poorly understood.[53] Exciton effects are manifold; they can greatly influence the optical properties of semiconducting materials by creating a resonant optical absorption and they can simultaneously directly affect carrier transport behavior and charge extraction.

Practically, excitons are often given negative connotation in solar energy harvesting due to their presumed short diffusion lengths and direct influence on conversion efficiencies; an exciton must 'break' into its constituent charged pieces in order for them to be collected as photocurrent. In polymer, organic, and low-dimensional semiconductors, excitons dominate over free charge carriers upon photoexcitation at room temperature, due to their associated exciton binding energy E_B values being larger than the average thermal energy k_BT. As a consequence, one of the limiting factors for power conversion efficiency in organic solar cells

is the rather short (on the order of 10 nm) exciton diffusion length, L_D.[54] This kind of diffusion length can be defined by the relationship between diffusivity D and carrier lifetime τ, or $L_D = \sqrt{D\tau}$, with diffusivity directly related to carrier mobility by $\mu = qD/k_BT$ (q is charge and T is temperature). This relationship implies that in order to have a large L_D, the material in question must have either a large μ or a long τ, or both.

In wide-bandgap semiconductors with low dielectric constants, excitons heavily dressed by phonons can be immobilized by a self-trapping mechanism, such as in the case of metal halides and OMHHs.[22] [21] [55] On the other hand, in inorganic semiconductors with larger dielectric constants, electric field screening can result in highly mobile excitons, exhibiting mobilities as high as 2×10^6 cm^2/Vs in Si[56]. It is important to note here that although excitons are charge neutral, their mobility can still be derived from D, analogous to charged particles. How excitons interact with free carriers, phonons, and the ever-present electric and magnetic fields within semiconductor materials is essential to understanding their exotic behaviors and transport properties.

1.2.2 Excitons in Relevant Semiconductors

Excitons in HOIPs: In regards to exciton transport, HOIPs are of particular interest to this dissertation. While the E_B values are intrinsically lower in many of the vanguard HOIPs being studied than those of purely organic semiconductors, excitons may still form in significant populations when the proper conditions are met. The ratio of coexisting excitons and free carriers can be quantitatively estimated by the Saha-Langmuir equation (**Equation 1.1**), which effectively relates relative exciton population to temperature and (excitation) density.[57] The fraction, x, of free charge carriers over the total excitation density for a 3D semiconductor can be written as

$$\frac{x^2}{(1-x)} = \frac{1}{n}\left(\frac{2\pi\mu k_B T}{h^2}\right)^{3/2} e^{-\frac{E_B}{k_B T}} \tag{1.1}$$

where μ is the reduced exciton mass, h is Planck's constant, T is temperature, and n is the total excitation density (excitons and free carriers combined).

At sufficiently low temperatures ($k_BT \ll E_B$), a majority of photoexcited charge carriers are bound into excitons. Similarly, under intense enough excitation densities, significant exciton formation is promoted due to the forced close proximity of the charged species. In our studies of $MAPbI_3$ and $MAPbBr_3$, the competition and control of E_B and k_BT will be the more interesting factor (high laser intensities are required in order to generate large carrier densities, and high laser intensities destroy these samples quite quickly).

E_B has been measured in $MAPbI_3$, by magnetic field-dependent optical interband absorption,[58] to be 16 meV in the low temperature orthorhombic phase and drops sharply to only a few meV in the tetragonal phase (around 160 K). Such an abrupt shift in E_B is expected due to the sudden change in dielectric function across the phase transition.[59] This low E_B suggests that excitons are unlikely to form in $MAPbI_3$ at room temperature, where k_BT is about 26 meV. Hence, our measurements proved to be most intriguing at lower temperatures,[60] where $MAPbI_3$ has transitioned into the orthorhombic phase. $MAPbBr_3$, however, has a much larger E_B than even $MAPbI_3$'s low temperature binding energy. A wide range of E_B values has been reported, up to 150 meV (a value comparable to those of organic semiconductors), indicating excitons and free carriers can coexist at room temperature.[61] Similar to $MAPbI_3$, the E_B of $MAPbBr_3$ also increases further at the low temperature phase change (tetragonal to orthorhombic). In fact, E_B becomes so strong at low temperature, it can be directly observed via photocurrent spectroscopy in our own samples.[62] In both of these HOIPs, fascinating and unique transport behavior emerged as E_B overcame k_BT, giving rise to our super-mobile exciton transport model, as will be discussed in detail in Chapter 3.

Excitons in Low-Dimensional Materials: Low-dimensional HOIPs, with quantum confinement effects and intrinsically huge E_B values, offer an excellent platform to study exci-

tons. Ruddlesden–Popper halide perovskites (RPPs) with the scary-looking chemical formula $(BA)_2MA_{n-1}Pb_nX_{3n-1}$ (where X is I, Br, or Cl), composed of 2D layered perovskite structures separated by long, chain-like spacer molecules, can be mechanically exfoliated relatively easily.[63] [64] Such single flake RPP devices remove complications of inhomogeneity and domain boundaries associated with poly-crystalline films and allow better understanding of the intrinsic properties. Pure phase RPPs have been synthesized with controlled layer numbers (n).[65] The long chain spacer molecules suppress nonradiative recombination[66] and improve the long term stability.[67] Due to this strong confinement, E_B has been demonstrated to increase with decreasing n and can reach up to 470 meV at n=1.[68] A carrier mobility of 10 cm^2/Vs and L_D of up to 2.5 μm have been measured by THz spectroscopy in 2D MA-phenylethylammonium (PEA) lead iodide at room temperature.[64]. An enormous Rashba splitting has also been observed in 2D perovskites as well as quantum-confined perovskite nanocrystals,[69] [70] which is highly sought after for spintronic applications.

Furthermore, 1D and 0D HOIPs[71] [72] and 1D OMHHs[21] [29] [55] have also recently been synthesized with even stronger quantum confinement and near-unity PL quantum efficiency. 1D and 0D HOIPs/OMHHs are obtained by effectively slicing 2D HOIPs/OMHHs into metal halide wires and individual octahedra, respectively.[72] 1D structures, with coincident electronic band formation and structural distortion, display large Stokes-shifted broadband emissions due to both free excitons (FE) and STEs.[72] [73] [74] In comparison, 0D structures, composed of isolated (due to the surrounding inorganic or organic cations) metal halide octahedral anions or metal halide clusters, do not retain their electronic band formation. Therefore, the 0D structures act like individual metal halide octahedra or metal halide clusters and display strongly Stokes-shifted broadband emissions with high PL quantum efficiency from STEs only.[72] [75]

Of particular interest to this dissertation are the optoelectronic properties of 1D OMHHs, which largely depend on the formation of STEs, resulting from strong electron–phonon coupling. STEs can be found in organic molecular crystals,[76] condensed rare gases,[77]

and halide crystals.[78] In these kinds of materials, electron-phonon interactions are so strong that the excited charge carriers can elastically warp the surrounding lattice.[79] This warping is unfavorable in terms of energy, compared to the self-trapping mechanism. Thus, an STE can be thought of as the bound state of an electron and a hole (an exciton), which is self-trapped in a lattice distortion field, forming a small polaron due to the strong coupling between the exciton and the lattice.[29] [71] [80] [81] [82] In the self-trapping process, electrons are first photo-excited to FE states. Then the resulting FEs undergo a very fast relaxation ($<$ 1 ps) to self-trapped states, which may contain several trapped centers with dissimilar energies.[29] The subsequent decay from these self-trapped states, with numerous local energy minima, leads to broadband emission. Generally, it is accepted that low structural dimensionality is required, or at least expected, for STE formation. However, density-functional theory (DFT) calculations suggest that the formation of STEs, and the resulting broad emission, require an appropriate electronic dimensionality rather than just structural dimensionality.[29] [83].

1.3 Outline of this Dissertation

In the following chapters we will dive into the world of exciton-driven phenomena in 3D HOIPs and 1D OMHHs, from the perspective of several research projects. Chapter 2 contains descriptions of the various experimental techniques utilized in these projects, including synthesis methods, device fabrication, and multiple characterization techniques. Chapter 3 discusses the published observations of highly mobile excitons at low temperature in the vanguard HOIPs $MAPbI_3$[60] and $MAPbBr_3$,[62] and the interesting differences between the two materials. Chapter 4 moves on to a similar class of materials, organic metal halide hybrids, and examines the recently published[55] anisotropic emission properties of self-trapped excitons in 1D $C_4N_2H_{14}PbBr_4$ single crystals. Finally, Chapter 5 consists of a summary of the projects' results and some discussion of ongoing and future related research endeavors.

Chapter 2. Experimental Techniques

The majority of the work that went into these various projects took place in two locations: the somewhat vibrationally-isolated basement of the UC Davis Physics and Astronomy building, and the Center for Integrated Nanotechnology Core (Sandia National Laboratory) and Gateway (Los Alamos National Laboratory) Facilities. The HOIP sample synthesis, HOIP device creation, scanning photocurrent measurements, and XRD characterization took place at UC Davis, while the static and time-resolved photoluminescence measurements occurred at the CINT locations. Sample growth for the 1D OMHHs was performed externally by our collaborators at Florida State University.

2.1 Synthesis and Characterization of $MAPbI_3$ and $MAPbBr_3$

HOIPs come in a large variety of structures, ranging from cm-sized bulk crystals to polycrystalline thin films to quantum dot and nanocrystal colloidal solutions. In our case, we focused on a solution-based synthesis method that produces high-quality single crystal microstructures (**Figure 2.1**). By working with single crystals, we avoid the detrimental influence of grain boundaries, commonly observed in polycrystalline films, and gain better insight into the more intrinsic transport properties of the material itself. Furthermore, by keeping the samples small (10's of nm to single μm in thickness), we are granted access to field-effect transistor (FET) architectures where we can directly tune the carrier concentration through back-gating.

$MAPbI_3$ and $MAPbBr_3$ micro-structures (predominantly micro-beams and microplates) were grown in very similar ways, but the details for each are as follows:

$MAPbI_3$ - Initially based off the instructions of our synthesis collaborators,[84] 40 mg of MAI powder (Sigma Aldrich >98%) are slowly dissolved in 1 mL of isopropyl alcohol (IPA 99.5%) in a glass vial inside a nitrogen glovebox. Meanwhile, 100 mg of $PbAc_2\ 3\,H_2O$ (Sigma Aldrich 99.999%) powder are dissolved in 1 mL of deionized water. The $PbAc_2$ solution is

distributed across an FTO-coated glass slide by spin-coating at 600 RPM for 40 seconds. The coated substrate is then baked at 60 °C until dry and then placed upside down inside the vial of MAI solution at 50 °C in an oven for several days. After baking, the substrate is removed from the vial, gently dipped into IPA for a few seconds, and then blown dry with nitrogen.

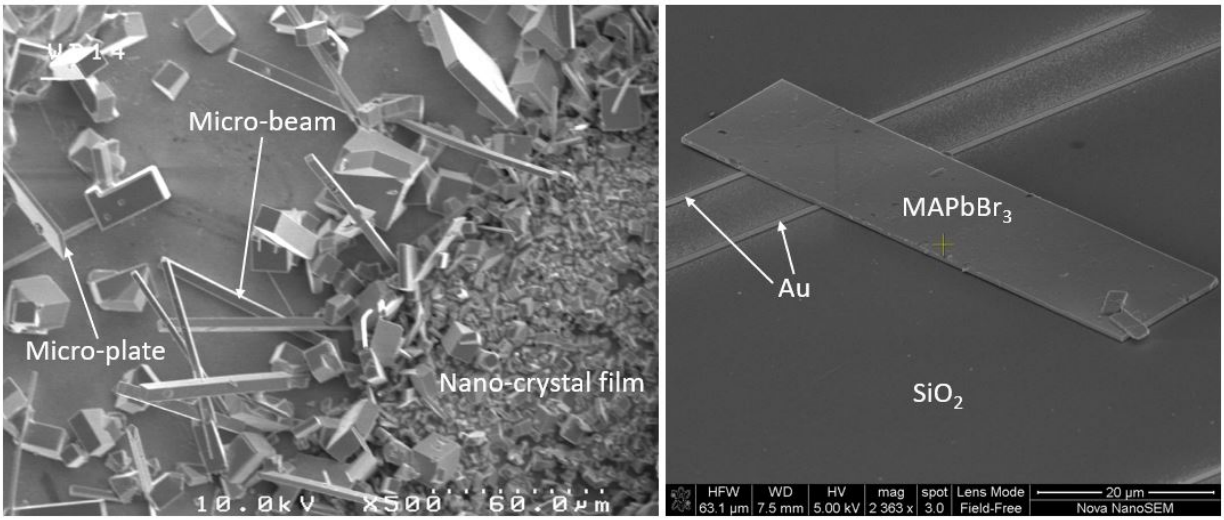

Figure 2.1: SEM images of micro-structure HOIP samples. (Left) As-grown $MAPbI_3$ single crystals on the growth substrate. Examples of micro-beams and micro-plates can be seen, as well as some nano-crystal film (right side of image). (Right) Single crystal $MAPbBr_3$ micro-plate lying across two gold electrodes in our typical FET device configuration. This particular crystal is about 640 nm thick and 74 μm long.

There are 2 main differences between our synthesis method and the previously mentioned published work[84] - (1) is the duration of oven baking and (2) is the use of $PbAc_2$ (Ac = acetate, or CH_3COO^-) instead of PbI_2. As shown in that work, baking for 20 hours resulted in single crystals of a few μm in length. By allowing the baking process to continue for $>$ 24 hours, even up to a few days, we are able to obtain single crystals of up to 200 μm in length and 10's of μm wide. Importantly, we did not attempt to grow the crystals much larger than this, due to the desire to keep sample thickness limited to within a few μm, for effective FET device construction. The choice to switch from PbI_2 to $PbAc_2$ was based upon subsequent literature,[85] [86] showing that the use of $PbAc_2$ leads to higher quality crystals.

The chemical mechanism behind the $MAPbI_3$ micro-crystal synthesis relies on what is known as a dissolution-recrystallization process.[84] When the dry, spin-coated $PbAc_2$ comes into contact with the MAI solution, a low-quality, thin film of $MAPbI_3$ immediately forms at the substrate surface, which actually blocks deeper $MAPbI_3$ crystallization. The crystallization of $MAPbI_3$ can be represented by the following equation:

$$PbAc_2 + 3CH_3NH_3I \rightarrow CH_3NH_3PbI_3 + 2CH_3NH_3Ac \tag{2.1}$$

or equivalently

$$PbAc_2 + 3MAI \rightarrow MAPbI_3 + 2MAAc \tag{2.2}$$

The initially messy $MAPbI_3$ layer and the surrounding solution interact in a continuous cycle of the $MAPbI_3$ dissolving and recrystallizing, and with each cycle the $MAPbI_3$ becomes higher quality and single crystals begin to nucleate and grow. This is due to the thermal instability of the by-product MAAc, which has been shown to sublimate and/or evaporate out of the solution as time passes,[87] leading to more and more pure $MAPbI_3$ and less messy mixture.

$MAPbBr_3$ - We follow a similar synthesis method for $MAPbBr_3$. 6 mg of MABr powder (Sigma Aldrich >98%) are slowly dissolved in 1 mL of isopropyl alcohol (IPA 99.5%) in a glass vial inside a nitrogen glovebox. Meanwhile, 100 mg of $PbAc_2\ 3\,H_2O$ (Sigma Aldrich 99.999%) powder are dissolved in 1 mL of deionized water. The $PbAc_2$ solution is distributed across an FTO-coated glass slide via manual spreading with a pipette, rather than spin-coating, while baking on a hot plate at 90 °C until dry. The slide is then placed upside down inside the vial of MABr solution at 40 °C for 1 - 3 days. Afterwards, the substrate is removed, gently dipped into IPA for a few seconds, and then blown dry with nitrogen.

The chemical process behind this synthesis is effectively identical to that of $MAPbI_3$, just replacing the halide ion I^- with Br^-. The use of manual spreading of solution instead of spin-coating arises entirely from an unfortunate change in FTO substrate manufacturer. The original FTO slides used for $MAPbI_3$ eventually ran out and we were unable to find an exact replacement. The new slides proved to be terrible at retaining droplets of solution during the spin-coating process, and so we switched to distributing the solution across the slide by hand. I find this to be a great example of how unexpectedly small alterations in technique can lead to huge changes in the end result.

2.2 Perovskite Micro-Structure Device Fabrication

HOIPs are sensitive to both high heat as well as several solvents used in lithography. Thus, it is difficult to fabricate micro-beam and/or micro-plate devices using conventional e-beam or photo-lithography methods. Instead, a more creative, and directly hands-on, technique was applied to fabricate our FET devices. The as-grown micro-structures were mechanically transferred via micro-fiber (cat hair, provided by Dr. Dong Yu's cats), by uncaffeinated hands, from the glass slide substrate to the device substrate. The device substrates were fabricated at the UC Davis Center of Nano and Micro-Manufacturing (CNM2) cleanroom facility and consist of a conductive silicon chip, followed by a 300 nm thick insulating layer of SiO_2, with pre-patterned 40 nm thick electrodes (5 nm Cr, 35 nm Au) on top (**Figure 2.1-Right**). With practice, one can select which pair of electrodes the sample crystal will land on, and even control the orientation and tilt of the crystal, with respect to the electrode direction. The ideal placement for our studies was to have most of the micro-beam or micro-plate away from the electrode channel (a pair of electrodes), while still making contact with both electrodes. The reasoning behind this will become clear in Chapter 3.

Once several micro-structure FET devices were prepared (all on one device substrate, as shown in **Figure 2.2-Left**), the substrate was installed in an optical cryostat (Janis ST-500) capable of reaching an internal pressure of 10^{-6} torr, thus minimizing detrimental

humidity effects on the HOIP samples and allowing for low temperature (down to 8 K) measurements. Characterization current-voltage curves were measured through a current preamplifier (DL Instruments, model 1211) and an NI data acquisition system. If the FET devices proved to be conductive, light-sensitive, and stable, SPCM measurements could begin.

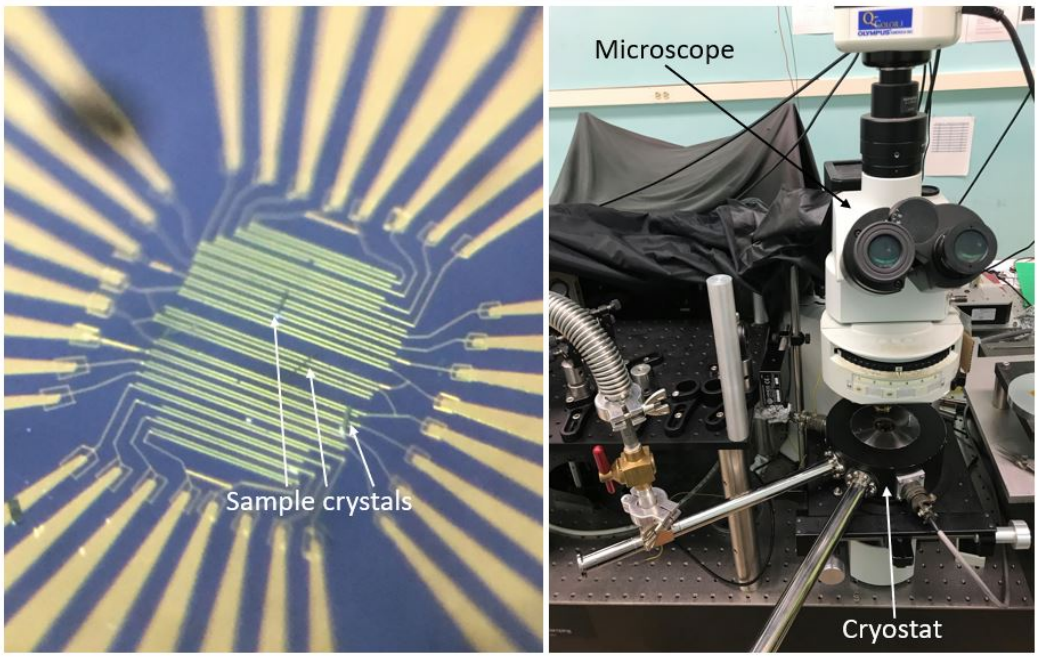

Figure 2.2: Experimental equipment. (Left) FET device chip with multiple sample crystals lying across pairs of gold electrodes. The thin electrode pairs (each electrode is 1 μm wide and 40 nm thick; 10 μm gap between pairs), feed off to large gold pads ($>$ 100 μm wide at the ends) for wire-bonding to make electrical connections. (Right) Home-built SPCM setup. The excitation laser is passed through the microscope, out the objective lens, and into the optical cryostat, where the device chip (Left) is mounted.

2.3 Scanning Photocurrent Microscopy

Scanning photocurrent microscopy, or SPCM, utilizes a focused light beam as a local excitation source, similar in concept to the probe tip of an atomic force microscope or scanning tunneling microscope.[88] [89] [90] [91] [92] J. Marek is credited with one of the first quantitative studies that put SPCM to real use, where the technique was applied to measure

photocurrent profiles at grain boundaries of semi-crystalline solar cell materials.[93] Over the last decade, the technique has been put to particularly effective use in the analysis of semiconductor micro and nano-structures.[94] [95] [96] [97] [98] [99] [100] [101] [102] [103] [104] In a typical SPCM system, a focused laser beam of selected energy is used to locally excite a semiconductor material out of equilibrium. The injected carriers, typically electrons and holes, then undergo a relaxation process that can consist of many pathways: thermal relaxation, recombination, drift, diffusion, etc. If the injected charge carriers make it to an electrode (or any charge collection zone of the semiconductor device architecture) before they recombine, a photocurrent is measured. Combined with some form of scanning mirrors or sample stage with programmable motion control features, a spatial mapping of photocurrent as a function of excitation location can be created. Such a mapping provides direct information on the optoelectronic properties of semiconductors, such as internal electric field, charge transport behaviors, and recombination dynamics.[90] The experimental results generated by this powerful measurement technique have been rigorously compared to derived theoretical calculations, considering absorption cross sections, excitation wavelength, and excitation spot size, and display excellent mutual agreement.

Here, SPCM measurements were performed using a home-built setup (**Figure 2.2-Right**) that consisted of a laser source, its associated optical components, a pair of mirrors mounted on galvanometers (also known as scan-mirrors), an optical microscope, and a current preamplifier. A 532 nm CW laser or a tunable pulsed laser (NKT SuperK plus 500 - 1700 nm) was focused by a 40x N.A. 0.6 objective lens to a diffraction limited spot with a diameter of about 1 μm and raster-scanned on various HOIP FET devices by the pair of scan-mirrors, while both reflectance and photocurrent were simultaneously recorded to produce two-dimensional maps of photocurrent sign and amplitude as a function of XY position. The position value is converted from the voltage output to the scan-mirror. The angle of the mirror (and hence the position of the laser) is proportional to this voltage, where the conversion factor has been calibrated. The laser power, ranging from 10s of nW to several

μW, was controlled by a set of neutral density (ND) filters and was measured by a power meter underneath the objective lens of the microscope.

When the HOIP micro-structures make contact with the gold electrodes, a Schottky junction is formed. This is a typical semiconductor phenomenon that occurs when the Fermi level of the sample material does not match the Fermi level of the metal electrode. When the two are placed in contact, the Fermi level of the sample is forced to locally align with the Fermi level (**Figure 2.3A**) of the metal, which leads to band-bending at the location of contact (the sample's conduction and valence bands are tilted in energy toward the fixed Fermi level). This bend in electrical potential energy results in a local, built-in electric field at the junction, with the field direction dependent on the relative tilt slope (tilting up or down toward the contact). When an excitation source, such as a laser, generates charge carriers in the sample, those carriers can drift and/or diffuse through the material. If they survive long enough before recombining, they may interact with the electric field surrounding the Schottky junction and thus be detected/collected as photocurrent. Depending on the previously mentioned tilt slope, or band-bending direction, the polarity of the detected photocurrent will be either positive or negative. The band-bending, and therefore local electric field, can also be influenced via the application of an external bias voltage V_{SD} (SD stands for source-drain), where the sign and magnitude of V_{SD} can enhance or dampen the tilting at the contact (**Figure 2.3A**). An applied gate voltage (V_G) may also affect the band-bending by globally shifting the sample Fermi level up or down. Furthermore, the Schottky junctions created at material interfaces are not the only sources of in-built electric fields that SPCM can detect. Band-bending can also be generated at any region where there is an inhomogeneous collection of charge, either manually created through doping or intrinsic to the sample, and SPCM can be used to study such regions.

Of particular relevance to the studies presented in this dissertation, SPCM can also be used to directly measure a sample's (minority) carrier diffusion length L_D. Upon excitation from the laser, photo-generated carriers outside of the electrode channel (where there

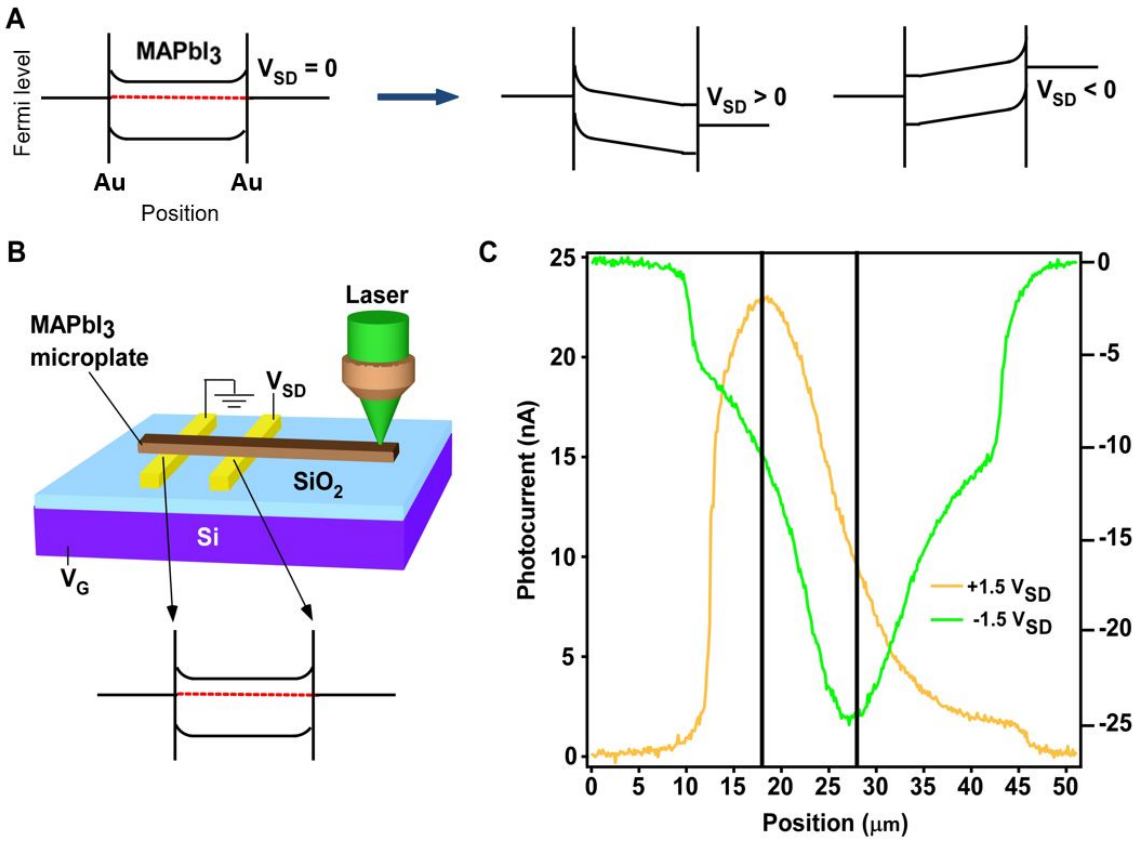

Figure 2.3: (A) Band-bending diagrams at different V_{SD} for an n-type $MAPbI_3$ device. (B) Schematic for SPCM. (C) Experimentally obtained SPCM profiles along the sample axis at room temperature, showing peak shift at opposite V_{SD}. The photocurrent is always peaked at the reversely biased contact and flips sign, consistent with the band-bending diagrams.

is no electric field-induced drift component) will diffuse through the sample until either recombining or making it to the Schottky junction and being collected as photocurrent. Due to the ever-present recombination factor, the odds of these excited carriers making it to the junction and being collected decrease exponentially as the distance between laser spot and junction increases. This implies that the measured photocurrent, too, should drop off exponentially as the laser scans across the sample, away from the contact, and this is indeed what is observed (**Figure 2.3C**).

In the linear regime, where the laser-excited carrier concentration is much smaller than the majority carrier concentration in the dark, carrier recombination (R) is proportional to the laser intensity:

$$R = B_r np = B_r(n_0 + \Delta n)(p_0 + \Delta p) \approx B_r n_0 \Delta p \tag{2.3}$$

for n-type, or $B_r p_0 \Delta n$ for p-type.

Here, B_r is the recombination rate, which is a constant; n_0 and p_0 are the dark electron and hole concentrations, respectively; Δn and Δp are the laser injected electron and hole concentrations, respectively. Recombination lifetime τ is therefore a constant, represented as $\tau = 1/(B_r n_0)$, so $R = \Delta p/\tau$ (for an n-type material), and the measured photocurrent decays exponentially. The decay length of the photocurrent corresponds directly to the carrier diffusion length.

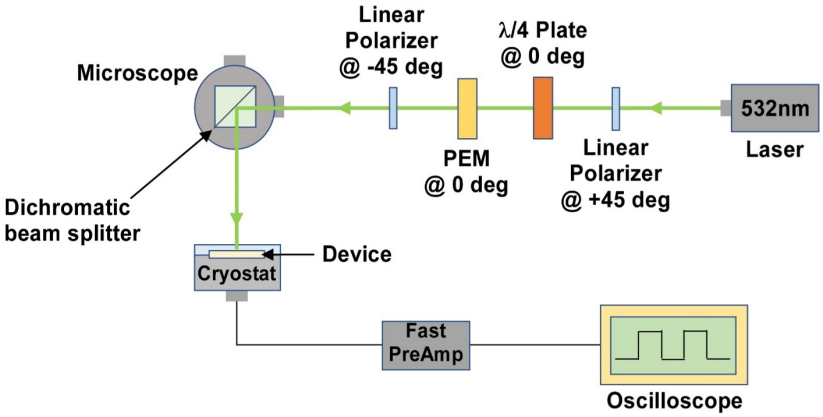

Figure 2.4: Schematic of transient photocurrent measurement setup.

2.4 Transient Photocurrent Measurements

Before gaining access to the time-resolved systems at the CINT facilities, we attempted to get an idea of the temperature-dependent carrier dynamics of our HOIP samples through a homemade optical chopping setup. We used a combination of a photoelastic mod-

ulator (PEM), quarter waveplate, and two crossed linear polarizers to modulate the light intensity at 50 kHz with an intensity decay (resolution) of about 0.5 μs (**Figure 2.4**). A high-speed amplifier (Femto DHPCA-100) and a digital oscilloscope were used to measure the transient photocurrent response.

2.5 Photocurrent Spectroscopy

Photocurrent spectra were measured through a current preamplifier (DL Instruments, model 1211) and a NI data acquisition system. A fixed or sweeping bias voltage V_{SD} was applied to the sample while a tunable laser was focused onto the sample surface. The generated photocurrent was measured while a macro-program scanned the tunable laser through a wide range of output wavelengths. After accounting for laser power calibration effects, any increase or decrease in the measured photocurrent corresponded to an increase or decrease in the sample's absorption coefficient. This method allowed us to directly measure the E_B of our $MAPbBr_3$ samples, where a strong exciton peak can be seen shifted away from the bulk absorption edge. The fittings required to estimate E_B, called Elliott fittings, and the associated error, are discussed in detail in Chapter 3.

2.6 Synthesis and Characterization of $C_4N_2H_{14}PbBr_4$

Macroscopic $C_4N_2H_{14}PbBr_4$ single crystals were synthesized by Biwu Ma's team at FSU, according to the following procedure. Lead(II) bromide ($PbBr_2$, 99.999%), N,N'-dimethylethylenediamine (DMEDA, 98%), hydrobromic acid (HBr, 48 wt.% in H_2O) were purchased from Sigma-Aldrich. Acetone ($\geq$ 99.5% ACS) was purchased from VWR Chemicals BDH. All reagents and solvents were used without further purification unless otherwise stated. Equimolar amounts of lead(II) bromide and N,N'-dimethylethylenediamine (0.27 mmol) were added into 10 mL of 48 wt.% hydrobromic acid, then the mixture was sonicated to yield a clear solution. Needle-like single crystals of $C_4N_2H_{14}PbBr_4$ were obtained through diffusion of acetone into 1 mL of the precursor solution for 24 hours. The crys-

tals were washed with acetone and then dried under reduced pressure for further use and characterization.

The structural orientation of the single crystals was investigated with X-ray diffraction (Rigaku MiniFlex600 Diffractometer).[105] A $C_4N_2H_{14}PbBr_4$ single crystal was placed on the substrate with one facet facing upward for the X-ray 2θ-scan. The facet of the single crystal was identified with the group of diffraction peaks. An ensemble of crystals was also checked by placing multiple crystals on the puck with one of their side facets parallel to the substrate. The result shows that only the {101} and {200} peaks were observed, indicating that the side facets of the crystals belong to either the {101} or the {200} plane families. These data were collected by Valentin Taufour's team at UC Davis and are displayed in Chapter 4.

2.7 Static and Time-Resolved Photoluminescence Spectroscopy

$MAPbBr_3$ Measurements: A picosecond pulsed laser (Picoquant LDH-D-C-405) with a wavelength of 405 nm and pulse width of 56 ps was used for excitation. The laser was reflected through a dichroic beamsplitter (Semrock Di02-R405) and then focused onto the sample to a diffraction limited spot size using a 50x, 0.7 NA Olympus objective microscope (LCPLFLN50xLCD), which was used to both excite the sample and collect the PL. Collected photons after passing through the same dichroic beamsplitter and a 496 nm long-pass filter either go to a spectrometer+CCD (Acton SP2300i, pylon100) or a single photon avalanche photodiode (Excelitas SPCM-AQRH-14). TRPL was analyzed using a TCSPC module (Picoquant Hydraharp 400). For spectra, a focusing lens was used before the objective to uniformly illuminate smaller samples with a spot size of about 30 μm. Then the spectrometer slit was closed to the smallest width of 10 μm to analyze the spectra in the region of interest. The average laser intensity varies from 0.3 W/cm^2 at low temperature to 14 W/cm^2 at room temperature, where the emission is much weaker (intensity dependence is displayed in **Appendix Figure B.9**).

$C_4N_2H_{14}PbBr_4$ Measurements: An ultrafast Ti:Sapphire pulsed laser (Coherent Chameleon Ultra) with a tunable wavelength range of 680 - 1080 nm and pulse width of 140 fs was used for excitation. For the high energy excitation, the Chameleon output was sent through a frequency doubling module. Collected photons are sent to a spectrometer (Acton, Princeton Instruments) and a Hamamatsu streak camera. The average laser intensity typically varies from about 10 to 50 W/cm^2 across the low temperature and room temperature measurements. Excitation polarization is controlled via a combination of a UV linear polarizer, UV half-wave plate, and nonpolarizing cube beam splitter. Emission polarization is measured via another linear polarizer in line with the detection path. The low temperature PL measurements were carried out in a close-cycle cryostat (Montana Instruments). A schematic of this system is displayed in Chapter 4.

Chapter 3. Speedy Excitons in $MAPbI_3$ and $MAPbBr_3$

3.1 Excitons, Phonons, and HOIPs, Oh My!

Exciton mobility in HOIPs is a complicated and lesser known subject of study, as most work to date has been focused on free charge carrier transport in these materials. When a typical charge carrier, such as an electron or hole, interacts with the LO phonons of the surrounding crystal lattice, it can be thought of as a quasi-particle called a polaron.[16] The HOIPs relevant to this work, namely $MAPbI_3$ and $MAPbBr_3$, have a Young's modulus that is roughly 10 times lower than common inorganic semiconductors like silicon[13] (I promise this is relevant). The Young's modulus here is directly related to the connectivity of the B-X bonds (from the ABX_3 structure) and their interaction with the central A-site cations. This relatively soft nature allows these HOIPs to manifest a crystalline solid and liquid-like behavior.[106] The halide ions, in particular, are able to move perpendicularly to the Pb-Pb axis with a strong anharmonic motion,[107] [108] [109] and the organic cations can tumble within the BX_3^- cage because of their charge anisotropy,[110] thus largely affecting the local polarization and charge-carrier transport.[4] [111] This polarizability allows for the formation of what is called a large polaron, with a diameter much larger than the lattice unit cell.[14] Large polarons are one of the most popular ideas for explaining the unique optoelectronic properties of HOIPs, including electric field screening, defect tolerance, slow hot carrier cooling, and high carrier mobility.[15] An exciton can also interact with the surrounding lattice, forming an exciton-polaron (making the math get even trickier), and this interaction can have a significant effect on the exciton's binding energy and transport properties.[112]

The majority of studies on exciton transport in HOIPs have been focused on either nano-crystals or layered, 2D samples, since E_B in these systems can easily be larger than k_BT, even at room temperature. Exciton L_D values ranging from hundreds of nm to over 1 μm have been measured in $CsPbBr_3$ nano-crystals (200 nm),[113] 2D $(BA)_2(MA)_{n-1}Pb_nI_{3n+1}$ single crystal flakes (several hundred nm),[114] and $MAPbBr_3$ nano-crystal films (> 1 μm).[115] Extended exciton diffusion in HOIP nano-crystal films has also been attributed to photon

recycling, but efficient exciton hopping is still believed to be the main contributor.[115] [116] In contrast to these systems, the ability for excitons to diffuse efficiently in 3D HOIPs is still an unclear subject. Gaining a deeper understanding of the effects of excitons on the intrinsic transport properties of 3D HOIPs is crucial to the progression of improving the optoelectronic performance of these materials.

3.2 Measuring Diffusion Length in HOIPs, A Brief Review

Much of the literature on optoelectronic studies of HOIPs involves measurements performed with global (large area) illumination, where the entire sample is covered with uniform light intensity. In constrast, spatially resolved illumination measurements can reveal information that global illumination cannot detect. In particular, the spatial sensitivity of SPCM makes it capable of extracting key material properties such as electric field distribution, local band-bending, and carrier diffusion length.[90]

Quite a variety of L_D values have been reported, ranging from 100 nm to 175 μm, across multiple kinds of HOIP systems (thin films, nano and micro-crystals, bulk single crystals, etc).[9] [11] [12] In many of these studies, L_D is determined indirectly. By separately measuring the carrier lifetime τ and mobility μ, one can calculate L_D through $L_D = \sqrt{D\tau}$, with diffusivity directly related to carrier mobility by $\mu = qD/k_BT$.[11] [12] Spatially resolved techniques have demonstrated more direct ways of obtaining L_D, such as spatially resolved PL,[117] where the Gaussian spatial spread of emitted light is carefully observed, and spatially resolved photocurrent measurements,[118] [119] [120] [121] which will be discussed in detail in this chapter. The broad variety of HOIP L_D values in literature likely arises from the vastly different methods of sample preparation, as well as the different measurement techniques. In fact, at least one paper has been written just to argue for the use of standardized material property tests on HOIPs because of the variety of results being published.[122]

As previously mentioned, most of the current literature quoting an L_D value utilized an indirect method to obtain it. A typical method involves getting lifetime via time-resolved

PL decay and mobility from current-voltage curves, and then doing a bit of math to get L_D. SPCM, however, provides a direct path to determining the minority carrier L_D. Careful modeling of SPCM has proven that the measured exponential decay of photocurrent is directly proportional to the characteristic minority carrier diffusion length, and can thus be fit with a simple exponential decay to extract L_D.[88] [123] SPCM and electron beam induced current (EBIC), a similar measurement technique in working principle, are both well-accepted methods of directly obtaining the L_D of semiconductor materials, including Si, GaAs, ZnO, and PbS.[88] [90] [97] [123] [124] [125] [126] [127]

Lastly, the majority of HOIP L_D studies have been performed at room temperature, which is certainly a relevant temperature to use when considering these materials for use in solar panels some day. That being said, exploration of the optoelectronic properties at low temperature reduces complications resulting from thermal fluctuations and may lead to deeper insights that cannot be garnered at room temperature. Indeed, many 3D HOIPs undergo one or more first-order phase transitions (usually cubic to tetragonal to orthorhombic; see **Figure 1.1**) as temperature is decreased; the resulting crystal structures become less and less symmetric and these transitions can have strong impacts on the material's optoelectronic properties. For example, $MAPbI_3$ is known to shift from cubic (α) to tetragonal (β) phase around 327 K, and then from tetragonal to orthorhombic (γ) around 163 K.[119] [128] The low temperature phase shift in particular is associated with a dramatic change in the PL emission behavior.[129] [130] [131] [132] [133] Transport properties, like mobility and, importantly, L_D, are also expected to change with temperature. Mobility is known to follow a power law dependence on temperature ($\mu \sim T^{-k}$)[134] and the exponent k here is found to be close to 1.5 in $MAPbI_3$[135] [136] and cubic $MAPbBr_3$,[137] which is consistent with acoustic phonon scattering.[14] [16] [134] [138] [139] Rashba and Dresselhaus effects, induced by spin-orbit coupling, are also anticipated to have strong temperature dependence, due to low temperature ferroelectric behavior[140] and symmetry breaking during the structural phase transitions.[141] Investigating these temperature-induced changes can provide crucial insights to how phonon

scattering, ion migration/rotation, structural distortion, and other thermally activated phenomena, affect the charge carrier and exciton transport in these HOIP systems.[60] [62]

3.3 Temperature and Gate Control of Carrier Diffusion in Single Crystal $MAPbI_3$ Micro-Structures

Now, at last, it's time to dive into my personal investigations of the temperature-dependent optoelectronic properties of 3D HOIP systems, beginning with arguably the most popular HOIP in literature, $MAPbI_3$. Here, we examine the roles that temperature and structural phase play on carrier transport and recombination within $MAPbI_3$ single crystal micro-structures. We apply scanning photocurrent microscopy to directly extract the carrier diffusion length in $MAPbI_3$ micro-plate field effect transistors (FETs) in the temperature range of 80 - 300 K. Studying single crystal halide perovskites eliminates the complications caused by grain boundaries as in polycrystals. Furthermore, unlike bulk single crystals, single crystal nano and micro-structures[142] allow in-situ gate tuning of Fermi level in the material,[143] facilitating exploration of charge transport mechanisms. Single crystalline micro-structures of $MAPbI_3$ are synthesized following a dissolution and recrystallization process,[84] as described in Chapter 2. Micro-beams and micro-plates with thicknesses of about 1 - 2 μm and lengths up to 100 μm are produced with well defined facets and smooth surfaces (**Figure 3.1A**). These micro-structures are mechanically transferred (thus avoiding detrimental effects of lithography solvents) to pre-patterned Cr/Au electrodes on SiO_2 coated Si substrates to fabricate FETs.

Under global illumination, the current first increases with source-drain bias (V_{SD}) then saturates as V_{SD} increases above 0.3 V (**Figure 3.1B**). The $I - V_{SD}$ characteristics can be understood by a back-to-back diode model,[123] (the anode of one diode is connected in series to the cathode of the other) where current eventually saturates in either biasing direction. The saturation current changes abruptly at 147 K (156 K) during cooling (warming) (**Figure 3.1C**). The photocurrent change shows a single step and occurs in only a few milliseconds

(**Appendix Figure A.1**), implying that the entire sample undergoes a phase transition simultaneously without any mixed phase domains. This critical temperature T_c agrees well with the reported values for the tetragonal to orthorhombic phase transition.[119] [128] The specific T_c values vary from device to device in a range of 15 K among the 10 devices we measured, and were lower in thinner samples, as was noticed in a previous work.[128] Interestingly, we occasionally observed a temporary photocurrent overshoot that occurred at the phase transition (**Figure 3.1C**), which may be related to induced strain as the sample abruptly shrinks by 1% from the tetragonal to orthorhombic phase.[144]

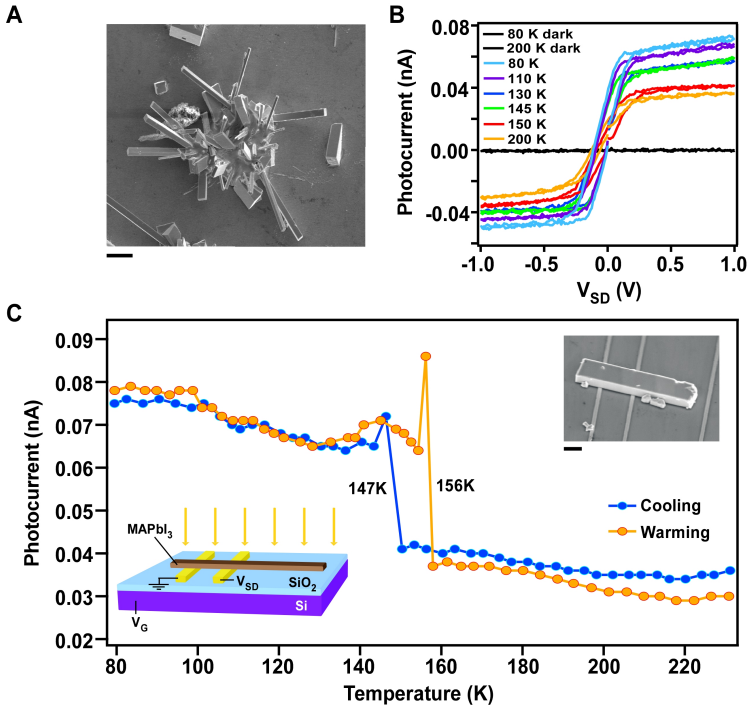

Figure 3.1: Photocurrent response across phase transition under global illumination. (A) Scanning electron microscopic (SEM) image of as-grown $MAPbI_3$ micro-crystals. Scale bar represents 20 μm. (B) $I - V_{SD}$ curves at various temperatures in the dark and under 5×10^{-4} W / cm^2 global illumination. (C) Saturation photocurrent as a function of temperature with $V_{SD} = 1$ V and global illumination. The sample temperature is ramped slowly (3 K / min). Inset: Left, Schematic of a $MAPbI_3$ micro-plate FET under global illumination; Right, SEM image of micro-plate device. Scale bar represents 5 μm.

3.3.1 Temperature-Dependent SPCM - $MAPbI_3$

SPCM is then performed to extract carrier diffusion lengths.[88] [90] [118] [119] [121] [123] The experimental setup is displayed in **Figure 3.2B**, where a micro-plate device is locally excited by a focused 532 nm CW laser with a diameter about 1 μm. While the laser is raster scanned across the entire device surface, the photo-induced current is recorded as a function of laser position and then plotted into 2D photocurrent maps (**Figure 3.2A**). At $V_{SD} = 0$ V, only very weak photocurrent is observed. At $V_{SD} = 3$ V, the enhanced band bending at the reversely biased contact leads to a much stronger photocurrent. The photocurrent peaks near the negatively biased contact, indicating the material is n-type.

While the maximum external quantum efficiency (EQE, defined by the number of collected electrons over the number of incident photons) remains about 35% at all temperatures, the photo-response area sensitively depends on temperature. The laser generates photocurrent both inside and outside the channel, illustrating that the photoexcited carriers can diffuse from outside the channel to the electrodes. Above T_c, the photocurrent is only pronounced in the vicinity of the contacts. Below T_c, the active area in which the laser can create photocurrent increases abruptly, which provides a microscopic understanding of the observed sudden photocurrent change under uniform illumination. At 80 K, the photocurrent remains nearly the same when the laser was scanned over the entire 90 μm long sample (**Figure 3.2A,D**), indicating that the locally generated carriers are equally capable of reaching the contacts and being collected, regardless of initial generation position.

Quantitatively, we extract the photocurrent decay length L_{decay} by fitting the photocurrent distributions along the micro-plate axis with a hyperbolic function, written as $I(x_0) = I_0 \cosh[(x_0 - L)/L_{decay}]$, where x_0 is the distance between the laser position and the contact, and L is the length of micro-plate outside the channel. A cosh function is used instead of an exponential when L_{decay} is not small compared with L [52] - mathematical justification to follow:

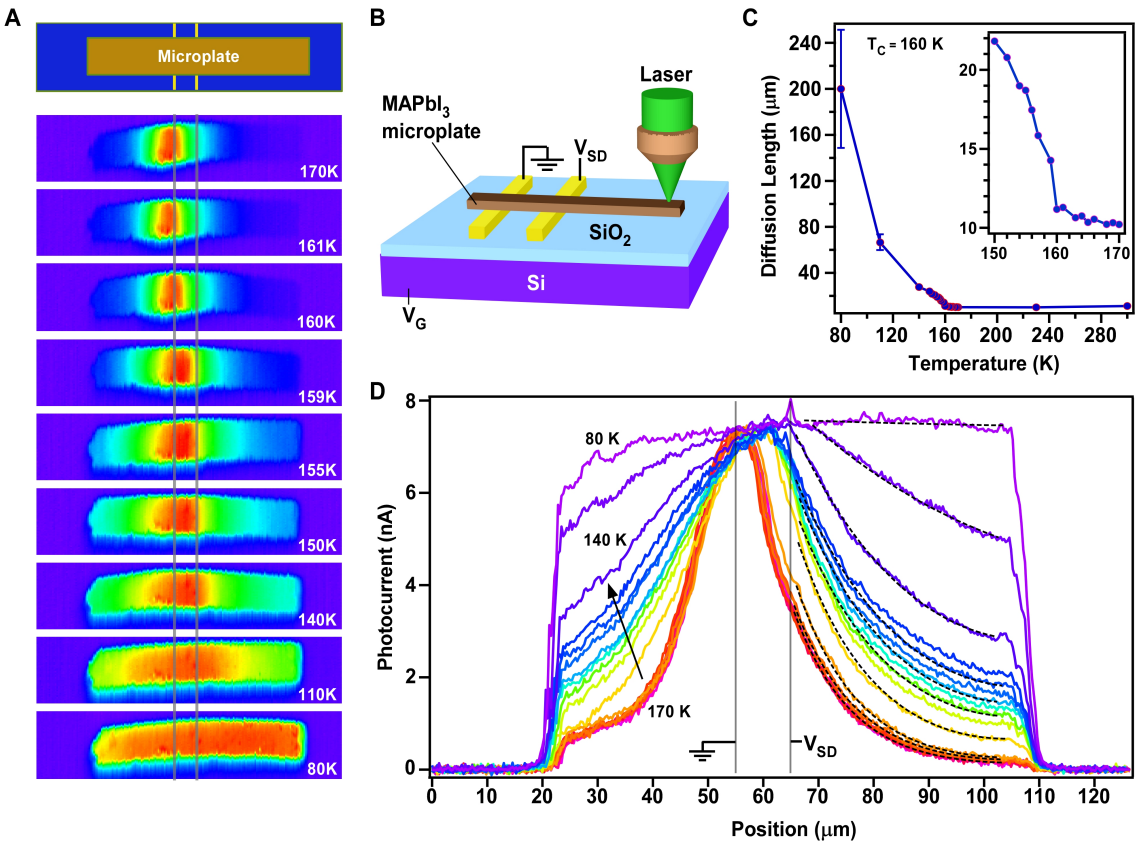

Figure 3.2: Spatially resolved photocurrent. (A) Device layout and photocurrent maps at various temperatures. Grey lines indicate electrode placement. (B) SPCM schematic. (C) Temperature dependent carrier diffusion length extracted by curve fitting photocurrent distributions in (D). Inset shows zoomed-in view of values in the vicinity of T_c (160 K). (D) Photocurrent profiles along the micro-plate axis at various temperatures, taken during warming process with 50 nW laser power and $V_{SD} = 3$ V. Grey vertical lines indicate electrode placement and black dashed curves are curve fittings.

The device geometry is shown in **Figure 3.3**. The steady state continuity equation describing light induced carrier concentration n is,

$$D\frac{\partial^2 n}{\partial x^2} - \frac{n}{\tau} + G\delta(x - x_0) = 0 \tag{3.1}$$

where the local laser generation is considered as a delta function and G is the generation rate proportional to laser power. For boundary conditions, we assume n drops to zero at the contact ($x = 0$) and carriers cannot flow out of the tip ($D\frac{\partial n}{\partial x} = 0$ at $x = L$). n is continuous

at $x = x_0$ and its derivative follows a relation that can be found by integrating **Equation 3.1**. From the solution, we can calculate current distribution as,

$$I(x_0) = eD\frac{\partial n}{\partial x}(x = 0) = eG\frac{cosh(\frac{x_0 - L}{L_{decay}})}{cosh(\frac{L}{L_{decay}})} \tag{3.2}$$

where $L_{decay} = \sqrt{D\tau}$.

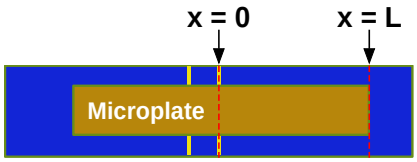

Figure 3.3: Example schematic for extraction of photocurrent decay length.

The main error in L_{decay} originates from error in the photocurrent and laser power. The photocurrent error is about 1%. Because of the large scan areas, the incident laser power is not always perfectly uniform and the photocurrent maps presented have already been calibrated to account for this issue. The uncertainty in power then also affects the corrected photocurrent and is estimated to be 0.5%. From **Equation 3.2**, we find that $L_{decay} = L/cosh^{-1}(z)$, where $z = I(x_0 = 0)/I(x_0 = L)$. We then propagate these error sources to estimate the error in L_{decay},

$$\Delta L_{decay} = \mid \frac{d}{dz}[\frac{1}{cosh^{-1}(z)}] \mid L\Delta z = \frac{1}{[cosh^{-1}(z)]^2\sqrt{z^2 - 1}}L\Delta z \tag{3.3}$$

where $\Delta z/z = \sqrt{2[(\Delta J/J)^2 + (\Delta P/P)^2]} = 1.6\%$.

Both currents are corrected by power, i.e., $I = J/P$ where J is the uncorrected current and P is laser power. The factor of 2 is because z is the ratio of two currents at $x_0 = 0$ and $x_0 = L$. The error becomes large when L_{decay} is long at low temperature since z is close to 1.

We only fit the photocurrent distributions outside the channel, to ensure diffusive transport of carriers[118] and thus obtain L_D from L_{decay}. L_D values are similar on both sides of the channel and the slight difference is presumably caused by the variation in local defect density along the micro-plate. To rigorously confirm the accuracy of this method, we simulated the photocurrent distributions by performing a 2D cross-sectional modeling of perovskite devices under local photoexcitation using COMSOL Multiphysics.[53] [123] The simulated photocurrent distributions follow nicely with the experimental data (**Figure 3.4**). Fits using the cosh function yield L_{decay} in excellent agreement with L_D calculated from the simulation parameters (**Figure 3.4B**).

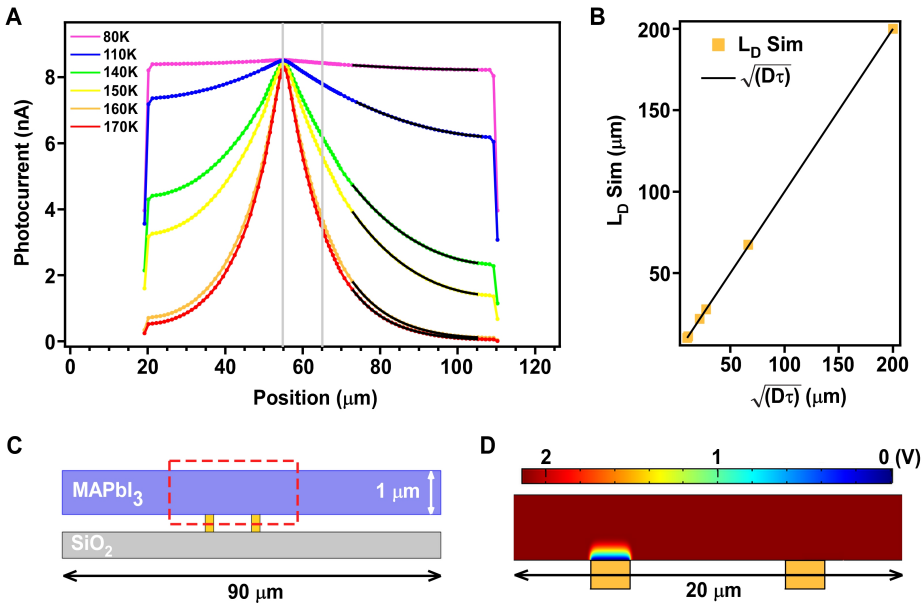

Figure 3.4: Simulated photocurrent distributions. (A) Simulated photocurrent profiles at various temperatures. Grey vertical lines indicate electrode placement. (B) Simulated photocurrent decay lengths L_{decay} are in good agreement with the diffusion lengths calculated from parameters used in the simulation ($L_D = \sqrt{D\tau}$). (C) Device configuration used in simulation. (D) Simulated electric potential distribution in the boxed area in (C) with $V_{SD} = 2$ V at 80 K.

The extracted L_D values remain around 10 μm above T_c, but rapidly increase to 22 μm as temperature decreases, within 10 K below T_c (**Figure 3.2C inset**). At 80 K, L_D reaches 200 $\pm$ 50 μm. The large error bar at 80 K originates from the finite sample length ($L < L_D$), as described above. L_D values at 80 K range from 100 - 200 μm depending on

the sample (data for another sample is shown in **Figure 3.5**). Our result is different from a previous work,[119] where the hole diffusion length was found to be at maximum 150 μm at 160 K but decreased to 50 μm at 96 K. The reason for this discrepancy remains unclear but is most likely related to the sample preparation. Our growth method yields samples with exceptionally low trap density, as demonstrated previously.[106] [142] [145] [146]

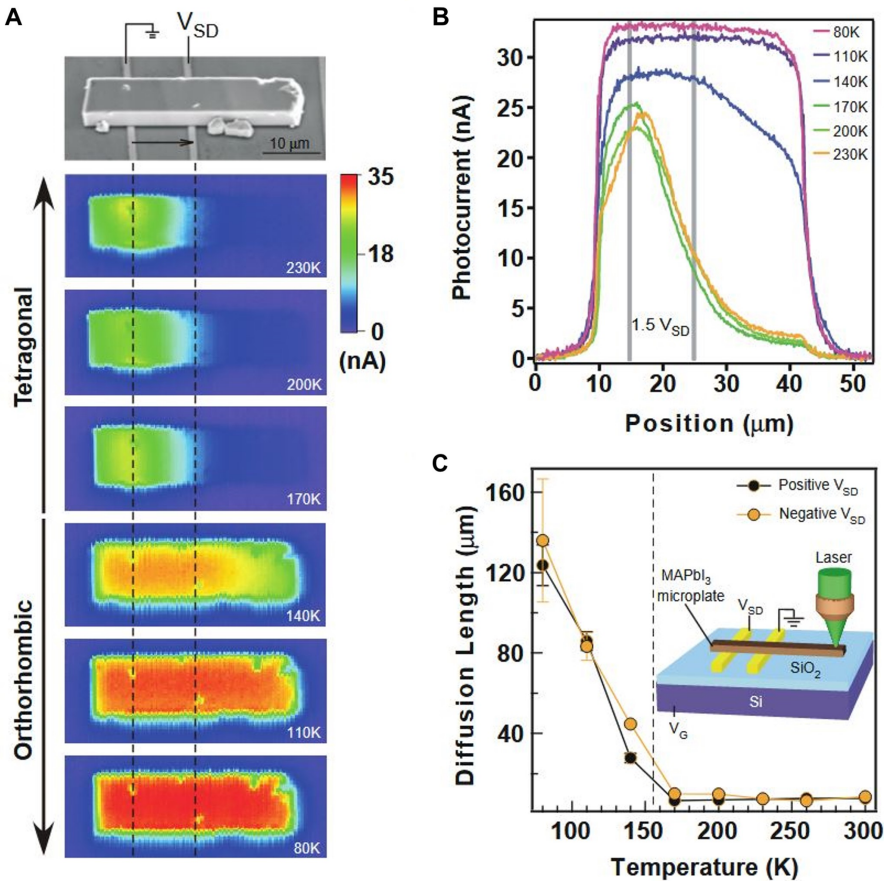

Figure 3.5: SPCM profiles for a different device. (A) SEM image and photocurrent maps at various temperatures. Dashed lines indicate electrode placement. (B) Photocurrent profiles along the micro-plate axis at various temperatures, taken during warming process with 200 nW laser and $V_{SD} = 1.5$ V. Grey vertical lines indicate electrode placement. (C) Temperature dependent carrier diffusion length extracted by fitting photocurrent distributions by a cosh function in (B).

3.3.2 Transient Photocurrent and an Implied Enormous Mobility

Transient photocurrent measurements are then performed to obtain carrier lifetime at various temperatures (**Appendix Figure A.2**). The carrier lifetime increases from less than 0.5 μs (our temporal resolution limit) above T_c to about 2 μs at 80 K for the same device as in **Figure 3.2**. From this lifetime and the measured L_D, we estimate a carrier mobility ($\mu = qL_D^2/\tau k_B T$) of 3 $\times$ 10^4 cm^2 / V s at 80 K, which is one order of magnitude higher than the highest reported values[147] [148] (Table 3.1). Lifetimes differ slightly across devices, ranging from $<$ 0.5 to 2 μs at 80 K (see lifetime measurements in another device in **Appendix Figure A.2B**), but mobility values are consistently high, on the order of 10^4 - 10^5 cm^2/ V s.

sample	$\mu(cm^2/Vs)$	$\tau(\mu s)$	$L_{diff}(\mu m)$	T(K)	method	reference
polycrystal	0.65	0.1	0.13	300	transient PL	[11]
single crystal	164	82	175	300	SCLC	[12]
single crystal	60	2700	650	300	Hall	[149]
polycrystal	66	-	-	300	Hall	[150]
polycrystal	0.1 10^{-6}	- -	- -	80 300	field effect	[143]
polycrystal	6.2 16	5 -	>5 -	300 165	TRMC	[136]
polycrystal	60-75	-	-	300	TRMC	[151]
polycrystal	10	-	-	300	SPCM	[120]
single crystal	115 3-15 (hole)	10 -	<55 27-65	300 300	TRMC SPCM	[119]
polycrystal	35 150	- -	2.5 -	300 80	THz	[131]
polycrystal	2000	-	-	15	THz	[147]
polycrystal	27 150	- -	- -	300 77	THz	[135]
single crystal	135 635	- -	- -	290 100	time of flight	[148]
single crystal	3×10^4 -	2 <0.5	200 10	80 300	SPCM	this work[60]

Table 3.1: Experimentally obtained carrier mobility, lifetime, and diffusion length in $MAPbI_3$.

The observed highly non-local photocurrent indicates efficient transport of photogenerated charge carriers, which can generally be understood by four possible mechanisms: (a) photon recycling, (b) exciton polariton condensate, (c) free charge carrier diffusion, and (d) free exciton diffusion. Here, we will show that the first three mechanisms are unlikely:

(a) Photon recycling via re-absorption/re-emission,[81] one of the most popular extended diffusion reasonings, is unlikely to account for the observed 200 μm photocurrent decay, as the optical loss through light escaping micro-plate surfaces alone would result in a maximum of 20 μm decay length according to our calculation, even when assuming unity photoluminescence efficiency. We perform a simple model to estimate the photocurrent decay length solely due to photon recycling, without considering carrier diffusion. To estimate an upper limit of the decay length, the radiative recombination efficiency η is taken as 100%.

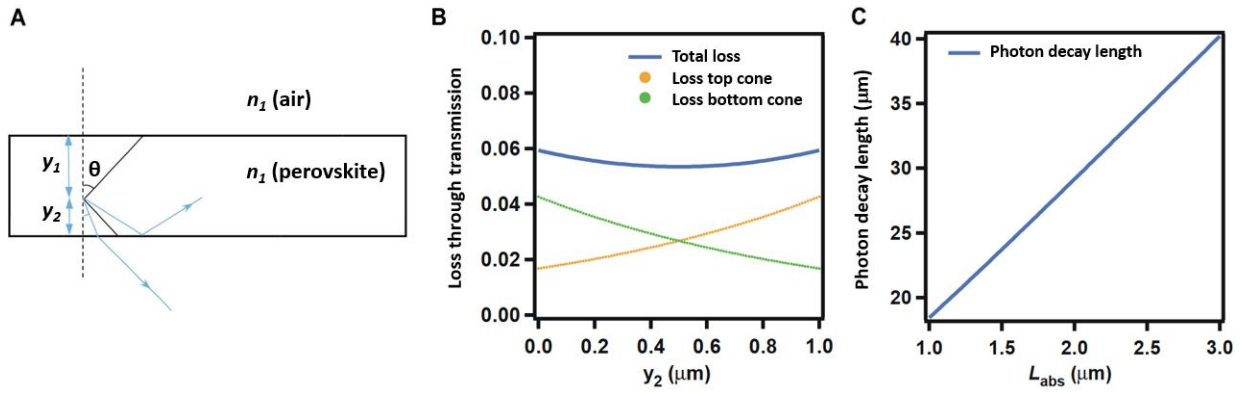

Figure 3.6: (a) Schematic of a photon traveling in a perovskite micro-structure and optical loss through transmission at the interface. (b) Calculated proportion of optical loss as a function of position of re-emitted light, where y_2 is the distance to the bottom surface, with light penetration depth of $L_{abs} = 1.12$ μm at 80 K. (c) Calculated photon travelling decay length as a function of the light penetration depth, with the optical loss values calculated in (b).

If we assume emission is isotropic, the fraction of the optical power escaping through the top/bottom surfaces (**Figure 3.6**) can be calculated as,

$$P_{loss} = \frac{\int_0^{\theta_m} T(\theta) \exp(-\alpha y_1/\cos\theta) \sin\theta d\theta + \int_0^{\theta_m} T(\theta) \exp(-\alpha y_2/\cos\theta) \sin\theta d\theta}{\int_0^{\pi} \sin\theta d\theta} \tag{3.4}$$

where $\theta_m = \arcsin(n_1/n_2)$ is the critical angle for total internal reflection (Fresnel equations), $T(\theta)$ is the angle-dependent transmission coefficient, and $\exp(-\alpha y_{1(2)}/\cos\theta)$ describes the light attenuation. At 80 K, an average light penetration depth of $L_{abs} = 1.12$ μm is used, which corresponds to an absorption coefficient $\alpha = 0.886$ μm^{-1}, based on the typical photoluminescence and absorption spectra of $MAPbI_3$.[152] [153] In this case, P_{loss} is in the range of 5.35 - 5.94%, depending on the height of the emission center (**Figure 3.6A**). Using the average P_{loss}, we estimate the decay length by considering that the power is reduced by P_{loss} after light travels L_{abs} and re-emits isotropically. This leads to a decay length of $-L_{abs}/ln(1 - P_{loss}) = 19.8$ μm, much less than the observed decay length. The above calculation considers a micro-plate with a width much larger than the thickness. For a micro-beam with a narrow width comparable to the thickness, emission can also escape from the side walls, thus leading to an even shorter decay length. Therefore, we conclude that photon recycling cannot account for the observed long L_D.

(b) Exciton polariton condensate[154] requires a micro-cavity structure to confine the light. Our micro-plate crystals do not have such a structure and optical loss would result in a short decay length.

(c) Free minority carrier diffusion appears plausible but demands a 400-fold increase in mobility, more than one order of magnitude higher than the highest reported values in the literature,[147] [148] to account for the rapid increase of L_D below T_c from 160 K to 80 K. Furthermore, existing charge carrier and polaron models predict $\mu \sim T^{-1.5}$ and a mobility change of only a factor of 3 from 160 K to 80 K.[134]

3.3.3 Efficient Exciton Transport Hypothesis

The above consideration leads us to attribute the origin of the highly non-local photocurrent at low temperature to efficient exciton transport, mechanism (d). A relatively large value of exciton binding energy E_B (larger than 20 meV) in the orthorhombic phase discontinuously drops to below 10 meV at room temperature tetragonal phase.[155] This is fairly consistent with the value of 16 ± 2 meV found in the orthorhombic phase and a few meV in the tetragonal phase in $MAPbI_3$ by magnetic field dependent optical absorption.[58] Using an effective-interaction-potential model,[156] [157] we calculated the exciton binding energies of $MAPbI_3$ in good agreement with the measurements, 20.1 meV and 9.1 meV in the low and high temperature phases, respectively, as shown in **Figure 3.7B**.

It is known that electron (hole)-phonon interactions are not negligible in halide perovskites, and in fact, both free carrier and excitonic states should be considered with polaronic corrections. Our model appropriately incorporates the coupling of the electron-hole pairs to LO-phonon modes of the medium to provide a better description of the exciton state beyond the simple hydrogenic model.[60] Electron and hole band masses, static and high-frequency dielectric constants, and energies of LO-phonons are the material parameters that determine the excitonic properties in this model. In $MAPbI_3$, the coupling of charge carriers to phonons is not weak enough for a satisfactory perturbative description of excitons, where the masses of electrons and holes would be renormalized to polaron masses and the two polarons would interact through a statically screened Coulomb interaction. Rather, the Bohr radius of the excitonic state is comparable to or even smaller than the electron and hole polaron-radii so that the polarization fields of the bound electron-hole pair partially cancel, calling for a more elaborate approach.

These excitonic binding energies suggest that excitons are unlikely to form at room temperature but they become significant at low temperatures. The exciton fraction over the total carriers is shown in **Figure 3.7C**, calculated following the approach in a previous

report,[57] and using the temperature-dependent exciton binding energy.[155] The abrupt increase in exciton fraction across the phase transition is a result of phase-dependent exciton binding energies. Note that the exciton fraction sensitively depends on the total carrier density, as high carrier density promotes exciton formation. The total carrier density in our sample is on the order of 10^{15} - 10^{16} cm^{-3}, estimated from the laser power and carrier lifetime.

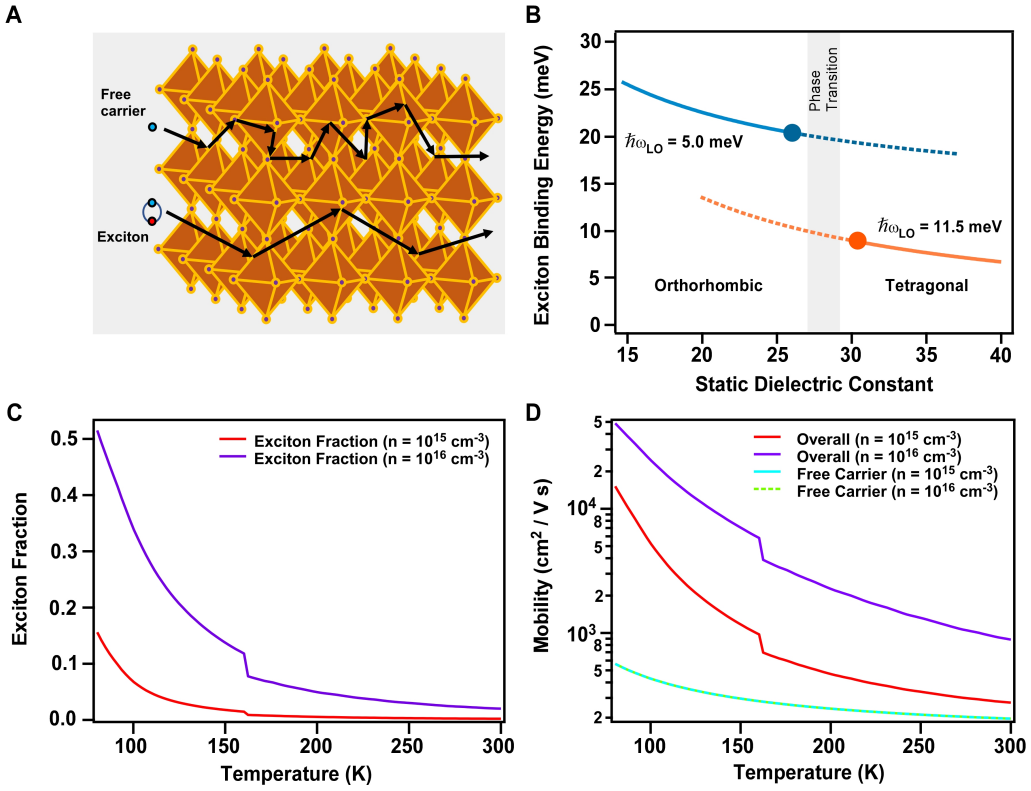

Figure 3.7: Calculation of free exciton and free carrier mobilities. (A) Visualization of free carrier versus exciton scattering in halide perovskites (scattering lengths not to scale). (B) Exciton binding energy, calculated taking into account polaronic effects, and as a function of static dielectric constant and LO phonon frequencies, which are phase-dependent. (C) Calculated exciton fraction as a function of temperature, at carrier densities $n = 10^{15}$ cm^{-3} and $n = 10^{16}$ cm^{-3}, showing significant exciton population at low temperatures. (D) Calculated free carrier mobility and overall mobility as a function of temperature. Free carrier mobility is independent of carrier density, while overall mobility is increased at higher densities due to higher exciton fractions.

The rapid increase of mobility at low temperature can then be understood as the exponential increase of exciton fraction with decreasing temperature. In this exciton model, the record-high mobility indicated by the long L_D does not contradict the non-excitonic free

carrier mobilities reported by earlier works. Even though an exciton is charge neutral, its mobility can be defined from its diffusion coefficient in analogy to charge by Einstein relation $\mu = qD/k_BT$. Charge neutral excitons create photocurrent when electron and hole pairs are separated as a result of band bending near the contact.

We hypothesize that the reason for the highly efficient exciton transport is the dipolar nature of excitons. Since dipole fields are shorter ranged than monopole fields, longitudinal optical (LO) phonons interact significantly less with excitons than with free carriers. Moreover, static ground-state excitonic dipoles do not exist in the centrosymmetric orthorhombic phases, and can only be dynamically induced by other charge fluctuations such as LO phonons. As a result, the scattering of excitons is expected to be less frequent than that of free carriers or charged polarons. To estimate the relative scattering rates of free carriers and excitons, we consider the interaction strength of an induced excitonic dipole, given by the polarizability $\alpha = \frac{18a_0^3}{4}$ of an exciton within a hydrogenic model,[158] with LO phonon charge fluctuations. Here, a_0 is the exciton Bohr radius. Compared to the interaction between free carriers (holes) and LO phonons, we find that the exciton-LO phonon interaction strength, or probability amplitude for scattering, is reduced by a factor of $\sqrt{\gamma} = \left(\frac{\alpha}{\epsilon_\infty R_x^4}\right) / \left(\frac{1}{R_h}\right)$. Here, $R_h = \sqrt{\frac{\hbar}{2m_h\omega_{LO}}}$ and $R_x = \sqrt{\frac{\hbar}{2m_x\omega_{LO}}}$ are the hole and exciton polaron radii that characterize the length scales of LO fluctuations around these species, with masses m_h and m_x respectively. The scattering rate, or probability, is therefore reduced by a factor of $\gamma = \left(\frac{18a_0^3 R_h}{4\epsilon_\infty R_x^4}\right)^2$.

We take the electron mass to be $m_e = 0.190$ and the hole mass to be $m_h = 0.230$, leading to a relatively well-established[58] [159] value of the exciton reduced-mass $\mu = 0.104$, in units of bare electron mass. This value is shown to be almost invariant[58] in the orthorhombic-tetragonal phase transition of $MAPbI_3$. We take the high-frequency dielectric constant to be $\varepsilon_\infty = 5.4$ in both phases, a value reported as a statistical average over a dozen experimental studies.[159] Temperature (phase)-dependent values of static dielectric constant and the effective (average) energy of the LO phonon modes that couple to the free carrier dynamics are still debated in the literature. For the static screening constant we used $\varepsilon_\infty = 30.4$

in the room temperature phase, a value reported as an average of four reported measurements.[159] In the orthorhombic phase, we take the static screening constant to be 25.7, since it is expected to be smaller possibly due to frozen rotational modes of the MA cation at low temperatures.[160] The optical phonon energy to be used in the calculation is also phase-dependent. By investigating the temperature dependence of emission line broadening, the energy of interacting LO phonon modes in the tetragonal phase of $MAPbI_3$ was determined to be 11.5 meV.[161] In the low temperature phase, low energy (4 - 8 meV) optical modes of the Pb-I lattice become dominant so that we take the effective phonon energy to be $\hbar\omega_{\mathrm{LO}} = 5$ meV. Using these parameters, the variational calculation, incorporating a detailed effective interaction potential for the electron-hole pair, and the polaronic self energy terms, gives a binding energy value of 20.1 meV in the orthorhombic phase, and 9.1 meV in the tetragonal phase, as previously mentioned. Correspondingly, the calculated exciton radius shrinks from 3.37 nm to 2.95 nm as the temperature is lowered.

Using the above mentioned values for $MAPbI_3$, we find that exciton scattering from LO phonons is reduced by a factor of $\gamma = 5 \times 10^{-4}$. This is a lower bound for γ, as other scattering mechanisms could be present for excitons. In **Figure 3.7D**, we plot the overall mobility, weighted by free carrier and excitonic contributions. The free-carrier mobility is calculated using the Kadanoff mobility,[134] while the exciton mobility was taken to be larger by a factor of $1/\gamma$. In **Figure 3.7D**, we show that reduced excitonic scattering at the value of $\gamma = 6 \times 10^{-3}$, leads to increases in low-temperature mobility comparable to measured values in our devices.

3.3.4 Gate Effects on Carrier Diffusion - $MAPbI_3$

Finally, we present the field effect on carrier diffusion in halide perovskite micro-plate FETs. In the dark, the conductance increases at positive V_G indicating the device is n-type (**Figure 3.8A**). The gate dependence shows significant hysteresis at room temperature as explained by gate induced ion migration.[143] The hysteresis is greatly reduced at lower

temperature, as ion migration is suppressed. By assuming a parallel plate capacitance (a combination of vacuum gap and oxide layer), an apparent field-effect mobility on the order of 0.01 cm^2 / V s can be extracted from the gate dependence at 80 K (**Figure 3.8A**). This apparent mobility value does not represent the real carrier mobility of the material because of large contact barriers evidenced by the nonlinear $I - V_{SD}$ curves (**Figure 3.8A** and **Appendix Figure A.3**). Furthermore, this low mobility value does not contradict with the high mobility value indicated by the long photocurrent decay length, as the gate dependence measures the mobility for free carriers or charged polarons rather than excitons.

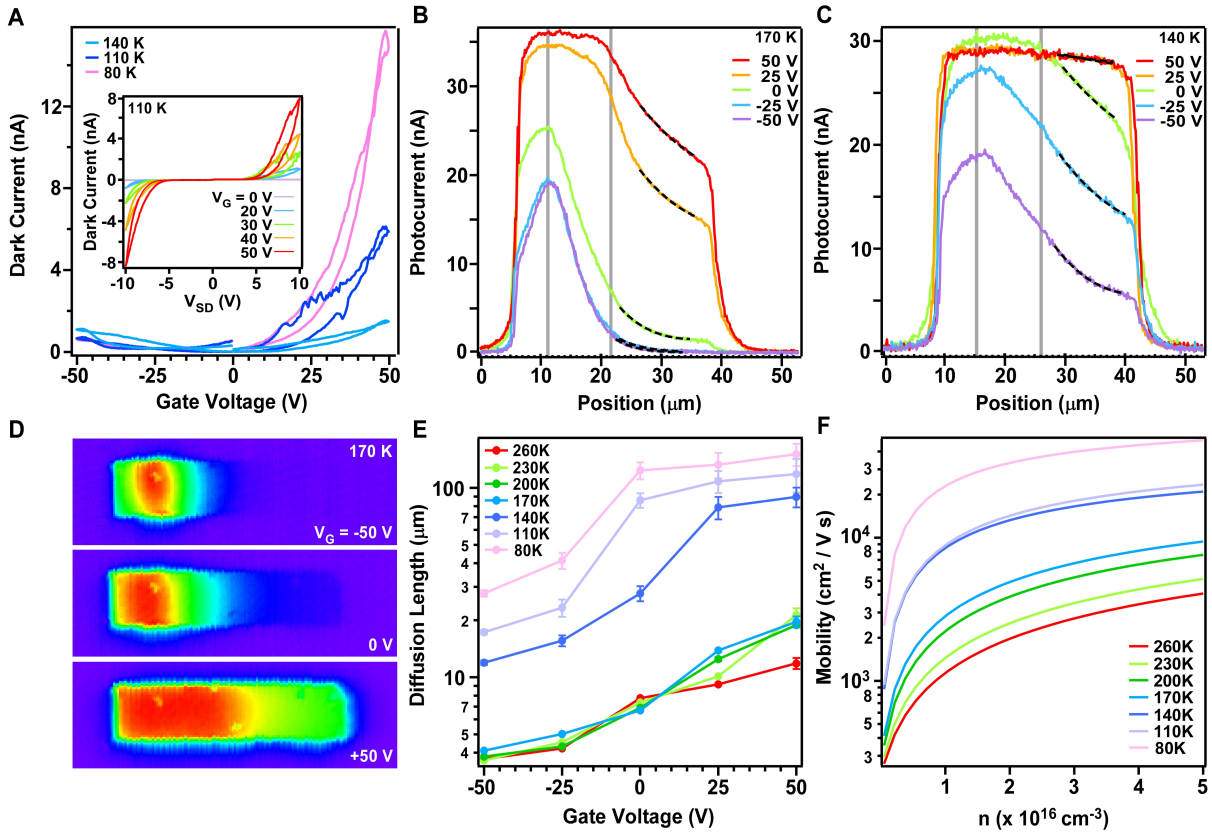

Figure 3.8: Field effect on carrier diffusion. (A) Dark current as a function of V_G at fixed V_{SD} = 10 V and various temperatures. Inset: Dark $I - V_{SD}$ curves at various V_G at 110 K. (B) and (C) show SPCM profiles with varying gate voltage and fixed bias of 1.5 V at 170 K (tetragonal phase) and 140 K (orthorhombic phase), respectively. Grey vertical lines indicate electrode placement. (D) Normalized photocurrent maps showing diffusion enhancement (suppression) at positive (negative) gate voltage at 170 K. (E) Carrier diffusion length at various temperatures as a function of gate voltage. (F) Simulated mobility values as a function of overall carrier density at various temperatures.

Photocurrent distributions sensitively depend on V_G (**Figure 3.8B-D**). At positive V_G, the photocurrent magnitude increases, likely caused by the reduced sample resistance and/or enhanced band bending at contact. The carrier diffusion length also significantly depends on the gate voltage, changing by a factor of 8 at low temperature as V_G varies from -50 V to 50 V (**Figure 3.8E**). Such a strong electric field control of carrier diffusion has not been reported before in halide perovskites. We consistently observe that L_D increases (decreases) at positive (negative) V_G. In the n-type device, this trend indicates that increasing the majority carrier (electron) concentration enhances the diffusion of the minority carrier (hole) or exciton. This behavior cannot be understood by the lifetime reduction at high majority carrier density as in other semiconductor nano-devices.[127] [162] Instead, this unusual gate dependence is consistent with the exciton model. The higher carrier concentration at positive V_G increases the probability of exciton formation, leading to a larger exciton fraction and hence higher overall mobility (**Figure 3.7**). The calculated mobility values taking into account exciton formation (**Figure 3.8F**) follow well with the general trend of the experimental results.

In summary, we observed temperature and gate dependent carrier diffusion in single-crystal $MAPbI_3$ micro-structures. L_D remains about 10 μm in the tetragonal phase, but increases sharply to 200 μm at 80 K in the orthorhombic phase. L_D also increases with majority carrier (electron) concentration tuned by gate voltage. The rapid increase of L_D can be understood by formation and efficient transport of excitons at low temperature. The phonon-scattering rate of excitons is significantly suppressed as a consequence of their dipolar nature, compared to free carriers and charged polarons. This hypothesis is supported by calculated temperature and carrier concentration dependent mobilities that are in excellent agreement with the experimental results. Though the relatively low excitonic binding energy in $MAPbI_3$ suggests that excitonic effects only become important at low temperature in this material, excitons are expected to play a significant role at room temperature in low

dimensional halide perovskites.[21] [163] This work provides valuable insight on understanding the interplay among free carriers, excitons, and phonons in HOIP systems.

3.3.5 Where?

This set of experiments was performed entirely at UC Davis. All optoelectronic measurements were taken in Dr. Yu's laboratory, with fabrication assistance from CNM2, and XRD characterization by Dr. Taufour's research team. Theoretical work was performed by our collaborators at the Molecular Foundry and the Izmir Institute of Technology.

3.4 Highly Mobile Excitons in Single Crystal $MAPbBr_3$ Micro-Structures

In materials with enormous E_B values, excitons dominate over free charge carriers upon photoexcitation. Consequently, one of the limiting factors for power conversion efficiency in purely organic solar cells is the exciton diffusion length (L_D), which is rather short, on the order of 10 nm.[54] In this case, the formation of excitons, their short diffusion lengths, as well as the difficulty of their separation into free charge carriers have posed significant challenges facing the applications of these materials in photovoltaics. However, as previously mentioned, excitons can also become highly mobile in inorganic materials, with mobility reaching as high as 10^6 cm^2/Vs in silicon[56] and 10^5 cm^2/Vs in GaAs quantum wells.[164] As we discovered in our study on $MAPbI_3$ micro-structures at low temperature, 3D HOIPs can have mobile excitons too, under the right conditions. The limits of exciton mobility and diffusion length in single crystal HOIPs are still unclear, but we've now begun to at least shed some light on the subject.

In the previous section, we discussed the observation of L_D increasing rapidly as temperature decreased in single-crystal $MAPbI_3$ micro-structures, which can be understood by the exponentially growing fraction of highly mobile, free excitons at low temperature.[60] [53] $MAPbBr_3$ has a larger E_B than $MAPbI_3$ and hence provides a convenient platform to further study excitons. Here, we investigate temperature-dependent dynamics and transport of coexisting photogenerated excitons and free carriers in $MAPbBr_3$ single crystal micro-plate FETs, by using energetically, spatially, and temporally resolved optical and optoelectronic techniques. By studying single crystal structures with nano/micro-scale thickness, we once again eliminate the complications caused by grain boundaries while also enabling in-situ gate tuning of the Fermi level.[143] In order to directly obtain exciton or carrier diffusion length, we use SPCM, a powerful experimental technique that provides spatially resolved photocurrent mapping and insights on carrier transport.[88] [90] [118] [121] SPCM has been used to study exciton diffusion in both HOIP systems[165] and transition metal dichalcogenides.[166] [167]

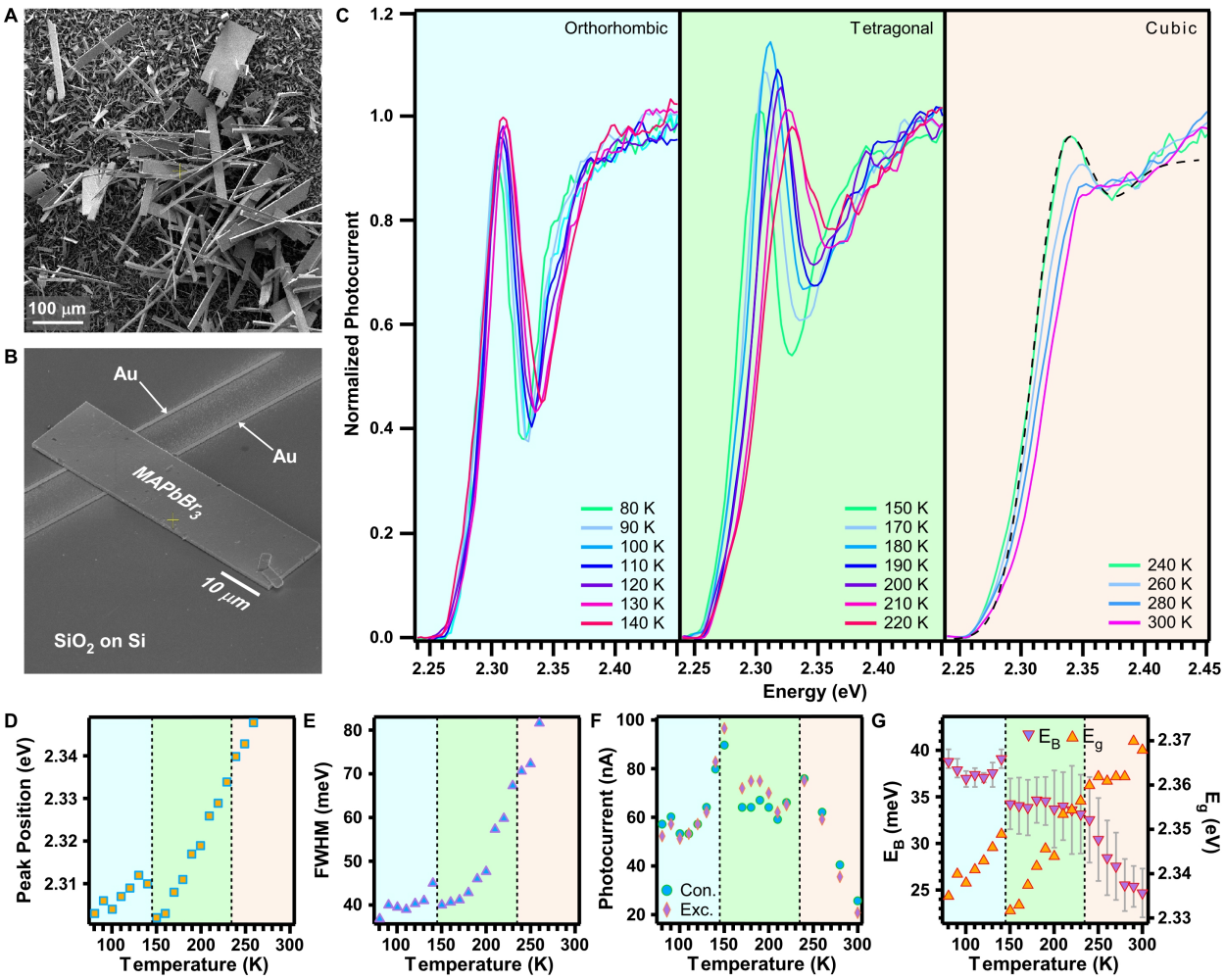

Figure 3.9: Temperature dependent photocurrent spectra and Elliott fittings of a typical $MAPbBr_3$ micro-plate device. (A) SEM image of the as-grown samples. (B) SEM image of a $MAPbBr_3$ micro-plate (74 μm long, 640 nm thick) connected to bottom Au contacts. (C) Photocurrent spectra at various temperatures. Photocurrent is normalized at 2.45 eV. The laser power is about 5 μW and defocused to an area of about 4000 μm^2. $V_{SD} = 2$ V is applied. The dashed, black line represents an Elliott fitting example. (D) and (E) Excitonic peak position and FWHM as functions of temperature, respectively. (F) Temperature dependent photocurrent values taken from 2.45 eV (Con.) and the excitonic peak (Exc.), respectively. (G) E_B and E_g as a function of temperature, extracted from (C) via the Elliott formula.

Single crystalline micro-structures of $MAPbBr_3$ are synthesized following a dissolution and recrystallization process, as discussed in Chapter 2.[84] Structures with thickness ranging from 300 nm to 2 μm and length up to 200 μm are produced with well defined facets and smooth surfaces (**Figure 3.9A,B**). To avoid exposing the sample to detrimental solvent processing, the as-grown crystals are directly transferred via micro-fiber to pre-patterned

Cr/Au electrodes on SiO_2 coated Si substrates to fabricate FETs. The devices are quite insulating in the dark but become conductive under light. The nonlinear current-voltage relation (**Appendix Figure B.4**) indicates large contact barriers.

3.4.1 Temperature-Dependent Photocurrent Spectra

Temperature-dependent photocurrent spectra are measured with a defocused laser, so that the entire micro-plate is uniformly photoexcited. As temperature is reduced, a distinct peak is developed, indicating the exciton resonance (**Figure 3.9C**). The exciton peak position first redshifts when the temperature is reduced, but then abruptly blueshifts at 140 K (**Figure 3.9D**), corresponding to the tetragonal-orthorhombic phase transition. It then continues to redshift below 140 K. This trend is similar to previous reports[112] [168] [169] and is observed in our PL spectra measurements (shown later). The excitonic peak width narrows from 80 to 40 meV as the temperature is reduced from 260 K to 170 K and then stays around the same level except for a spike at the 140 K phase change (**Figure 3.9E**). The peak width at low temperature is larger than the value expected from phonon broadening,[170] indicating sample inhomogeneity due to the relatively large surface to volume ratio and the large laser spot size. We perform Elliott fittings, convolved with Gaussian functions to account for thermal broadening, on the photocurrent spectra to extract E_B and bandgap energy (E_g)[169] [171] [172] [173] [174] [175] [176] [177] (**Figure 3.9C,G** and **Appendix Figure B.5**). E_B grows steadily until the first phase change, where it then stagnates around 34 meV. It then abruptly jumps to about 39 meV at the second phase change, simultaneous with a sharp blueshift in E_g.

3.4.2 Extracting E_B Using The Elliott Model

The basic Elliott formula for an absorption spectrum can be written as

$$\alpha(\omega) = A \cdot \theta(\hbar\omega - E_g) \cdot \frac{\pi e^{\pi x}}{\sinh(\pi x)} + A \cdot R_{ex} \sum_{n_{ex}=1}^{\infty} \frac{4\pi}{n_{ex}^3} \cdot \delta(\hbar\omega - E_g + R_{ex}/n_{ex}^2) \qquad (3.5)$$

where A is related to the interband transition matrix element, $\hbar\omega$ is the photon energy, θ is the Heaviside step-function, E_g is the bandgap energy, R_{ex} is the exciton Rydberg energy, n_{ex} is the principle quantum number, and x is defined to be $\sqrt{\frac{R_{ex}}{\hbar\omega - E_g}}$. Here, R_{ex} is equal to the exciton binding energy E_B when $n_{ex} = 1$.

Due to the nature of our data collection procedure (photocurrent rather than absorption), we expect the Elliott model to imperfectly handle the spectra fittings. We therefore interpret the output fitting parameters of E_B and E_g to be approximations, and attach error to their values by attempting the fit in more than one way. The inaccuracy of the fit at higher energies in the continuum is explained by the effects of Sommerfeld enhancement on the absorption coefficient[171], and is less interesting for our study. The convolved Elliott formula without a Sommerfeld term is expected to saturate at high energy, as shown in our plots, rather than continue to increase.

The interesting discrepancy between our experimental data and the model is what happens to the excitonic peak as temperature is decreased. The model predicts both the peak amplitude as well as the energy gap between peak and continuum to increase as E_B increases. In our data, we see this trend initially, but as temperature decreases and peak separation becomes more distinct, we do not see peak amplitude rise accordingly. By 140 K, the excitonic peak is clearly well-separated from the continuum edge, implying a large E_B, but the E_B value required to create this gap also calls for a much taller peak.

Therefore, we extract our E_B and E_g values by attempting to fit the spectra from the low and high energy sides of the peak, separately, as shown in **Appendix Figure B.5**. Fitting from the low energy side produces smaller E_B values while fitting from the high energy side produces larger values. This makes sense, as the low energy side assumes the peak has been reached, whereas the high energy side tries to capture the gap between peak and continuum and does not know how high the peak reaches. This provides us with a form of minimum and maximum bound on the E_B, which we then average to give the values listed in the main text.

Furthermore, we also make use of how well-resolved the peaks are from the continuum at low temperature. Since the gap between the peak center and the continuum edge is directly related to the E_B, we can look at the energy difference between peak center and half way up the continuum edge to get another estimate on the E_B. For example, at 110 K, the energy gap between the peak center and halfway up the continuum edge is about 38 meV, which agrees well with our fitting value. For the data collected between 80 K and 140 K, the error bars are set to reach between the min and max values of the fittings and are relatively small compared to higher temperatures due to the distinct separation of peak and continuum. For the data collected between 150 K and 300 K, the error bars are again set to reach between min and max values of the fittings but then additionally increased in proportion to temperature, since excitonic and continuum components begin to mix significantly as temperature increases.

As the excitonic peak grows and shifts with decreasing temperature, binding energies appear to increase while bandgap energy decreases. Two structural phase changes occurred across this range of temperatures, the cubic to tetragonal transition at about 235 K, and the larger (in terms of lattice distortion) tetragonal to orthorhombic transition around 145 K.[178] E_B grows steadily until the first change, where it then stagnates around 34 meV. It then abruptly jumps to about 39 meV at the second phase change, simultaneous with a sharp blueshift in E_g. We have thus far found no other report showing spectral behavior with such clear separation of excitonic and continuum components for 3D HOIPs. Interestingly, the Elliott fittings begin to fail as temperature decreases, since the Elliott model predicts the exciton peak to grow in amplitude, relative to the continuum, as separation from the continuum edge (and therefore E_B) increases. In the data, however, the peak amplitude increases at first but then begins to decrease (**Figure 3.9**), which can be understood by the difficulty of splitting excitons at the contact. This deviation from the Elliott model can be related to our spectra being obtained via photocurrent, rather than via optical absorption.

3.4.3 Temperature-Dependent SPCM - $MAPbBr_3$

We then perform SPCM at various temperatures. A focused laser with a spot size of about 1 μm is raster scanned while photocurrent is mapped as a function of laser position. A source-drain bias (V_{SD}) is applied to improve the photocurrent signal. The photocurrent cross sections along the micro-plate axis are shown in **Figure 3.10A**. At 300 K and 260 K, photocurrent is only observed when the laser is close to the reversely biased contact, with a decay length of 2 - 3 μm. Photocurrent appears both inside and outside the source-drain channel. The photocurrent generated by photoexcitation in the electric-field-free region outside the channel is caused by the diffusion of the photogenerated carriers. Below 220 K, the photocurrent profile looks slightly asymmetric with a longer decay length in the channel (most clear at 140 K). This is likely because the contact barrier is smaller at low temperature, creating a stronger in-channel electric field. Consequently, the carrier drift leads to enhanced photocurrent and longer L_D up to 7 μm (**Figure 3.10E**) in channel.

Interestingly, a long tail with a smaller magnitude in the photocurrent distributions appears below 220 K (**Figure 3.10A**), in addition to the short decay component. A double-exponential fitting yields a decay length of 100 $\pm$ 40 μm for the long-range component at low temperatures (**Figure 3.10E**). The large uncertainty arises from the micro-plate's length, which is itself limited by the synthesis method. The photocurrent decay profiles are found to be insensitive to the excitation photon energy range used in the experiment (2.25 - 2.48 eV). The short decay length is comparable to the electron (minority carrier) diffusion length (1 - 5 μm) reported in single crystal $MAPbBr_3$,[179] but the long decay length is much larger than previously reported values. The long-range component's magnitude peaks at 140 K and is about one quarter of the short component's magnitude (**Figure 3.10D**). As you may recall, a long-range photocurrent decay profile was also observed in our previously mentioned work on $MAPbI_3$ micro-plates.[60] However, the photocurrent behavior in $MAPbBr_3$ is drastically different from that in $MAPbI_3$. First, the photocurrent profile in $MAPbI_3$ followed well

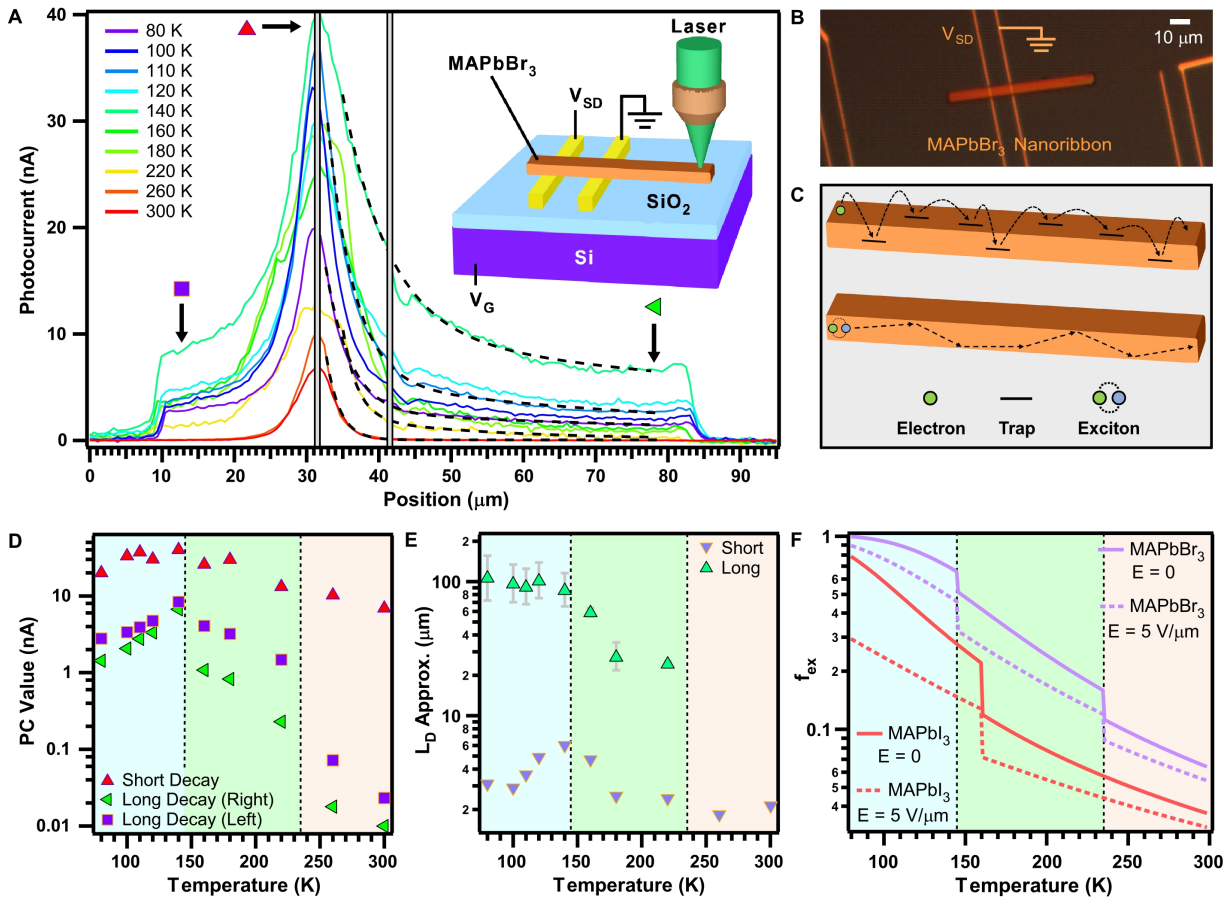

Figure 3.10: Spatially resolved photocurrent. (A) Photocurrent distributions along the microplate axis at various temperatures. The laser power is 2 μW at 510 nm. V_{SD} = 4 V (5 V for 260 and 300 K) is applied across the channel. Dashed black lines represent double-exponential fittings of the photocurrent decays. Inset shows the SPCM schematic. (B) Optical image of a microplate device. (C) Schematics for potential mechanisms, including trap hopping (top) and exciton transport (bottom). (D) Photocurrent magnitudes plotted against temperature, taken from SPCM profiles in (A), at three locations along the device (indicated with markers): at the contact (red triangles), at the right end (green triangles), and at the left end (purple squares). (E) L_D extracted from double-exponential curve fits in (A). There is no long-range component for 260 and 300 K. (F) Calculated exciton fraction as a function of temperature for $MAPbI_3$ and $MAPbBr_3$, in the field free region and the depletion region, respectively.

with a single exponential function, while $MAPbBr_3$ shows two distinct decay components. Second, the photocurrent decay length in $MAPbI_3$ reached 200 μm only at 80 K, while the decay length in $MAPbBr_3$ increases to 100 μm around the orthorhombic phase transition temperature (140 K).

To better understand the observed long decay length, we perform time-resolved PL (TRPL) at various temperatures. PL spectra exhibit a well defined peak at 11 K, which

shifts to higher energy as temperature increases, consistent with the photocurrent spectra (**Figure 3.11A,B**). The FWHM was about 10 meV at 11 K and increases to 15 meV at 80 K (**Figure 3.11C**), significantly narrower than the peak width measured in photocurrent spectra. Initially, the PL intensity decays rapidly, on a timescale within a few ns. This very fast decay can be attributed to Auger recombination[173] or surface recombination.[180] As temperature decreases, a slower component of 10's of ns is observed (**Figure 3.11D**), and an even slower component of 100's of ns appears below 80 K. However, at the more relevant temperatures for our photocurrent studies, 80 K and above, this extra slow component is absent. These recombination lifetimes are also consistent with literature values.[180] [181] [182]

To examine the potentially slow nonradiative carrier recombination undetected by TRPL, we also perform time-resolved photocurrent (TRPC) by using a photoelastic modulator (PEM) based chopper (B.6). TRPC measurements yield a photocurrent decay time of $\sim$1.2 μs, which is an upper bound of the real carrier lifetime because of the temporal resolution limitation of the instrument. Using the upper limit of the above determined lifetime of $\tau = 1.2$ μs and an L_D value of 100 μm at 80 K, we extract a lower bound diffusion coefficient of $D = L_D^2/\tau \approx 83\ cm^2/s$, which corresponds to an enormous mobility of $\mu = qD/k_BT \approx 10^4$ cm^2/Vs. Such a high carrier mobility is unlikely achieved by trapped charges hopping among traps (depicted in **Figure 3.10C, top**). In addition, the hopping mobility is usually suppressed at lower temperature and inconsistent with the longer L_D.

We now discuss the potential mechanisms that may account for the observed long-range photocurrent tails. Exciton-polaritons with a propagation distance of 60 μm have been reported in $CsPbBr_3$ microcavity structures with distributed Bragg reflectors (DBR).[154] Our micro-plate devices are not embedded in such photonic structures and the observed 100 μm photocurrent decay lengths do not require DBR. Without manufactured mirrors to confine the photons within the cavity, optical loss through PL emitted light escaping through the sample surfaces is expected, making it difficult to sustain such low-loss and long-distance polariton transport. Indeed, in $MAPbBr_3$ micro/nanowires without DBR,

exciton-polaritons were only demonstrated in microwires shorter than 20 μm.[183] Therefore, exciton-polariton condensation is not a likely mechanism to account for the observed 100 μm photocurrent decay lengths in our micro-plates without manufactured cavities. Furthermore, photon recycling unlikely accounts for the observation because of the optical loss through micro-plate surfaces.[60]

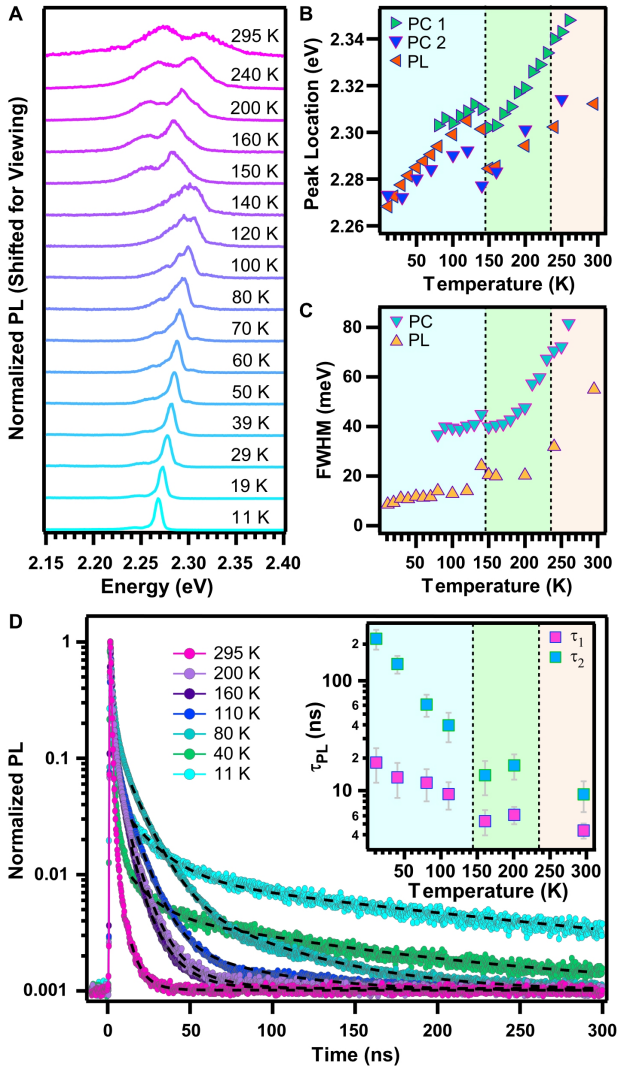

Figure 3.11: PL spectra and TRPL measurements under 405 nm excitation. (A) Normalized PL spectra across a wide range of temperatures, vertically shifted for better viewing. The average laser intensity varies from 3×10^{-2} to 1.6 W/cm^2 as the PL emission is much stronger at lower temperature. (B-C) Comparison of PL and photocurrent peak energy (B) and FWHM (C) as a function of temperature. PC values are extracted from **Figure 3.9** and another device. (D) Normalized TRPL measurements as a function of temperature, with bi-exponential fittings used to extract carrier lifetimes. Average laser intensity varies from 0.3 to 14 W/cm^2 as temperature increases. Inset, extracted carrier lifetimes as a function of temperature.

Free carrier diffusion is also unlikely to explain the observed highly non-local photocurrent in $MAPbBr_3$. Under photoexcitation, the excitons and free carriers quickly reach a dynamic balance through the fast pairing and dissociation process occurring on a picosecond timescale,[184] reaching a pseudo-equilibrium. Therefore, the fractions of the coexisting excitons and free carriers can be quantitatively estimated by the Saha-Langmuir equation[57] (see **Equation 1.1**). At sufficiently low temperature ($k_BT \ll E_B$), a majority of photoexcited charge carriers are bound into pairs. Using an exciton binding energy of 40 meV (as extracted from our photocurrent spectral data) and a hole concentration of 10^{16} cm^{-3} in the *p*-type material, we estimate from Saha's equation that photogeneration creates 99 % excitons and 1 % free carriers at 80 K (see details in Appendix B: $MAPbBr_3$). This calculation is also supported by the very pronounced exciton peaks observed in our photocurrent and PL spectra at low temperatures. Furthermore, the diffusion length remains extremely long at 10 K (**Appendix Figure B.7B**), where E_B is 40 times larger than k_BT. Thus, it is highly unlikely that the observed long diffusion lengths originates from free carriers.

We attribute the strongly temperature dependent non-local photocurrent to efficient exciton transport.[62] Similar to $MAPbI_3$, the excitons may have a much lower phonon scattering rate than free carriers. While electrons and phonons interact relatively strongly in the hybrid perovskites,[161] excitons interact significantly less with phonons because of their dipolar nature. A calculation shows the exciton-LO phonon scattering rate is reduced by a factor of $\gamma = \left(\frac{18a_0^3R_f}{4\epsilon_\infty R_x^4}\right)^2$, where a_0 is the the exciton Bohr radius, $R_e = \sqrt{\frac{\hbar}{2m_e\omega_{LO}}}$, $R_h = \sqrt{\frac{\hbar}{2m_h\omega_{LO}}}$, and $R_x = \sqrt{\frac{\hbar}{2m_x\omega_{LO}}}$ are the electron, hole, and exciton polaron radii, respectively, where m_e, m_h, and m_x are their corresponding effective masses, and ω_{LO} is the LO phonon frequency.[60] Here, γ is estimated to be 5.3×10^{-4} in orthorhombic $MAPbI_3$ and 5.2×10^{-4} in orthorhombic $MAPbBr_3$ (parameters are shown in **Appendix Table B1**).

The higher onset temperature for long L_D in $MAPbBr_3$ is consistent with its larger E_B. Though excitons are charge neutral, they can diffuse and split under the Schottky field at the contacts, leading to photocurrent. Due to the band bending at the contacts, one type

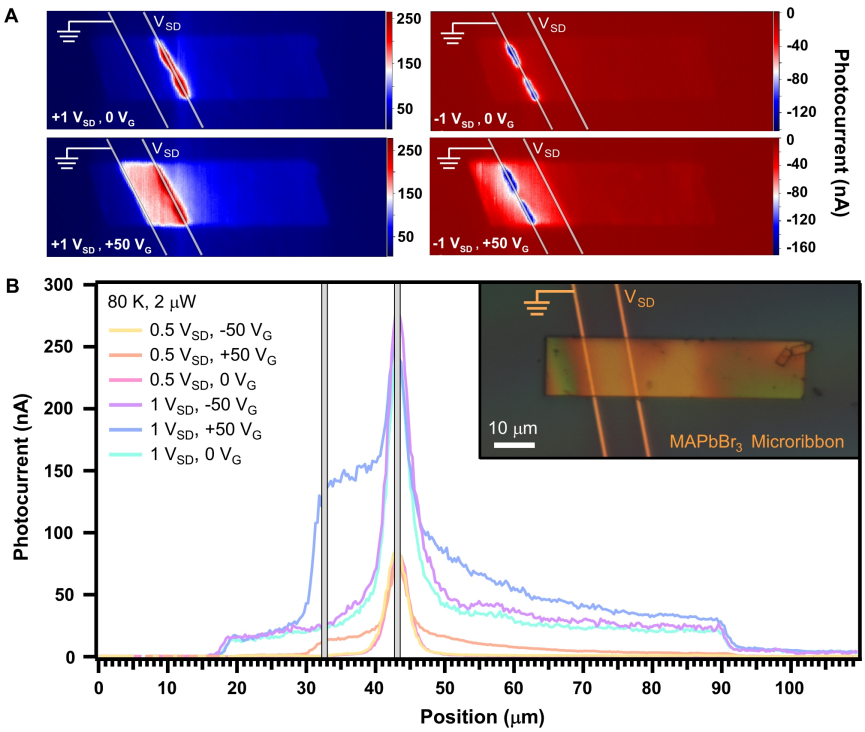

Figure 3.12: Gate dependent photocurrent profiles. (A) Gate dependent photocurrent maps at 80 K and $V_{SD} = 1$ and -1 V, respectively. White lines indicate electrode positions. (B) Bias and gate-dependent SPCM profiles along the long axis at 80 K. Inset, optical image of a $MAPbBr_3$ microplate with bottom-contacts visible through the crystal due to $MAPbBr_3$'s partial transparency.

of carrier (electron in this case) flows into the contact while the other type is blocked. As a result, a photocurrent is produced similar to the charge separation process in a Schottky photovoltaic device, as modeled in previous work. [88] [123] [53]

The photocurrent magnitude of the long-range tail first increases, caused by the increasing exciton fraction (f_{ex}). Then it decreases below 140 K, likely because the lower thermal energy becomes less effective at dissociating excitons even when they enter the depletion region. We calculated f_{ex} from the Saha equation in the field-free region and in the depletion region by considering electric field effects (further detail in Appendix B: $MAPbBr_3$). f_{ex} was significantly decreased under the electric field at the metal junction (estimated to be 5 V/μm) for $MAPbI_3$ but did not change much for $MAPbBr_3$ at 80 K (**Figure 3.10F**).

One significant difference with $MAPbI_3$ is that the $MAPbBr_3$ photocurrent distributions always exhibit a short decay component near the contact. $MAPbBr_3$ is known to have a higher defect density than $MAPbI_3$ [180] and the defect density is expected to be significantly higher at the surface, causing a faster recombination. The short photocurrent decay near the contact may be due to the fast surface recombination. When the laser is far away from the contact, a large fraction of injected carriers recombine quickly at the surface. A smaller fraction of carriers (around 25% at 140 K), generated inside the micro-plate away from surface, form excitons and travel with high mobility to the contact.

3.4.4 Gate Effects on Carrier Diffusion - $MAPbBr_3$

Finally, we briefly discuss the gate modulation on the non-local photocurrent. The application of a gate voltage (V_G) has negligible effect at room temperature, presumably due to ion migration in $MAPbBr_3$ which screens the gate induced electric field. At lower temperatures, however, V_G significantly modulates the conductivity of the $MAPbBr_3$ micro-plate devices. The dark conductance drops by about an order of magnitude under positive V_G, indicating the device is p-type (**Appendix Figure B.8**). The hole mobility extracted from the slope of the gate scan is 2.3×10^{-3} cm^2/Vs. Note that this value is an underestimation of the actual hole mobility because of the large contact resistance. The gate scan also shows a bigger hysteresis at higher temperature, indicating ion migration or charge trapping. The photocurrent distributions are also sensitive to V_G in the $MAPbBr_3$ micro-plate FET (**Figure 3.12**). The photocurrent inside the source-drain channel increases by a factor of 6 when V_G increases to 50 V at $V_{SD} = 1$ V, likely because the p-type channel becomes much more insulating and the voltage drop across the channel increases, leading to a larger photocurrent. At $V_{SD} = 0.5$ V, the non-local photocurrent could be completely turned on/off by the gate (**Figure 3.12B**). This is likely because the weaker junction electric field is insufficient to split excitons in the absence of V_G. The non-local photocurrent outside the channel also

increases at positive V_G. This could be attributed to the longer carrier recombination time as the positive V_G reduces the majority carrier (hole) concentration, though it is still unclear.

In summary, we observed, via photocurrent mapping, gate-tunable exciton diffusion lengths up to 100 μm below 140 K in single-crystal $MAPbBr_3$ micro-plates. The onset temperature for observing this long decay length in $MAPbBr_3$ (140 K) is significantly higher than that in $MAPbI_3$ (80 K), consistent with the larger exciton binding energy in $MAPbBr_3$. Along with a carrier lifetime of 1.2 μs or shorter determined from time-resolved measurements, we estimate a high exciton mobility on the order of 10^4 cm^2/Vs. The high mobility is most likely due to the dipolar nature of the excitons, as they interact with phonons much less than monopolar free carriers. Formation of exciton-polaritons is unlikely to explain the 100 μm photocurrent decay length since our micro-plates are not optically confined in a fabricated photonic cavity. This work offers key insights on fast exciton transport in HOIP systems. It also provides methods for electrical detection and manipulation of exciton transport. The observed long exciton diffusion lengths may motivate unique designs of exciton-based photovoltaic materials and devices.

3.4.5 Where?

This set of experiments was performed at both UC Davis as well as CINT (LANL site). Photocurrent spectroscopy and SPCM measurements were taken in Dr. Yu's laboratory, again with fabrication assistance from CNM2, and XRD characterization by Dr. Taufour's research team. PL spectroscopy and TRPL measurements were taken at CINT, in Dr. Htoon's laboratory. Theoretical work was performed by Dr. Senger at the Izmir Institute of Technology.

3.5 COMSOL Simulations of Exciton Transport

It should be mentioned that the vast quantity of experiments and phonon scattering calculations presented in this chapter are further backed up by quantitative COMSOL simulations of photocurrent decay profiles with and without the influence of excitons (specifically in $MAPbI_3$ in this case), performed by a colleague, Kuen Wai Tang,[53] using my experimental data.[60]

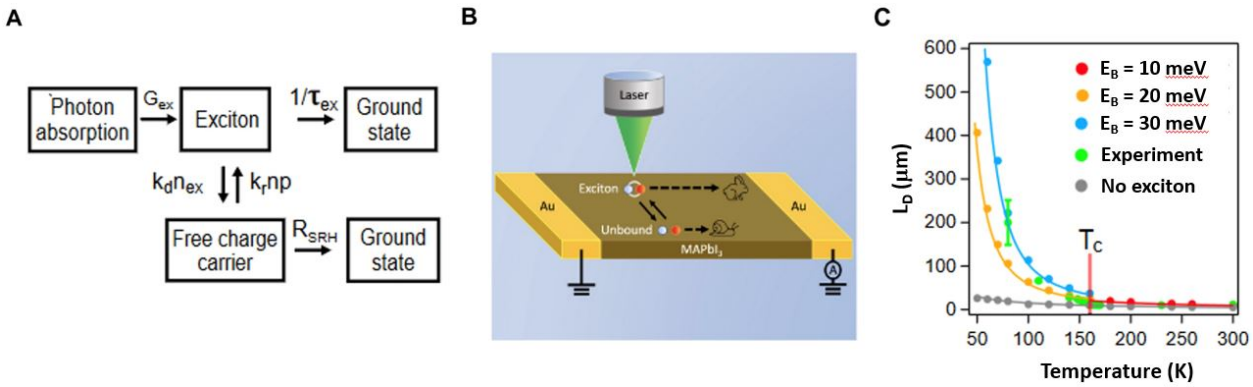

Figure 3.13: (A) Diagram showing the generation, pairing/dissociation, and recombination processes of coexisting excitons and free carriers. (B) Schematic drawing of device configuration under a focused laser and the generation and transport of excitons and free carriers. (C) Simulated temperature dependent L_D at different E_B values or in the absence of excitons. The circles are L_D values extracted from the hyperbolic fitting of Tang's simulated photocurrent distributions, which are not displayed here but can be found in our published work.[53] The solid curves are calculated using **Equation 3.22**. The experimental results (green circles, extracted from reference[60]) are also shown to compare with the simulation.

Inspired by the experimental work, we perform device modeling and numerical simulations to rigorously analyze the exciton formation and transport in $MAPbI_3$ micro-structures under local photoexcitation. The simulation results agree well with our experimental observations including temperature and gate-dependent photocurrent decay lengths. A similar approach[185] has been applied to simulate the excitonic effects in conducting polymer solar cells, but excitons were treated as immobile particles. In this work, we instead consider that excitons are significantly more mobile than free carriers. Another major difference is that the device geometry examined in the previous work was a solar cell under uniform il-

lumination, while we consider a point photoexcitation as used in SPCM. Our results indeed show that excitons can actually dictate and dominate the photocurrent distributions at low temperature.[53]

3.5.1 Basic Equations

We consider three coexisting particles in the material under illumination: free electrons, free holes, and excitons. These particles may be dressed by phonons, thus resulting in reduced mobilities. A free electron and a free hole are bound into an exciton at a rate described by Langevin recombination (k_r), which assumes an exciton is created if an electron and a hole move within a joint capture radius,[184]

$$k_r = \frac{\mu e}{\epsilon_r \epsilon_0} \tag{3.6}$$

where $\mu = \mu_n + \mu_p$ is the sum of electron and hole mobilities and ϵ_r is the dielectric constant. The exciton also undergoes a dissociation into a free electron and a free hole at a rate (k_d) that depends on the local electric field E,

$$k_d(E) = k_r K(E) \tag{3.7}$$

At $E = 0$, the equilibrium constant of exciton dissociation $K(0)$ is given as,[186]

$$K(0) = \frac{3}{4\pi a_{ex}^3} e^{-E_B/k_B T} \tag{3.8}$$

where a_{ex} is the exciton radius and $E_B = \frac{e^2}{4\pi\epsilon_r\epsilon_0 a}$ is the exciton binding energy. In the presence of an external electric field, excitons dissociate at a higher rate given by,[184]

$$K(E)/K(0) = \frac{J_1(2\sqrt{-2b})}{\sqrt{-2b}} \tag{3.9}$$

where J_1 is the Bessel function of order one and $b = \frac{e^3 E}{8\pi\epsilon_r\epsilon_0 k_B^2 T^2}$.

As displayed in **Figure 3.13A**, photogenerated excitons exist in equilibrium with free charge carriers via these formation and dissociation processes. Both excitons and free carriers can recombine to the ground state, as well as drift and diffuse to other locations. To calculate the densities of free electrons (n), free holes (p), and excitons (n_{ex}), one needs to solve the electrostatic and continuity equations,

$$\nabla \cdot \vec{E} = e(p + N_d - n - N_a)/\epsilon_r\epsilon_0 \tag{3.10}$$

$$\frac{dn}{dt} = k_d(E)n_{ex} - k_r np - R_{SRH} - \nabla \cdot \vec{J_n} \tag{3.11}$$

$$\frac{dp}{dt} = k_d(E)n_{ex} - k_r np - R_{SRH} - \nabla \cdot \vec{J_p} \tag{3.12}$$

$$\frac{dn_{ex}}{dt} = G_{ex} + k_r np - k_d(E)n_{ex} - n_{ex}/\tau_{ex} - \nabla \cdot \vec{J_{ex}} \tag{3.13}$$

where N_a is the acceptor concentration, N_d is the donor concentration, G_{ex} is the photoexcitation rate, and τ_{ex} is the lifetime of excitons. G_{ex} in **Equation 3.13** is set to initially generate excitons, however we note that the simulation results do not change if G_{ex} initially generates free carriers, due to the fast pairing and dissociation processes.

We assume that free carriers recombine through the Shockley-Read-Hall process at a rate R_{SRH},

$$R_{SRH} = \frac{np - {n_i}^2}{\tau_p(n + n_i) + \tau_n(p + n_i)} \tag{3.14}$$

$\vec{J_n}$, $\vec{J_p}$, $\vec{J_{ex}}$ are number (not charge) current densities of electrons, holes, and excitons, respectively. Each current density has both diffusion and drift components. Explicitly, we have,

$$\vec{J_n} = -\mu_n n\vec{E} - \mu_n k_B T \nabla n/e \tag{3.15}$$

$$\vec{J_p} = \mu_p p\vec{E} - \mu_p k_B T \nabla p/e \tag{3.16}$$

$$\vec{J_{ex}} = -\mu_{ex} k_B T \nabla n_{ex}/e \tag{3.17}$$

where μ_n, μ_p, μ_{ex} are the mobilities of electrons, holes, and excitons, respectively. We assume the Einstein relation is held in all three cases (for example, $D_{ex} = \mu_{ex} k_B T/e$). The drift term in **Equation 3.17** is set to zero because excitons are charge neutral. We ignore photo-induced thermoelectric current as the observed photocurrent is much larger than that expected from such an effect,[60] confirmed by previous simulation work.[88] [123]

3.5.2 Solving The Simplified Equations

The above equations can only be solved analytically by making some large assumptions. These assumptions are likely over-simplified, but the analytic solutions can help us understand the physical mechanisms. For the purposes of this dissertation, I will summarize the three assumptions that were made - for the full, detailed analysis I recommend reading our published work.[53] The last assumption is most relevant to our experimental work.

Assumption 1 - The material is under homogeneous photoexcitation. If free carriers and excitons are uniformly distributed through the sample, then all net currents within the sample itself are nullified. Additionally, if the pairing time ($\tau_{pair} = \frac{1}{k_r n}$) is much faster than

the recombination time, then n_{ex}/τ_{ex} can also be dropped from **Equation 3.13**. In the absence of electric field, we then have an equilibrium equation,

$$np/n_{ex} = K(0) = \frac{3}{4\pi a_{ex}^3} e^{-E_B/k_B T} \tag{3.18}$$

We note that the above equation is similar in form to the Saha-Langmuir equation[57] [187], with the thermal de Broglie wavelength ($\lambda = h/\sqrt{2\pi m_{ex}^* k_B T}$, where $m_{ex}^* = m_e m_h/(m_e + m_h)$ is the effective mass of an exciton) replaced by the exciton size a_{ex}. Both the Saha-Langmuir equation and **Equation 3.18** have been used to relate the exciton and free carrier densities in equilibrium[57] [188] [184] [185].

Assumption 2 - The excitation source is point-like, but exciton density is negligible when $E_B \ll k_B T$. This means **Equations 3.11** and **3.12** are reduced to the continuity equations for free carriers alone. Photocurrent will decay exponentially as the point excitation moves away from the contact ($I = I_0 e^{-x/L_D}$),[90] where the decay length equals the minority carrier L_D.

Assumption 3 - The most interesting assumption; exciton mobility is enormous ($\mu_n \ll \mu_{ex}$ and $\mu_p \ll \mu_{ex}$). This assumption comes from our high mobility exciton hypothesis, as presented in our previous work.[60] In this extreme case, we ignore the drift and diffusion of free carriers ($J_n = J_p = 0$). Our $MAPbI_3$ samples were n-type, so we have $R_{SRH} = p/\tau_p$ at low photoexcitation intensity. If we consider a steady state (carrier concentration is independent of time), summing **Equations 3.12** and **3.13** yields,

$$\nabla \cdot \vec{J}_{ex} = G_{ex} - n_{ex}/\tau_{ex} - p/\tau_p \tag{3.19}$$

In the region outside the excitation point (away from the laser), $G_{ex} = 0$ and the above equation in one dimension becomes,

$$D_{ex}\frac{d^2n_{ex}}{dx^2} = n_{ex}/\tau_{ex} + p/\tau_p \tag{3.20}$$

We further assume free carriers and excitons reach a dynamic balance at any position, allowing **Equation 3.18** to eliminate p. Additionally, $n \approx N_d$ is expected to be uniform under low photoexcitation in n-type devices, so we have,

$$D_{ex}\frac{d^2n_{ex}}{dx^2} = n_{ex}[1/\tau_{ex} + K(0)/N_d\tau_p] = n_{ex}/\tau_{eff} \tag{3.21}$$

where τ_{eff} is the effective lifetime. The solution to this equation is a simple exponential distribution of exciton concentration, indicating that photocurrent exponentially decays with a decay length that is determined by the exciton diffusion coefficient and a hybrid effective lifetime,

$$L_D = \sqrt{D_{ex}\tau_{eff}} = \sqrt{\frac{D_{ex}}{1/\tau_{ex} + K(0)/N_d\tau_p}} \tag{3.22}$$

With these assumptions, we are able to perform rigorous finite element simulations in COMSOL to model transport of coexisting excitons and free carriers locally excited by a focused laser. The device modeling shows that highly mobile excitons become important and actually dominate the photocurrent decay profiles at low temperature in HOIPs (**Figure 3.13C**). The simulations are highly consistent with the previous experimental results.[60] The main results of the entire work are well-summarized in Tang's published conclusions.[53]

Chapter 4. Self-Trapped Excitons in 1D $C_4N_2H_{14}PbBr_4$

We now move on to a different material to continue our study of excitonic effects in hybrid semiconductors. In the previous chapter, we explored the concept of extremely mobile free excitons in 3D HOIP single crystal micro-structures. Here, we perform an effective 180° flip and switch to a low-dimensional, confined material where excitons are instead highly immobile. Due to a (still heavily discussed) number of factors, these FEs, generated via photoexcitation, immediately undergo a self-trapping process and become highly localized. It has been argued that the presence or absence of the self-trapping process depends largely on the structural and electronic dimensionality of the material.[83] However, a more recent theoretical work has shown that the trapping of FEs is more simply determined by the competition of the energy-gap decrease and deformation-energy increase along with the lattice distortion.[189] We can oversimplify their results as follows - Given some amount of lattice distortion (corresponding to a deformation energy ΔE_{deform}), there is also an associated shift in gap energy (ΔE_{gap}; the Δ here is referring to the energy difference between FE states and STE states at the given amount of lattice distortion). When $\Delta E_{gap} > \Delta E_{deform}$, STE formation is favored, which happens to be the case in many low-dimensional metal halide materials. Thus, low dimensionality is not necessarily a requirement for STE formation, it just tends to provide the right circumstances. Regardless of why they exist, these STEs dominate the emission properties of 1D organic metal halide hybrids and are vital to the creation of the broadband, white light photoluminescence which we hope to apply toward future LED technologies.

4.1 Surface Effects on Anisotropic Photoluminescence in One-Dimensional Organic Metal Halide Hybrids

Here, we perform excitation energy and polarization-dependent PL and time-resolved PL spectroscopy to better understand the optical anisotropy in the 1D single crystal OMHH, N,N'-dimethylethylenediammonium lead bromide ($C_4N_2H_{14}PbBr_4$ or DMEDAPbBr$_4$).[21] We

first confirm that the 1D metal halide chain is along the long axis of single crystal needle-like samples through rigorous X-ray diffraction (XRD) analysis. Then we perform comprehensive PL spectroscopy with the photoexcitation wavelength ranging from 360 nm (3.44 eV) to 410 nm (3.02 eV), in increments of 10 nm, at both room temperature and 8 K. Two linear polarizers are used to independently control and analyze both excitation and emission polarization. Surprisingly, we find that the PL reaches a maximum (minimum) when photoexcitation is linearly polarized perpendicular to the 1D metal halide chain when the excitation wavelength is shorter (longer) than 380 nm (3.26 eV), respectively. The ratio of PL emission under different excitation polarizations (I_{max}/I_{min}, where I_{max} and I_{min} are the maximum and minimum PL emission intensities, respectively) also sensitively depends on the excitation energy and reaches up to 9.4. Time-resolved photoluminescence (TRPL) measurements show an additional linearly polarized fast decay component (< 20 ps) when photoexcitation is parallel to the 1D chain. We carried out first principles calculations that show highly anisotropic optical absorption at low excitation energy. Based on these experimental and theoretical results, we attribute the strong excitation energy dependent anisotropic emission to fast recombination at the surface of 1D OMHHs. This work highlights the importance of surface effects on optical properties of 1D OMHHs.

4.1.1 Characterizing $DMEDAPbBr_4$

The synthetic method of $DMEDAPbBr_4$ can be found in Chapter 2. The crystal structure of $DMEDAPbBr_4$ has already been identified and can be understood by 1D chains surrounded by organic cations to form core-shell-like quantum wires[21] (**Figure 4.1A**). The needle-like single crystals are about a few mm long and 100 μm wide and tall as shown in **Figure 4.1B,C**. The orientation of the 1D metal halide chains relative to the needle axis has not been previously determined. To resolve this, we perform careful XRD analysis on single crystal needles lying on the substrates. The orthorhombic crystal has similar lattice constants along the a and c axes (a = 14.62 Å and c = 14.41 Å), but the lattice constant

along the b axis (the 1D metal halide chain) is much shorter (b = 6.10 Å). The crystal orientation can be identified from the missing XRD peaks, since the diffraction only occurs in the crystal planes parallel to the substrates.

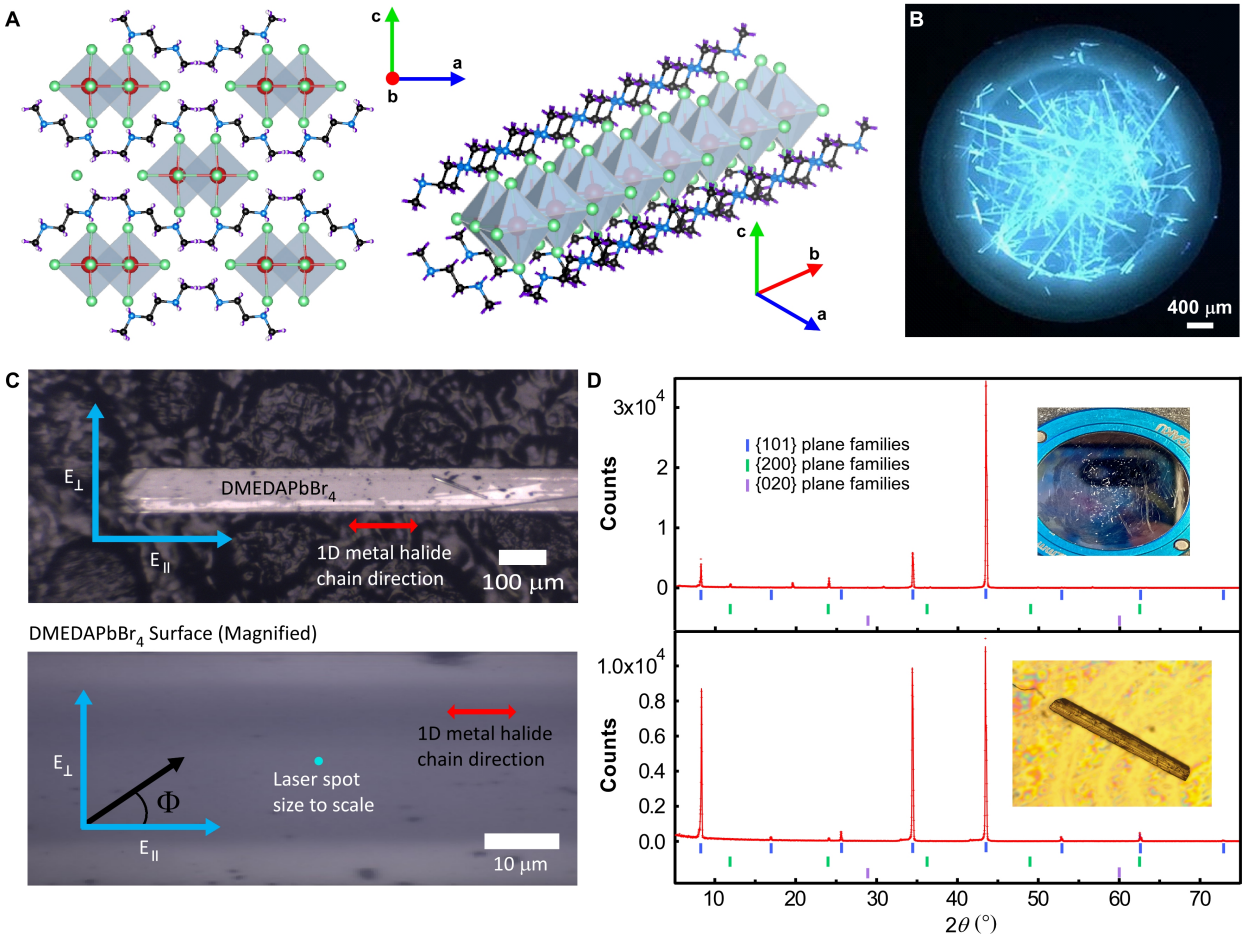

Figure 4.1: (A) Structure of $DMEDAPbBr_4$ that can be described as lead bromide quantum wires wrapped by the organic cations (red spheres: lead atoms; green spheres: bromine atoms; blue spheres: nitrogen atoms; black spheres: carbon atoms; purple spheres: hydrogen atoms; grey polyhedra: $PbBr_6^{4-}$ octahedrons). Hydrogen atoms are hidden for clarity in the image on the right. The red $\vec{b}$ axis indicates the 1D chain direction. (B) Single crystals of $DMEDAPbBr_4$ under UV light (365 nm). (C) A single $DMEDAPbBr_4$ sample on carbon tape with 1D metal halide chain and laser polarization directions labeled. (D) XRD results for many crystals (top) as well as an isolated crystal (bottom).

As shown in **Figure 4.1D, top**, the diffraction pattern from an ensemble of needles exhibits the {101} and {200} plane families, in which the b index is always zero. The {020} plane family is labeled (purple markers) in **Figure 4.1D** to demonstrate the absence of

{020} peaks. The intensities of the {101} peaks are larger, which indicates that the needle cross sections are likely terminated by the {101} planes. This is confirmed by performing the measurement again on a single needle (**Figure 4.1D, bottom**) which shows only the {101} peaks. This clearly indicates that the b axis must be along the long axis of the needle, which is always parallel to the substrate. Otherwise, diffraction peaks with nonzero b index are expected to show up because of the random orientation of the short axis of the needles. We note that there is an additional small peak around 24° that could correspond to the {400} peak. This is likely due to a tiny fragment of crystal that had chipped off and was aligned in a different direction.

4.1.2 Excitation-Sensitive Anisotropic Emission

The experimental setup is shown in **Figure 4.2A**, where a linearly polarized tunable UV laser is focused onto the 1D perovskite crystals with normal incidence and a spot size of about 1 μm. Thanks to the tight laser focus and high optical image resolution, we are able to measure completely clean regions of the crystal surface (**Figure 4.1C, bottom**). The linear polarization of the photoexcitation is tuned by a half waveplate (designed specifically for the UV range). Another linear polarizer for the visible light can be inserted in front of the streak camera to study the polarization of the emitted light. We observe that the overall PL intensity (with the linear polarizer in front of the streak camera removed) sensitively depends on both the polarization of the excitation laser beam as well as the wavelength (**Figure 4.2B**). Under 360 nm excitation, when the electric field of the incident laser beam is perpendicular to the 1D metal halide chains, the emission intensity reaches a maximum, which, for the sample shown in **Figure 4.2B**, is about 5 times stronger than the intensity when the field is parallel.

Surprisingly, this trend reverses itself at lower photoexcitation energy. Under 400 nm (3.10 eV) excitation, the PL emission maximum is reached when the laser polarization is parallel to the 1D chain. This anisotropic emission intensity can be well-fit with the equation

$I(\phi) = I_0 \cos[2(\phi - \phi_0)] + K$, where ϕ is the angle between the photoexcitation polarization and the 1D chain, ϕ_0 is the phase shift, I_0 is the polarization-dependent intensity amplitude, and K is the polarization-independent intensity component[42] (**Figure 4.2B**). ϕ_0 is found to be close to 0 for 400 nm and $\pi/2$ for 360 nm from the fitting. The reversal of polarization dependence of PL upon increasing the photoexcitation energy has not been reported to our knowledge. The 400 nm excitation is close to the minimum absorption energy of $DMEDAPbBr_4$, which corresponds to the exciton resonance energy. We plot the total PL counts under photoexcitation with polarization parallel and perpendicular to the chain at various excitation wavelengths in **Figure 4.2C** and **Appendix Figure C.10** (for a different sample). The PL intensity first increases and then decreases as the excitation wavelength increases from 360 nm to 400 nm. There is also a clear cross-over at 380 - 390 nm (3.18 - 3.26 eV), where the perpendicular polarization generates stronger PL at shorter wavelength.

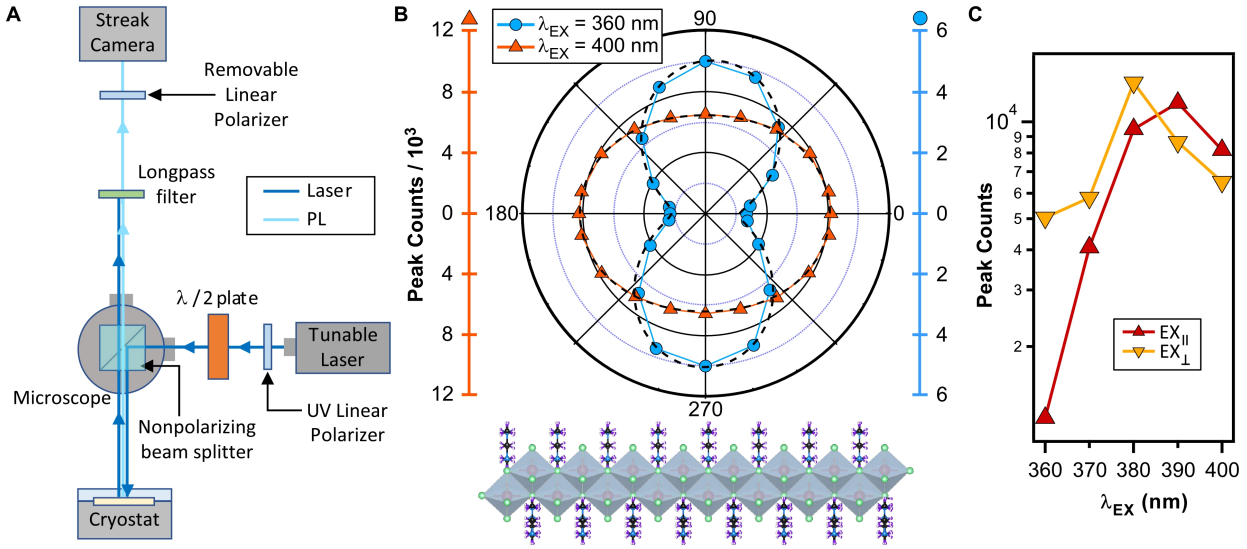

Figure 4.2: (A) Schematic of experimental setup for polarization-dependent PL and TRPL measurements. (B) Polar plot of peak PL counts as a function of excitation angle for high (360 nm) and low (400 nm) energy excitation. The dashed lines are curve fits. Polarization at 0° is parallel to the 1D chain of $DMEDAPbBr_4$. Please note the different scales of the orange and blue axes. (C) Total PL emission counts as a function of excitation wavelength and orthogonal excitation polarizations. All PL counts are normalized to photoexcitation power. (Sample #3)

The PL emission spectra are broad, but their shape is independent of the excitation polarization (**Figure 4.3A**) and excitation wavelength for both 295 K and 8 K. The broadband emission has been attributed to the exciton self-trapping.[21] The total emission is stronger and the spectral width is narrower at low temperature, as is typical for these families of metal halide hybrids due to significant electron-phonon and/or exciton-phonon coupling, which can be understood through the Fröhlich longitudinal optical (LO) phonon broadening model.[21] [161] [190] We define an excitation anisotropy ratio as $R_{EX} = I_{EX\perp}/I_{EX\parallel}$, where $I_{EX\parallel}$ ($I_{EX\perp}$) is the peak PL count (with the detector polarizer removed) when photoexcitation is linearly polarized parallel (perpendicular) to the 1D chain, respectively. R_{EX} increases at lower temperature from 4.3 to 9.3 at $\lambda_{EX} = 360$ nm for Sample #3. Curiously, at low temperature, R_{EX} abruptly increases between 370 nm (3.35 eV) and 390 nm (3.18 eV) excitation. The reason behind this bump in the trend is currently unknown but may be caused by an exciton fine structure revealed at low temperature.[70] [191] [192] [193] [194] [195] R_{EX} varies from sample to sample, up to 9.4 at room temperature for one sample (**Figure 4.3B**). The variation is presumably due to the internal alignment of 1D molecular chains along with the long axis of the sample and defect levels, which can sensitively depend on the growth conditions. As excitation wavelength increases, R_{EX} decreases and then crosses below 1 around 380 nm (**Figure 4.3B**), meaning parallel excitation is creating brighter emission. This trend is repeatable across multiple DMEDAPbBr$_4$ samples, with the cross-over excitation wavelength varying between about 375 and 385 nm (3.31 and 3.22 eV). The anisotropy ratio is also fairly large at long wavelength, up to 1/3.

The PL emission is highly linearly polarized parallel to the 1D chain, regardless of the excitation polarization, as shown in **Figure 4.3C**. We define an emission anisotropy ratio as $R_{EM} = I_{EM\parallel}/I_{EM\perp}$, where $I_{EM\parallel}$ ($I_{EM\perp}$) is the peak PL count when the detector polarizer is parallel (perpendicular) to the 1D chain, respectively. R_{EM} are extracted from **Figure 4.3C** to be 11.4 (11.2) for perpendicular (parallel) excitation at room temperature, corresponding to a degree of polarization ($P = \frac{I_{EM\parallel} - I_{EM\perp}}{I_{EM\parallel} + I_{EM\perp}}$) of 84%. These values are significantly

higher than those reported in 1D polymer and Pt chains,[35] [37] as well as the previously reported values in 1D OMHHs $C_4N_2H_{14}PbI_4$ and $C_3H_{10}NPbI_3$,[42] [43] demonstrating the strong anisotropy and high quality of our samples. The PL peak position shifts from 510 nm (2.43 eV) for the emission parallel to the chain to 485 nm (2.56 eV) for that perpendicular to the chain (**Figure 4.3C**). A similar blue-shift of PL spectra for transverse polarization has been observed in $C_3H_{10}NPbI_3$.[43] This spectral shift indicates the transverse-polarized exciton state has a slightly higher energy than the longitudinally polarized exciton state.[196] Note by contrast that, for absorption, calculations show a blue shift around 1.5 eV for the transverse compared to the longitudinally polarized peaks; we attribute the difference to the self-trapping of the emitting excitons.

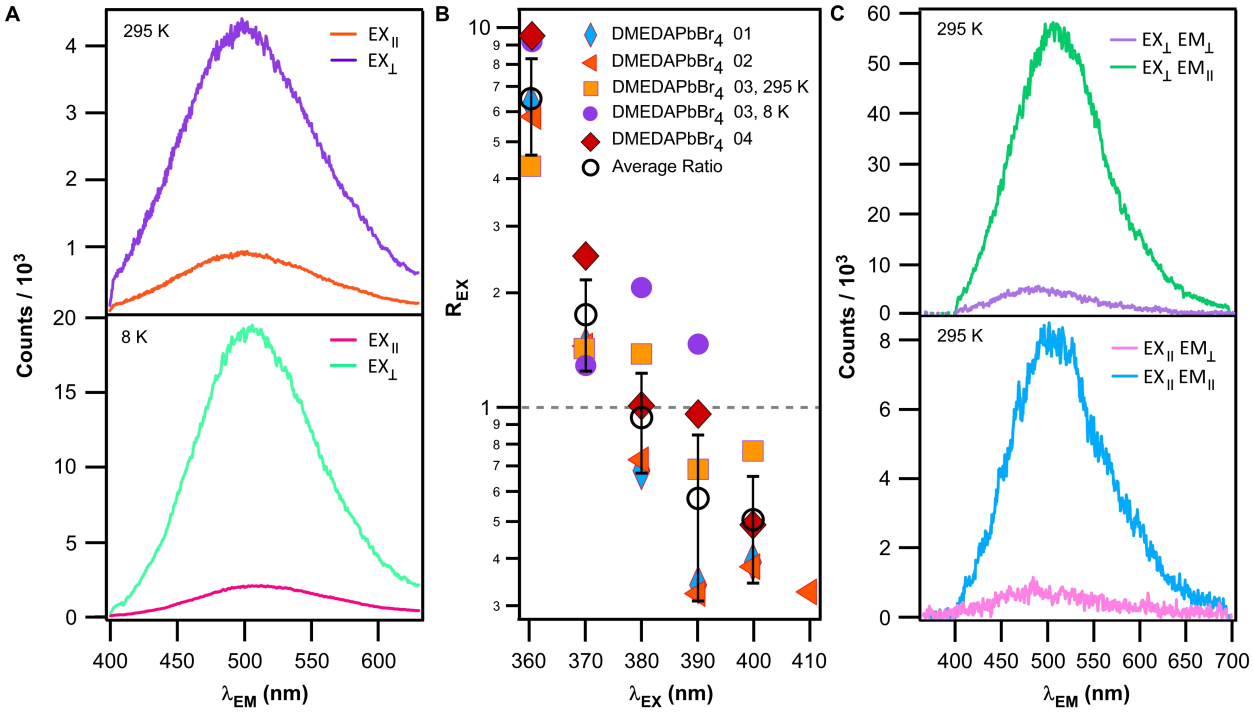

Figure 4.3: (A) Excitation polarization-dependent PL spectra for Sample #3 at room temperature and 8 K, respectively. Counts drop off at 400 nm due to a long pass filter. The measurements were performed with excitation wavelength of 360 nm and no polarizer was in the detection path. (B) $R_{EX} = I_{EX\perp}/I_{EX\parallel}$ for representative $DMEDAPbBr_4$ samples at room temperature and 8 K. Fewer data points are displayed at 410 nm excitation due to the PL becoming too weak for accurate measurements. (C) Room temperature PL emission spectra for Sample #2 at 360 nm with the detector linear polarizer inserted.

4.1.3 TRPL of Self-Trapped Excitons

PL emission under a pump pulse (< 200 fs) at 380 nm shows a slow decay (4 - 7 ns) under excitation perpendicular to the 1D chain, consistent with previous reports.[21] However, an initial sharp decay (12 - 14 ps) is observed when the excitation polarization is parallel to the 1D chain (**Figure 4.4A**). The decay constants are extracted from the exponential fitting (dashed curves in **Figure 4.4A**). We caution that the slow decay constants have large uncertainty because the data is fit in a < 1 ns duration. The presence and magnitude of this sharp decay feature appears to depend on both excitation polarization as well as excitation wavelength. At 360 nm excitation the sharp feature is relatively weaker than at 380 nm excitation under parallel excitation (**Appendix Figure C.11**). Under all excitation wavelengths, $DMEDAPbBr_4$ appears to emit both parallel and perpendicular to the 1D chains, but the parallel component is always significantly stronger. The initial sharp decay peak is only observed when the detector polarizer is parallel to the chain in the sample shown in **Figure 4.4A**, though a small peak is also observed for perpendicular emission polarization in another sample (**Appendix Figure C.12**). The PL emission spectral peak blue-shifts from 530 nm (2.34 eV) to 500 nm (2.48 eV) as the PL intensity increases to maximum in about 40 ps after the pump pulse (**Figure 4.4B**). Then the PL falls to a slow decay state in about 50 ps. The measured fast decay time stays at about 12 - 14 ps (**Appendix Figures C.13** and **C.14**) when the pump intensity increases by 20 times at both 295 K and 11 K, though the measured decay time is likely limited by the temporal resolution of the setup (**Appendix Figure C.15**) and should be considered as the upper bound of the real value. The PL counts for both the short and long components are linear with the fluence of the pump laser (**Appendix Figures C.13** and **C.14**), at both 295 K and 11 K. The slow decay component is around 4 - 7 nanoseconds but could not be accurately determined in our experiment because of the high repetition rate of the excitation laser pulses.

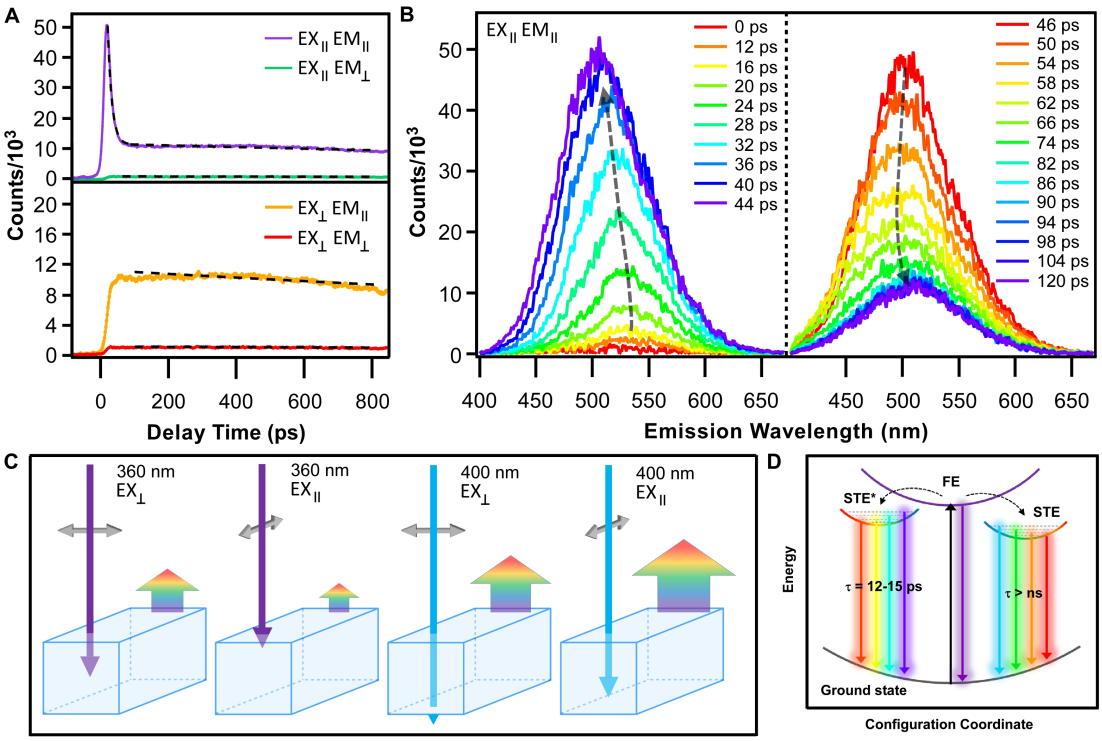

Figure 4.4: (A) PL counts as a function of delay time after 380 nm pulsed excitation at room temperature (Sample #5) with different excitation and emission polarization configurations. (B) PL emission spectra at various delay times across the rise and fall of the sharp feature seen under parallel excitation and emission in (A). (C) Proposed surface effect model. At 360 nm, parallel polarization is absorbed very close to the sample surface, resulting in reduced PL emission. At 400 nm, both polarizations can now penetrate farther into the bulk, but the parallel polarization is more readily absorbed, resulting in relatively stronger emission. (D) Configuration coordinate diagram with relaxation pathways for the proposed TRPL surface effect mechanism. FE = free exciton; STE = self-trapped exciton. STEs* are created near the surface and recombine fast, while STEs are in the bulk and recombine slowly.

4.1.4 Band Structure, Density of States, and Absorption Simulations

We summarize the main observations here: (a) PL emission is stronger when excitation polarization is parallel (perpendicular) to the 1D chains at λ_{EX} = 400 nm (360 nm), respectively. (b) PL emission is always more strongly polarized along the chain, regardless of excitation wavelength or polarization. (c) TRPL shows a fast decay (< 20 ps) only when excitation polarization is parallel to the chain. All of these observations can be understood by the surface effects on PL as detailed below.

The optical absorption of 1D halide perovskites is expected to be highly anisotropic, strongly depending on the optical polarization. This is because the optical electric field parallel to the chain can more easily polarize the electrons along the 1D chain composed of inorganic octahedra. Confined by the insulating organic structure surrounding the chain, electrons are harder to be polarized by a transverse electric field. To confirm, our theorist collaborators (who are much better at math than me) performed plane-wave DFT calculations in the Quantum ESPRESSO code,[197] with the Perdew-Burke-Ernzerhof (PBE)[198] exchange-correlation functional. Relaxation starting from the XRD structure ($a = 14.62$ Å, $b = 6.10$ Å, $c = 14.40$ Å, $\alpha = \beta = \gamma = 90°$) gave lattice parameters in close agreement ($a = 14.70$ Å, $b = 6.06$ Å, $c = 14.56$ Å, $\alpha = \beta = \gamma = 90°$), as seen in work on other hybrid perovskites and OMHHs.[199] [200]. The calculations used a primitive cell of this body-centered tetragonal structure, with lattice parameters $a = b = c = 10.80$ Å, and $\alpha = 32.48°$, $\beta = 94.86°$, $\gamma = 85.88°$ with the Pb-Br chain along the z direction (see more details in Appendix C: $C_4N_2H_{14}PbBr_4$). The calculated electronic band structure of the 1D metal halides in the GW approximation (with a simple spin-orbit correction) is shown in **Figure 4.5A**; the gap is indirect and computed to be 3.6 eV, though the difference between the direct and indirect bandgap is only 16 meV. The valence band maximum (VBM) has contributions mostly from the p-orbitals of Br, whereas at the conduction band minimum (CBM), p-orbitals of Pb dominate (**Figure 4.5C**). The electronic bands are dispersive along the Pb-Br chain direction but are nearly flat along the other two perpendicular directions.

Additionally, the absorption spectrum was calculated through the Bethe-Salpeter Equation (BSE) in the BerkeleyGW code,[201] shown in **Figure 4.5B**. Here, the utilization of BSE in the calculation allows one to take the GW energies and inject the contributions of electron-hole interaction. These contributions are composed of the electrostatic attraction between the electron and hole, and the "exchange" term, which is repulsive. Thus, BSE accounts for excitonic effects in the absorption spectrum, which is necessary to get accurate results when E_B is large in the material. The lowest exciton energy was found at 2.9 eV. Re-

sults from the random phase approximation (RPA) were also provided for comparison, which do not include excitonic effects. By comparing the absorption peaks of BSE and RPA, we found a substantial exciton binding energy (830 meV), as is usual in low-dimensional structures.[202] The first absorption peak is strong along the Pb-Br chain (z-polarized), consistent with the Pb-Br chain mainly contributing to the electronic transition at the band edges. The peak is mainly due to transitions at $\vec{k} = Z$ from the VBM and the next band below the VBM to the CBM and the next band above the CBM (CBM+1). For x- and y-polarizations, the dominant transitions are at $\vec{k} = X$ and Y respectively, and in both cases are from VBM to CBM and CBM+1. **Figure 4.5B** shows large anisotropy in absorption in this material.

4.1.5 Surface Effects on STE Recombination

Though the overall absorption spectrum of a sample containing many randomly oriented needles has been measured,[21] the polarization dependent absorption spectrum of a single needle has not been obtained due to its small size. The above calculation clearly indicates strong anisotropic absorption for the lowest energy excitation, and hence in the excitation energy range used in our experiment (3.02 - 3.44 eV), which was just above the (perhaps slightly underestimated) calculated peak energy (2.9 eV) through BSE, after considering excitonic effects. Note the minimum absorption energy was determined by the excitonic energy instead of the single-particle gap. The calculated optical transition rates are much higher for the parallel electric field in the lowest energy peak shown in **Figure 4.5B**. The corresponding absorption depth reaches as shallow as 10 nm for polarization parallel to the Pb-Br chain, at least two orders of magnitude smaller than that under perpendicular polarization (**Figure 4.5D**). The sharp rise of the peak on the low energy side agrees with the rapid increase in the optical absorption as the excitation energy increases within the experimentally accessible range. Consequently, at $\lambda_{EX} = 400$ nm, the photon energy is just above the minimum absorption energy and the absorption is weak. The photoexcited charge carriers are located relatively deep in the bulk (depicted in **Figure 4.4C**). In this case, the

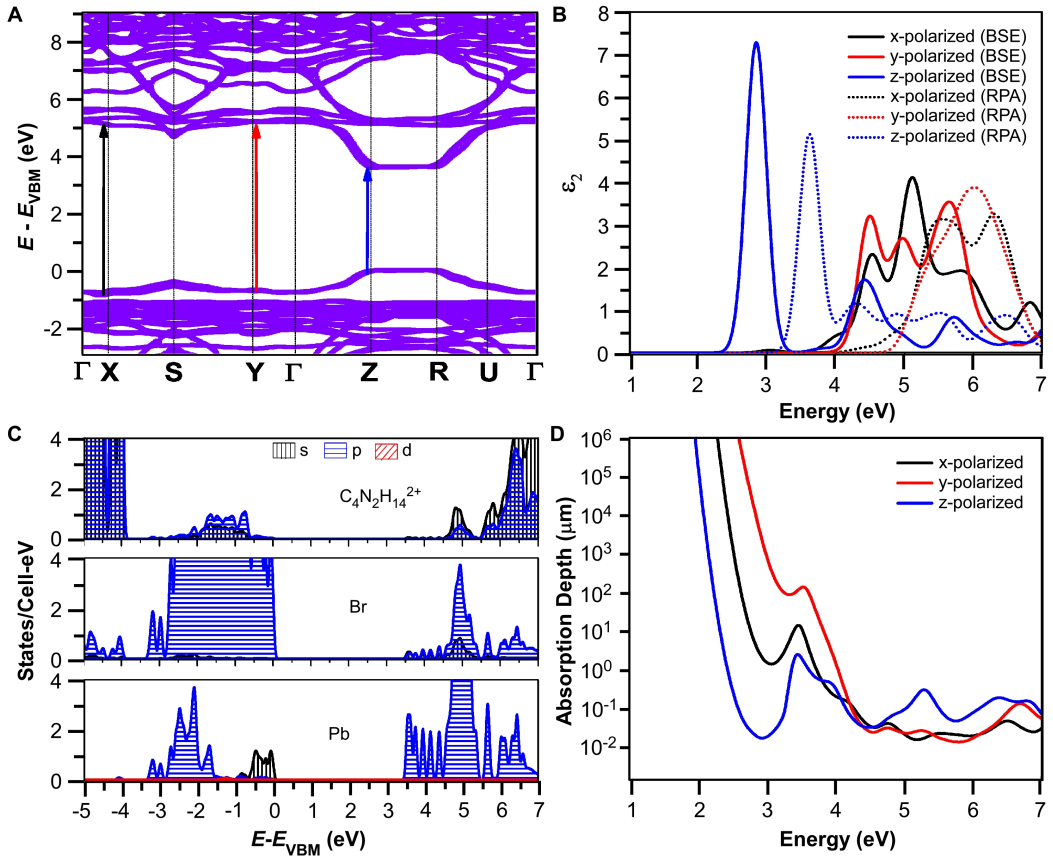

Figure 4.5: Electronic structure simulations. (A) Electronic band structure, in the conventional Brillouin zone, in the GW approximation plus a spin-orbit correction to the gap. Arrows show the dominant transitions for the lowest-energy peaks for light polarized along x (black), y (red), and z (blue) directions, where z is the direction along the Pb-Br chains. (B) Polarized absorption spectra with (BSE, solid) and without (RPA, dashed) electron-hole interactions, based on the GW bandstructure with spin-orbit correction to the gap. (C) Partial density of states from DFT to show atomic orbital character of bands, with gap corrected by GW and spin-orbit coupling. (D) Absorption depth for polarized light, from BSE as in B).

absorption is enhanced when the polarization is parallel to the chain as the perpendicularly polarized light is likely only absorbed partially by the approximately 100 μm thick samples. This leads to a moderately enhanced emission under parallel polarized excitation. In contrast, at $\lambda_{EX} = 360$ nm, the absorption is much stronger due to resonance with the lowest excitonic level and the photoexcited carriers are generated closer to the surface. For parallel polarization, the absorption is even stronger, leading to a very shallow distribution of photoexcited carriers. Under these conditions, the PL intensity is strongly reduced because of fast recombination at the surface. At $\lambda_{EX} = 380$ nm, both perpendicular and parallel

excitations generated about the same PL intensities, when the surface effects under parallel polarization and the incomplete absorption under perpendicular polarization have similar impacts to the PL reduction.

Regardless of excitation polarization or energy, the emission is mostly polarized parallel to the 1D chain, indicating the transition dipoles of self-trapped excitons are preferentially parallel to the 1D chain. However, there is always a perpendicular component of emission as well. This may simply be caused by the non-perfect alignment of the 1D chains, though the sharp XRD peaks indicate the samples are highly crystalline. Another possibility is that a small portion of self-trapped excitons exist with transition dipoles not entirely parallel to the chain. For example, the transition dipole moment has been estimated to make an angle of 65 - 70° with the chain direction in J-aggregates of thiacarbocyanine dyes.[36]

TRPL results can also be understood with the above hypothesis of surface effects. We first highlight the key observations in TRPL measurements in detail below: (i) parallel excitation results in two distinct decay constants with a fast component shorter than 20 ps and a slow component of 4 - 7 ns, while perpendicular excitation only produces the slow component; (ii) the initial sharp PL decay is also highly linearly polarized (**Figure 4.4A**); (iii) both the fast and slow components are linear with the fluence of the pump laser (**Appendix Figures C.13** and **C.14**) at both 295 K and 11 K; (iv) the emission spectra of the fast and slow components has a similar shape, with the fast component slightly blue-shifted. Observation (i) indicates that the initial fast recombination is likely induced by the excitons generated close to the surface under parallel excitation. Observation (ii) implies that the emission from trapped charge at the radiative surface defect states is unlikely to account for the initial fast PL decay, since the emission from surface defects is expected to have random polarization. Observation (iii) indicates that the initial sharp decay is unlikely to be caused by a nonlinear effect such as Auger recombination. Lastly, the similarity in the broad emission spectra in observation (iv) suggests that both the fast and slow components are created by a similar recombination process of STEs. The different decay times and emission

energies are likely caused by the types of STEs generated under different polarizations as depicted in **Figure 4.4D**. Under parallel excitation, a significant portion of STEs are created near the surface (labeled as STE* in **Figure 4.4D**). These STEs* recombine at a faster rate with higher emission energy.

We briefly discuss the possible mechanisms that may account for the different dynamics of STES* near the surface. The slow recombination in 1D metal halides has been attributed to spin-forbidden transitions of STEs,[22] [203] where photoexcited free excitons could rapidly transfer to a triplet state due to strong spin-orbit coupling in the presence of the heavy element Pb in the crystal. The triplet state then slowly relaxes to the ground state. The fast PL component is most likely caused by nonradiative recombination via surface defects, such as dangling bonds or vacancies, through Shockley-Read-Hall (SRH) recombination. This kind of recombination occurs when defects provide mid-gap states that are roughly equidistant from the valence and conduction bands. These states are called recombination centers because they allow for electrons and holes to reach similar (or even same) mid-gap energy levels, where they can then easily recombine without emitting a photon. This provides a fast nonradiative pathway, substantially reducing the overall PL intensity under parallel polarization.

The observed initial fast PL component is still from the radiative STE* recombination, though only a small portion of STE*s recombine radiatively, as most excitons near the surface recombine nonradiatively through the surface defects. The excitons generated in the bulk away from the surface do not suffer from this fast defect-mediated nonradiative recombination, as the interchain diffusion of excitons is expected to be very slow. However, we do not exclude other possible mechanisms expediting the STE* recombination near the surface. The proximity to the surface may help mix the single and triplet states to allow faster recombination. For example, singlet-triplet conversion through intersystem crossing (ISC) has been reported recently [204] [205] [206] and ISC can be induced by crystal structure distortion by stress.[207] Mixing of singlet and triplet excitons has been predicted to occur in 3D halide

perovskites near inhomogeneities as a result of spin-orbit coupling.[208] We speculate that surface reconstruction may have a similar effect. The initial slight blue-shift can also be caused by the difference in emission energy at the surface. The out-of-plane electric field at the sample surface may have an impact on the charge recombination dynamics. The ion migration in 1D OMHHs[209] may create surface charge that results in an electric field near the surface. By comparing PL by one-photon and two-photon excitation, it has been observed that the recombination lifetime is significantly reduced and the emission spectra blue-shift near the surface of $MAPbBr_3$,[210] similar to our observations in **Figure 4.4A,B**. Further work such as magnetic field and electric field-dependent TRPL measurements, as well as passivation of surface defects by coating, are needed to fully clarify the exact mechanism.

In summary, we performed excitation energy and polarization-dependent PL and TRPL spectroscopy to elucidate optical anisotropy properties in the 1D single crystal OMHH, N,N'-dimethylethylenediammonium lead bromide. We confirmed the parallel orientation of the 1D metal halide chain with respect to the long axis of the needle-like crystals. We performed comprehensive polarization-dependent PL and TRPL spectroscopy with the photoexcitation wavelength ranging from 360 nm to 410 nm at both room temperature and 8 K. Interestingly, we found that the trend of anisotropic PL reverses as we increase photoexcitation energy, where perpendicular (parallel) excitation results in more emission at higher (lower) energy, respectively. The anisotropy ratio, defined by $R_{EX} = I_{EX\perp}/I_{EX\parallel}$, increases from 1/3 at 410 nm to 9.4 at 360 nm. Curiously, TRPL measurements reveal an additional fast decay component of < 20 ps only when excitation is parallel to the 1D chains, which could be caused by the surface impacts on the recombination of self-trapped excitons. We emphasize that the fast PL component is linearly polarized and exhibited an emission spectrum similar to the slow component, so it is unlikely to be induced by radiative recombination via surface defects. Instead, we speculate that the fast recombination is caused by nonradiative recombination via surface defects or by the crystal structure distortion near the surface, which mixes the triplet and singlet states of STEs. Finally, we carried out first

principles calculations that displayed highly anisotropic optical absorption in the range of our excitation energies. Based on these experimental and theoretical results, we attribute the strong excitation energy dependent anisotropic emission to a drastically different recombination process at the surface of 1D OMHHs. This work highlights the importance of surface effects in understanding the optical properties of 1D OMHHs and utilizing their anisotropic and broadband emission in novel applications for lighting and photodetection.

4.1.6 Where?

This set of experiments was performed at UC Davis, CINT (LANL site), and CINT (SNL site). Preliminary polarization-dependent PL tests were conducted in Dr. Yu's laboratory, with XRD characterization once more by Dr. Taufour's research team. Polarization-dependent PL and TRPL spectroscopy measurements were taken at CINT (SNL site), in Dr. Luk's laboratory. Further characterization measurements, including polarization-dependent Raman spectroscopy (not displayed here; perhaps in a future publication), were performed at CINT (LANL site). Samples were synthesized by Dr. Ma's group at FSU. Theoretical work was performed by our collaborators at UC Merced and the Molecular Foundry.

Chapter 5. Conclusions and Future Work

5.1 Conclusions

5.1.1 Highly Mobile Excitons in $MAPbI_3$ And $MAPbBr_3$ Micro-Structures

Through the application of several powerful optoelectronic measurement techniques, including scanning photocurrent microscopy, time-resolved photocurrent and photoluminescence, and photocurrent spectroscopy, we garnered new crucial information on the temperature and gate-dependent transport properties of single crystal $MAPbI_3$ and $MAPbBr_3$ micro-structures. In $MAPbI_3$, we observed a room temperature L_D of around 10 μm which abruptly increased to 22 μm across the low temperature tetragonal to orthorhombic phase change. L_D then further increased to roughly 200 μm by 80 K, corresponding to a photocurrent profile that appeared nearly flat. This rapid increase of L_D, combined with the observation of a consistently short carrier lifetime, led to the formation of our super mobile exciton hypothesis, where excitons undergo efficient formation and high speed transport at low temperature (where $E_B > k_BT$). The phonon-scattering rate of excitons should be significantly suppressed as a consequence of their dipolar nature, compared to free carriers and charged polarons. This hypothesis is supported by calculated temperature and carrier concentration-dependent mobilities that are in excellent agreement with the experimental results. Furthermore, the application of a gate voltage allowed for direct tuning of the majority carrier (electron) concentration and opened another pathway to control the low temperature transport. Increasing (decreasing) the electron concentration led to a substantial increase (decrease) in L_D, which can be understood through the exciton model as well, since increasing the electron concentration should enhance exciton formation probability.

In $MAPbBr_3$, we observed similar, but still distinctly unique, temperature-dependent transport behaviors. Here, the room temperature L_D was only a few μm, but an additional, long decay component began to form at temperatures as high as 140 K, again near the phase change region. While $MAPbI_3$ often had to be cooled down to 80 K in order to display

the nearly flat photocurrent profiles (which could always be fit using a single exponential), $MAPbBr_3$ consistently displayed two separate decay components (requiring a double exponential fitting) where the short component was always present and the long component (around 100 μm) could appear at much higher temperatures than $MAPbI_3$. We believe this is directly related to the exciton transport picture. If the long L_D component arises from efficient exciton transport in both materials, then we expect $MAPbBr_3$ to reveal the long component at higher temperatures, as is observed, since E_B is larger in that material. In fact, E_B was large enough in our samples to be directly measured through photocurrent spectroscopy coupled with Elliott model fittings. Along with carrier lifetimes of 1.2 μs or shorter, determined from time-resolved photoluminescence and photocurrent measurements, we estimate an enormous exciton mobility, on the order of 10^4 cm^2/Vs. In our published works, we elaborate in detail on other various phenomena that could explain our observations (exciton-polaritons, photon recycling, etc.), and provide evidence and discussion to rule them out.

These projects led to the creation of a novel hypothesis toward understanding the fascinating low temperature transport behavior of our HOIP micro-structures. Efficient, fast exciton transport in 3D HOIPs is a unique concept that we believe could motivate new designs for exciton-based, or exciton-enhanced, photovoltaic materials and architectures, where excitons are no longer viewed as villains to device performance but instead provide assistance.

5.1.2 Anisotropic Emission of Self-Trapped Excitons in 1D $C_4N_2H_{14}PbBr_4$

In this most recent work, we performed excitation energy and polarization-dependent PL and TRPL spectroscopy to illuminate some interesting (and unexpected) optical anisotropy properties in the 1D single crystal OMHH, $C_4N_2H_{14}PbBr_4$. Thanks to careful XRD analysis performed by our collaborators, we were able to confirm the parallel orientation of the 1D metal halide chains with respect to the macro-scale long axis of the needle-like crystals. We

performed a suite of polarization and temperature-dependent PL and TRPL spectroscopic measurements, with the excitation source ranging from 360 nm to 410 nm. We discovered an initially confusing trend in the anisotropic PL behavior, with respect to excitation wavelength. At relatively lower excitation energy (longer wavelength), parallel excitation (with respect to the chains) generates brighter emission (more counts) than perpendicular excitation. However, this trend appears to depend on excitation energy, and at relatively higher energies the trend actually flips and perpendicular excitation generates brighter emission. In fact, under 360 nm excitation, the anisotropy ratio, defined by $R_{EX} = I_{EX\perp}/I_{EX\parallel}$, increases to almost 10 (meaning 10 times more emission is detected under perpendicular excitation).

Interestingly, TRPL measurements revealed a fast decay component of < 20 ps on top of the well-known, expected slow decay, but only when excitation was parallel to the 1D chains. This fast component is slightly blueshifted, linearly polarized, and immediately broadband, just like the slow component, hinting that it too originates from STE recombination and not random defects. We theorize that the fast decay is indeed tied to STE recombination, but perhaps a different type of STE which is slightly higher in energy and recombines much faster, specifically due to surface-related effects in the material. Such surface effects are not necessarily related to defects or degradation in the surface region, but could instead arise from local crystal structure distortions, ion movement, or other stresses, which mix the triplet and singlet STE states.

Lastly, we carried out first principles calculations that displayed highly anisotropic optical properties, especially absorption, in the range of our excitation energies. The absorption depth in the parallel configuration (excitation parallel to 1D chains) proves to be immensely shallower than the perpendicular configuration, further backing our surface effect model. This project's results reveal how careful one needs to be in controlling and utilizing the optical properties of 1D OMHHs for future light generation and detection, since merely the presence of a surface can alter these properties so dramatically.

5.2 Ongoing and Future Work

5.2.1 T-REx User Projects

One of the major pieces of my fellowship at Los Alamos National Laboratory has consisted of the construction of a time-resolved experimental microscope system, which has been nicknamed the T-REx. The T-REx system represents a flexible platform capable of facilitating a variety of ultrafast microscopy experiments spanning the ultraviolet to near infrared regime. The base configuration allows for non-degenerate differential reflectivity measurements (commonly known as pump-probe) with diffraction-limited spatial and sub-100 femtosecond time resolutions. These experiments can be performed in both co-linear and non-co-linear geometries, the latter being beneficial when freely tunable polarizations of the pump and/or probe beams are necessary. The inclusion of an avalanche photo-detector and associated timing electronics (such as single photon counting modules), in concert with field-of-view restricting apertures, further extends the system to enable time-resolved photoluminescence microscopy where the real-space excitation and emission regions can be independently controlled. Thanks to the Janis ST500 optical cryostat coupled into the T-REx build, all of these experiments can be performed at room or cryogenic temperatures down to 5 K, with the additional capability of applying bias and gate voltages to the samples when electronic properties are of interest.

- Nonlocal Photoluminescence of HOIP Micro-Structures (Ongoing)

Through the T-REx microscope and other available CINT systems (at both the Core and Gateway facilities), we are utilizing our extensive capabilities in ultrafast optical spectroscopy and microscopy to track spatio-temporal dynamics of excitons in HOIP microstructures and identify (with an aim to control) the pathways of exciton formation and dissipation. Our systems can focus down to micron size beam spots while preserving sub-100 fs temporal resolution in a broad spectral range, which makes them perfect for studying

our micro-structure devices under variable temperature conditions. Unlike a previous study of exciton diffusion in HOIPs[211] where oil immersion magnification was necessary to achieve a high enough spatial resolution to extract the PL profile, we anticipate a spatially broad PL signature (10's of μm) in our 3D devices, thus indicating high diffusivity values (a property directly related to L_D). A spatially broad PL signature removes the need for oil immersion magnification, which typically limits experimental temperature range. While steady-state PL studies on single crystal devices have been previously performed, we are using our ultrafast setups to monitor the time-resolved exciton diffusivity dynamics as we drop to cryogenic temperatures, where we expect to see further PL broadening. By pumping the sample in one location and then only collecting emission (from exciton recombination) a known distance away (10 μm or so), we can monitor how long it takes for that emission to arrive and be collected. With the distance and time known, we can get an effective exciton velocity, which we anticipate to be quite large. The ultrafast time resolution allows us to examine the dynamics of the exciton formation, transport, and recombination mechanisms, and apply this knowledge to suppress undesired losses and dissipation of exciton population by adjusting material composition, dimensionality, charge densities (gating), and device geometries.

- Coherent Phonon Control in SnIP Nano-Wires (Ongoing) and Ultrafast Nanoscale Photocurrent Control in Hybrid Nano-Plasmonic-2D Material Systems (Ongoing)

There are several other User projects being currently conducted, including these two, that are making use of the T-REx's capabilities. Unfortunately and fortunately, these projects are likely to become publications and therefore cannot be publicly described in detail just yet.

5.2.2 Spatially Resolved Pump-Probe Photocurrent (Future)

Here, photocurrent, rather than photoluminescence, will be measured as a function of delay time between pump and probe laser pulses. The measured signal can be thought of as the probe-induced photocurrent, but modified by the pump-generated carriers. If the pump-created carriers persist when the probe pulse arrives, a smaller photocurrent will be generated due to the reduced absorption of the probe beam (also known as saturation - carriers cannot be excited if they are already excited). Therefore, a measurable dip in the photocurrent signal is expected with a characteristic time directly related to the carrier lifetime. This measurement method has previously been used to study the carrier lifetime in graphene.[212] [213] We intend to track carrier lifetime in our samples as a function of gate voltage, temperature, and pump intensity to better understand how lifetime is affected by these parameters.

Additionally, we can focus the pump and probe beams at separate spatial locations on the micro-structure devices. Such a configuration can be used to measure an effective transit time of the pump-induced carriers to the probe location, and hence provide information about the velocity of the carrier transport.[214] The dependence of this transit time on the separation distance between the two beam spots can be used to determine the carrier/exciton transport speed. This provides a direct way to measure the exciton diffusivity as a function of temperature as well as gate voltage. Measurements with ps resolution may also capture hot carrier transport, which would assist in understanding the non-equilibrium photo-physics in HOIPs. An intriguingly slow hot carrier cooling, up to 100 ps, has been recently reported in $MAPbBr_3$.[106]

References

[1] Michael M Lee, Joël Teuscher, Tsutomu Miyasaka, Takurou N Murakami, and Henry J Snaith. Efficient hybrid solar cells based on meso-superstructured organometal halide perovskites. *Science*, 338(6107):643–647, 2012.

[2] Nam Joong Jeon, Jun Hong Noh, Woon Seok Yang, Young Chan Kim, Seungchan Ryu, Jangwon Seo, and Sang Il Seok. Compositional engineering of perovskite materials for high-performance solar cells. *Nature*, 517(7535):476, 2015.

[3] Bening Tirta Muhammad, Shaoni Kar, Meera Stephen, and Wei Lin Leong. Halide perovskite-based indoor photovoltaics: recent development and challenges. *Materials Today Energy*, 23:100907, 2022.

[4] Jin-Wook Lee, Shaun Tan, Sang Il Seok, Yang Yang, and Nam-Gyu Park. Rethinking the a cation in halide perovskites. *Science*, 375(6583):eabj1186, 2022.

[5] Guichuan Xing, Nripan Mathews, Swee Sien Lim, Natalia Yantara, Xinfeng Liu, Dharani Sabba, Michael Grätzel, Subodh Mhaisalkar, and Tze Chien Sum. Low-temperature solution-processed wavelength-tunable perovskites for lasing. *Nature materials*, 13(5):476, 2014.

[6] Dandan Zhang, Samuel W Eaton, Yi Yu, Letian Dou, and Peidong Yang. Solution-phase synthesis of cesium lead halide perovskite nanowires. *Journal of the American Chemical Society*, 137(29):9230–9233, 2015.

[7] PS Whitfield, N Herron, WE Guise, K Page, YQ Cheng, I Milas, and MK Crawford. Structures, phase transitions and tricritical behavior of the hybrid perovskite methyl ammonium lead iodide. *Scientific reports*, 6(1):35685, 2016.

[8] Zhengqi Shi and Ahalapitiya H Jayatissa. Perovskites-based solar cells: A review of recent progress, materials and processing methods. *Materials*, 11(5):729, 2018.

[9] Samuel D Stranks and Henry J Snaith. Metal-halide perovskites for photovoltaic and light-emitting devices. *Nature nanotechnology*, 10(5):391, 2015.

[10] Dong Shi, Valerio Adinolfi, Riccardo Comin, Mingjian Yuan, Erkki Alarousu, Andrei Buin, Yin Chen, Sjoerd Hoogland, Alexander Rothenberger, Khabiboulakh Katsiev, et al. Low trap-state density and long carrier diffusion in organolead trihalide perovskite single crystals. *Science*, 347(6221):519–522, 2015.

[11] Samuel D Stranks, Giles E Eperon, Giulia Grancini, Christopher Menelaou, Marcelo JP Alcocer, Tomas Leijtens, Laura M Herz, Annamaria Petrozza, and Henry J Snaith. Electron-hole diffusion lengths exceeding 1 micrometer in an organometal trihalide perovskite absorber. *Science*, 342(6156):341–344, 2013.

[12] Qingfeng Dong, Yanjun Fang, Yuchuan Shao, Padhraic Mulligan, Jie Qiu, Lei Cao, and Jinsong Huang. Electron-hole diffusion lengths¿ 175 μm in solution-grown ch3nh3pbi3 single crystals. *Science*, 347(6225):967–970, 2015.

[13] Yevgeny Rakita, Sidney R Cohen, Nir Klein Kedem, Gary Hodes, and David Cahen. Mechanical properties of apbx 3 (a= cs or ch 3 nh 3; x= i or br) perovskite single crystals. *MRS Commun.*, 5(4):623–629, 2015.

[14] Michael Sendner, Pabitra K Nayak, David A Egger, Sebastian Beck, Christian Müller, Bernd Epding, Wolfgang Kowalsky, Leeor Kronik, Henry J Snaith, Annemarie Pucci, et al. Optical phonons in methylammonium lead halide perovskites and implications for charge transport. *Mater. Horiz.*, 3(6):613–620, 2016.

[15] Kiyoshi Miyata, Timothy L Atallah, and X-Y Zhu. Lead halide perovskites: Crystal-liquid duality, phonon glass electron crystals, and large polaron formation. *Sci. Adv.*, 3(10):e1701469, 2017.

[16] Jozef T Devreese and Alexandre S Alexandrov. Fröhlich polaron and bipolaron: recent developments. *Rep. Prog. Phys.*, 72(6):066501, 2009.

[17] Omer Yaffe, Yinsheng Guo, Liang Z Tan, David A Egger, Trevor Hull, Constantinos C Stoumpos, Fan Zheng, Tony F Heinz, Leeor Kronik, Mercouri G Kanatzidis, et al. Local polar fluctuations in lead halide perovskite crystals. *Phys. Rev. Lett.*, 118(13):136001, 2017.

[18] Fan Zheng, Liang Z Tan, Shi Liu, and Andrew M Rappe. Rashba spin–orbit coupling enhanced carrier lifetime in ch3nh3pbi3. *Nano Lett.*, 15(12):7794–7800, 2015.

[19] Yongbo Yuan and Jinsong Huang. Ion migration in organometal trihalide perovskite and its impact on photovoltaic efficiency and stability. *Acc. Chem. Res.*, 49(2):286–293, 2016.

[20] Yevgeny Rakita, Omri Bar-Elli, Elena Meirzadeh, Hadar Kaslasi, Yagel Peleg, Gary Hodes, Igor Lubomirsky, Dan Oron, David Ehre, and David Cahen. Tetragonal ch3nh3pbi3 is ferroelectric. *Proc. Natl. Acad. Sci.*, 114(28):E5504–E5512, 2017.

[21] Zhao Yuan, Chenkun Zhou, Yu Tian, Yu Shu, Joshua Messier, Jamie C Wang, Lambertus J Van De Burgt, Konstantinos Kountouriotis, Yan Xin, Ethan Holt, et al. One-dimensional organic lead halide perovskites with efficient bluish white-light emission. *Nature communications*, 8(1):1–7, 2017.

[22] RT Williams and KS Song. The self-trapped exciton. *J. Phys. Chem. Solids*, 51(7):679–716, 1990.

[23] Hsin-Ping Wang, Siyuan Li, Xinya Liu, Zhifeng Shi, Xiaosheng Fang, and Jr-Hau He. Low-dimensional metal halide perovskite photodetectors. *Advanced Materials*, 33(7):2003309, 2021.

[24] Fatemeh Barati, Trevor B Arp, Shanshan Su, Roger K Lake, Vivek Aji, Rienk van Grondelle, Mark S Rudner, Justin CW Song, and Nathaniel M Gabor. Vibronic exciton–phonon states in stack-engineered van der waals heterojunction photodiodes. *Nano Letters*, 2022.

[25] Ioannis Paradisanos, Gang Wang, Evgeny M Alexeev, Alisson R Cadore, Xavier Marie, Andrea C Ferrari, Mikhail M Glazov, and Bernhard Urbaszek. Efficient phonon cascades in wse2 monolayers. *Nature communications*, 12(1):1–7, 2021.

[26] Alexander Vokhmintsev, Ilya Weinstein, and Dmitry Zamyatin. Electron-phonon interactions in subband excited photoluminescence of hexagonal boron nitride. *Journal of Luminescence*, 208:363–370, 2019.

[27] B Berzina, L Trinkler, V Korsak, R Krutohvostov, DL Carroll, KB Ucer, and RT Williams. Exciton luminescence of boron nitride nanotubes and nano-arches. *physica status solidi (b)*, 243(14):3840–3845, 2006.

[28] Zhen Li, Yan Yan, Mu-Sen Song, Jia-Yu Xin, Hai-Yu Wang, Hai Wang, and Yu Wang. Exciton–phonon coupling of chiral one-dimensional lead-free hybrid metal halides at room temperature. *The Journal of Physical Chemistry Letters*, 13:4073–4081, 2022.

[29] Md Zahidur Rahaman, Shuaipeng Ge, Chun-Ho Lin, Yimin Cui, and Tom Wu. One-dimensional molecular metal halide materials: Structures, properties, and applications. *Small Structures*, 2(4):2000062, 2021.

[30] Chenkun Zhou, Haoran Lin, Qingquan He, Liangjin Xu, Michael Worku, Maya Chaaban, Sujin Lee, Xiaoqin Shi, Mao-Hua Du, and Biwu Ma. Low dimensional metal halide perovskites and hybrids. *Materials Science and Engineering: R: Reports*, 137:38–65, 2019.

[31] Emma R Dohner, Adam Jaffe, Liam R Bradshaw, and Hemamala I Karunadasa. Intrinsic white-light emission from layered hybrid perovskites. *Journal of the American Chemical Society*, 136(38):13154–13157, 2014.

[32] Te Hu, Matthew D Smith, Emma R Dohner, Meng-Ju Sher, Xiaoxi Wu, M Tuan Trinh, Alan Fisher, Jeff Corbett, X-Y Zhu, Hemamala I Karunadasa, et al. Mechanism for broadband white-light emission from two-dimensional (110) hybrid perovskites. *The journal of physical chemistry letters*, 7(12):2258–2263, 2016.

[33] Machteld E Kamminga, Hong-Hua Fang, Marina R Filip, Feliciano Giustino, Jacob Baas, Graeme R Blake, Maria Antonietta Loi, and Thomas TM Palstra. Confinement

effects in low-dimensional lead iodide perovskite hybrids. *Chemistry of Materials*, 28(13):4554–4562, 2016.

[34] Yingqi Wang, Songhao Guo, Hui Luo, Chenkun Zhou, Haoran Lin, Xuedan Ma, Qingyang Hu, Mao-hua Du, Biwu Ma, Wenge Yang, et al. Reaching 90% photoluminescence quantum yield in one-dimensional metal halide c4n2h14pbbr4 by pressure-suppressed nonradiative loss. *Journal of the American Chemical Society*, 142(37):16001–16006, 2020.

[35] GR Hayes, IDW Samuel, and RT Phillips. Polarization dependence of the ultrafast photoluminescence of oriented poly (p-phenylenevinylene). *Physical Review B*, 56(7):3838, 1997.

[36] IG Scheblykin, MA Drobizhev, OP Varnavsky, Mark Van der Auweraer, and AG Vitukhnovsky. Reorientation of transition dipoles during exciton relaxation in j-aggregates probed by flourescence anisotropy. *Chemical physics letters*, 261(1-2):181–190, 1996.

[37] Y Wada, U Lemmer, EO Göbel, M Yamashita, and K Toriumi. Time-resolved luminescence study of self-trapped-exciton relaxation in quasi-one-dimensional halogen-bridged mixed-valence metal complexes. *Physical Review B*, 52(11):8276, 1995.

[38] Yann Battie, Damien Jamon, J-S Lauret, A En Naciri, Laurent Broch, and Annick Loiseau. Optical anisotropy of single walled carbon nanotubes investigated by spectroscopic ellipsometry. *Carbon*, 50(12):4673–4679, 2012.

[39] Jiangbin Wu, Xin Cong, Shanyuan Niu, Fanxin Liu, Huan Zhao, Zhonghao Du, Jayakanth Ravichandran, Ping-Heng Tan, and Han Wang. Linear dichroism conversion in quasi-1d perovskite chalcogenide. *Advanced Materials*, 31(33):1902118, 2019.

[40] A Ishii and T Miyasaka. Direct detection of circular polarized light in helical 1d perovskite-based photodiode. *Science advances*, 6(46):eabd3274, 2020.

[41] Xingxing Jiang, Zhengwei Xu, Yueshao Zheng, Jiang Zeng, Ke-Qiu Chen, and Yexin Feng. A first-principles study of exciton self-trapping and electric polarization in one-dimensional organic lead halide perovskites. *Physical Chemistry Chemical Physics*, 24(28):17323–17328, 2022.

[42] Xue Cheng, Jiaqi Ma, Yunxi Zhou, Chen Fang, Jun Wang, Junze Li, Xinglin Wen, and Dehui Li. Optical anisotropy of one-dimensional perovskite c4n2h14pbi4 crystals. *Journal of Physics: Photonics*, 2(1):014008, 2020.

[43] Yiping Du, Zhengguang Yan, Jiawen Xiao, Guoqing Zhang, Yang Ma, Songyu Li, Yonghong Li, Quan Zhou, Lin Ma, and Xiaodong Han. Temperature-dependent luminescence and anisotropic optical properties of centimeter-sized one-dimensional per-

ovskite trimethylammonium lead iodide single crystals. *The Journal of Physical Chemistry Letters*, 13:5451–5460, 2022.

[44] James P Wolfe. Thermodynamics of excitons in semiconductors. *Phys. Today*, 35(3):46–54, 1982.

[45] Beer Pal Singh. Lecture notes on excitons, Chaudhary Charan Singh University, April 2020.

[46] Yumeng You, Xiao-Xiao Zhang, Timothy C Berkelbach, Mark S Hybertsen, David R Reichman, and Tony F Heinz. Observation of biexcitons in monolayer wse 2. *Nat. Phys.*, 11(6):477–481, 2015.

[47] Nikolay S Makarov, Shaojun Guo, Oleksandr Isaienko, Wenyong Liu, István Robel, and Victor I Klimov. Spectral and dynamical properties of single excitons, biexcitons, and trions in cesium–lead-halide perovskite quantum dots. *Nano Lett.*, 16(4):2349–2362, 2016.

[48] Amanda J Neukirch, Wanyi Nie, Jean-Christophe Blancon, Kannatassen Appavoo, Hsinhan Tsai, Matthew Y Sfeir, Claudine Katan, Laurent Pedesseau, Jacky Even, Jared J Crochet, et al. Polaron stabilization by cooperative lattice distortion and cation rotations in hybrid perovskite materials. *Nano Lett.*, 16(6):3809–3816, 2016.

[49] Rui Su, Carole Diederichs, Jun Wang, Timothy CH Liew, Jiaxin Zhao, Sheng Liu, Weigao Xu, Zhanghai Chen, and Qihua Xiong. Room-temperature polariton lasing in all-inorganic perovskite nanoplatelets. *Nano Lett.*, 17(6):3982–3988, 2017.

[50] Michael Stern, Vladimir Umansky, and Israel Bar-Joseph. Exciton liquid in coupled quantum wells. *Science*, 343(6166):55–57, 2014.

[51] Alexander A High, Jason R Leonard, Aaron T Hammack, Michael M Fogler, Leonid V Butov, Alexey V Kavokin, Kenneth L Campman, and Arthur C Gossard. Spontaneous coherence in a cold exciton gas. *Nature*, 483(7391):584–588, 2012.

[52] Yasen Hou, Rui Wang, Rui Xiao, Luke McClintock, Henry Clark Travaglini, John Paulus Francia, Harry Fetsch, Onur Erten, Sergey Y Savrasov, Baigeng Wang, et al. Millimetre-long transport of photogenerated carriers in topological insulators. *Nat. Commun.*, 10(1):1–7, 2019.

[53] Kuen Wai Tang, Senlei Li, Spencer Weeden, Ziyi Song, Luke McClintock, Rui Xiao, R Tugrul Senger, and Dong Yu. Transport modeling of locally photogenerated excitons in halide perovskites. *J. Phys. Chem. Lett.*, 12(16):3951–3959, 2021.

[54] Tracey M Clarke and James R Durrant. Charge photogeneration in organic solar cells. *Chem. Rev.*, 110(11):6736–6767, 2010.

[55] Luke M McClintock, Long Yuan, Ziyi Song, Michael T Pettes, Dmitry Yarotski, Rijan Karkee, David A Strubbe, Liang Z Tan, Azza Ben-Akacha, Biwu Ma, Yunshu Shi, Valentin Taufour, and Dong Yu. Surface effects on anisotropic photoluminescence in one-dimensional organic metal halide hybrids. *Small Structures*, (2200378), 2023.

[56] MA Tamor and JP Wolfe. Drift and diffusion of free excitons in si. *Phys. Rev. Lett.*, 44(25):1703, 1980.

[57] Valerio D'innocenzo, Giulia Grancini, Marcelo JP Alcocer, Ajay Ram Srimath Kandada, Samuel D Stranks, Michael M Lee, Guglielmo Lanzani, Henry J Snaith, and Annamaria Petrozza. Excitons versus free charges in organo-lead tri-halide perovskites. *Nat. Commun.*, 5:3586, 2014.

[58] Atsuhiko Miyata, Anatolie Mitioglu, Paulina Plochocka, Oliver Portugall, Jacob Tse-Wei Wang, Samuel D Stranks, Henry J Snaith, and Robin J Nicholas. Direct measurement of the exciton binding energy and effective masses for charge carriers in organic-inorganic tri-halide perovskites. *Nat. Phys.*, 11(7):582–587, 2015.

[59] Jacky Even, Laurent Pedesseau, and Claudine Katan. Analysis of multivalley and multibandgap absorption and enhancement of free carriers related to exciton screening in hybrid perovskites. *J. Phys. Chem. C*, 118(22):11566–11572, 2014.

[60] Luke McClintock, Rui Xiao, Yasen Hou, Clinton Gibson, Henry Clark Travaglini, David Abramovitch, Liang Z Tan, Ramazan Tugrul Senger, Yongping Fu, Song Jin, et al. Temperature and gate dependence of carrier diffusion in single crystal methylammonium lead iodide perovskite microstructures. *J. Phys. Chem. Lett.*, 11(3):1000–1006, 2020.

[61] Nikolaos Droseros, Demetra Tsokkou, and Natalie Banerji. Photophysics of methylammonium lead tribromide perovskite: Free carriers, excitons, and sub-bandgap states. *Adv. Energy Mater.*, 10(13):1903258, 2020.

[62] Luke McClintock, Ziyi Song, H Clark Travaglini, R Tugrul Senger, Vigneshwaran Chandrasekaran, Han Htoon, Dmitry Yarotski, and Dong Yu. Highly mobile excitons in single crystal methylammonium lead tribromide perovskite microribbons. *The Journal of Physical Chemistry Letters*, 13(16):3698–3705, 2022.

[63] Shan Chen and Gaoquan Shi. Two-dimensional materials for halide perovskite-based optoelectronic devices. *Advanced Materials*, 29(24):1605448, 2017.

[64] Rebecca L Milot, Rebecca J Sutton, Giles E Eperon, Amir Abbas Haghighirad, Josue Martinez Hardigree, Laura Miranda, Henry J Snaith, Michael B Johnston, and Laura M Herz. Charge-carrier dynamics in 2d hybrid metal–halide perovskites. *Nano letters*, 16(11):7001–7007, 2016.

[65] Constantinos C Stoumpos, Chan Myae Myae Soe, Hsinhan Tsai, Wanyi Nie, Jean-Christophe Blancon, Duyen H Cao, Fangze Liu, Boubacar Traoré, Claudine Katan, Jacky Even, et al. High members of the 2d ruddlesden-popper halide perovskites: synthesis, optical properties, and solar cells of (ch3 (ch2) 3nh3) 2 (ch3nh3) 4pb5i16. *Chem*, 2(3):427–440, 2017.

[66] Mingjian Yuan, Li Na Quan, Riccardo Comin, Grant Walters, Randy Sabatini, Oleksandr Voznyy, Sjoerd Hoogland, Yongbiao Zhao, Eric M Beauregard, Pongsakorn Kanjanaboos, et al. Perovskite energy funnels for efficient light-emitting diodes. *Nature nanotechnology*, 11(10):872, 2016.

[67] Giulia Grancini, C Roldán-Carmona, Iwan Zimmermann, E Mosconi, X Lee, D Martineau, S Narbey, Frédéric Oswald, F De Angelis, Michael Graetzel, et al. One-year stable perovskite solar cells by 2d/3d interface engineering. *Nature communications*, 8:15684, 2017.

[68] J-C Blancon, Andreas V Stier, Hsinhan Tsai, Wanyi Nie, CC Stoumpos, Boubacar Traore, L Pedesseau, Mikael Kepenekian, Fumiya Katsutani, GT Noe, et al. Scaling law for excitons in 2d perovskite quantum wells. *Nature communications*, 9(1):2254, 2018.

[69] Yaxin Zhai, Sangita Baniya, Chuang Zhang, Junwen Li, Paul Haney, Chuan-Xiang Sheng, Eitan Ehrenfreund, and Zeev Valy Vardeny. Giant rashba splitting in 2d organic-inorganic halide perovskites measured by transient spectroscopies. *Science advances*, 3(7):e1700704, 2017.

[70] Peter C Sercel, John L Lyons, Darshana Wickramaratne, Roman Vaxenburg, Noam Bernstein, and Alexander L Efros. Exciton fine structure in perovskite nanocrystals. *Nano letters*, 19(6):4068–4077, 2019.

[71] Haoran Lin, Chenkun Zhou, Yu Tian, Theo Siegrist, and Biwu Ma. Low-dimensional organometal halide perovskites. *ACS Energy Letters*, 3(1):54–62, 2017.

[72] Siqi Sun, Min Lu, Xupeng Gao, Zhifeng Shi, Xue Bai, William W Yu, and Yu Zhang. 0d perovskites: Unique properties, synthesis, and their applications. *Advanced Science*, 8(24):2102689, 2021.

[73] Matthew D Smith and Hemamala I Karunadasa. White-light emission from layered halide perovskites. *Accounts of chemical research*, 51(3):619–627, 2018.

[74] Chenkun Zhou, Yu Tian, Oussama Khabou, Michael Worku, Yan Zhou, Joseph Hurley, Haoran Lin, and Biwu Ma. Manganese-doped one-dimensional organic lead bromide perovskites with bright white emissions. *ACS applied materials & interfaces*, 9(46):40446–40451, 2017.

[75] Chenkun Zhou, Haoran Lin, Yu Tian, Zhao Yuan, Ronald Clark, Banghao Chen, Lambertus J van de Burgt, Jamie C Wang, Yan Zhou, Kenneth Hanson, et al. Luminescent zero-dimensional organic metal halide hybrids with near-unity quantum efficiency, chem, 2018.

[76] Reinhard Scholz, Andrei Yu Kobitski, Dietrich RT Zahn, and Michael Schreiber. Investigation of molecular dimers in α-ptcda by ab initio methods: Binding energies, gas-to-crystal shift, and self-trapped excitons. *Physical Review B*, 72(24):245208, 2005.

[77] Dietrich Menzel. Valence and core excitations in rare gas mono-and multilayers: Production, decay, and desorption of neutrals and ions. *Applied Physics A*, 51:163–171, 1990.

[78] RT Williams, KS Song, WL Faust, and CH Leung. Off-center self-trapped excitons and creation of lattice defects in alkali halide crystals. *Physical Review B*, 33(10):7232, 1986.

[79] Shunran Li, Jiajun Luo, Jing Liu, and Jiang Tang. Self-trapped excitons in all-inorganic halide perovskites: fundamentals, status, and potential applications. *The journal of physical chemistry letters*, 10(8):1999–2007, 2019.

[80] Yupeng Zhang, Jingying Liu, Ziyu Wang, Yunzhou Xue, Qingdong Ou, Lakshminarayana Polavarapu, Jialu Zheng, Xiang Qi, and Qiaoliang Bao. Synthesis, properties, and optical applications of low-dimensional perovskites. *Chemical communications*, 52(94):13637–13655, 2016.

[81] Luis M Pazos-Outón, Monika Szumilo, Robin Lamboll, Johannes M Richter, Micaela Crespo-Quesada, Mojtaba Abdi-Jalebi, Harry J Beeson, Milan Vrućinić, Mejd Alsari, Henry J Snaith, et al. Photon recycling in lead iodide perovskite solar cells. *Science*, 351(6280):1430–1433, 2016.

[82] Shanqin Liu, Long Hu, Shujuan Huang, Wanqing Zhang, Jingjing Ma, Jichao Wang, Xinwei Guan, Chun-Ho Lin, Jiyun Kim, Tao Wan, et al. Enhancing the efficiency and stability of pbs quantum dot solar cells through engineering an ultrathin nio nanocrystalline interlayer. *ACS Applied Materials & Interfaces*, 12(41):46239–46246, 2020.

[83] Xiaoming Wang, Weiwei Meng, Weiqiang Liao, Jianbo Wang, Ren-Gen Xiong, and Yanfa Yan. Atomistic mechanism of broadband emission in metal halide perovskites. *The Journal of Physical Chemistry Letters*, 10(3):501–506, 2019.

[84] Yongping Fu, Fei Meng, Matthew B Rowley, Blaise J Thompson, Melinda J Shearer, Dewei Ma, Robert J Hamers, John C Wright, and Song Jin. Solution growth of single crystal methylammonium lead halide perovskite nanostructures for optoelectronic and photovoltaic applications. *J. Am. Chem. Soc.*, 137(17):5810–5818, 2015.

[85] Jian Qing, Hrisheekesh-Thachoth Chandran, Hong-Tao Xue, Zhi-Qiang Guan, Tai-Li Liu, Sai-Wing Tsang, Ming-Fai Lo, and Chun-Sing Lee. Simple fabrication of perovskite solar cells using lead acetate as lead source at low temperature. *Organic Electronics*, 27:12–17, 2015.

[86] Wei Zhang, Michael Saliba, David T Moore, Sandeep K Pathak, Maximilian T Hörantner, Thomas Stergiopoulos, Samuel D Stranks, Giles E Eperon, Jack A Alexander-Webber, Antonio Abate, et al. Ultrasmooth organic–inorganic perovskite thin-film formation and crystallization for efficient planar heterojunction solar cells. *Nature communications*, 6(1):6142, 2015.

[87] Amalie Dualeh, Nicolas Tétreault, Thomas Moehl, Peng Gao, Mohammad Khaja Nazeeruddin, and Michael Grätzel. Effect of annealing temperature on film morphology of organic–inorganic hybrid pervoskite solid-state solar cells. *Advanced Functional Materials*, 24(21):3250–3258, 2014.

[88] Deyi Fu, Jijun Zou, Kevin Wang, Rong Zhang, Dong Yu, and Junqiao Wu. Electrothermal dynamics of semiconductor nanowires under local carrier modulation. *Nano Lett.*, 11(9):3809–3815, 2011.

[89] Rion Graham, Chris Miller, Mark Triplett, and Dong Yu. Scanning photocurrent microscopy in single nanowire devices. In *Nanoepitaxy: Materials and Devices III*, volume 8106, pages 59–66. SPIE, 2011.

[90] Rion Graham and Dong Yu. Scanning photocurrent microscopy in semiconductor nanostructures. *Mod. Phys. Lett. B*, 27(25):1330018, 2013.

[91] Kannan Balasubramanian, Yuwei Fan, Marko Burghard, Klaus Kern, Marcel Friedrich, Uli Wannek, and Alf Mews. Photoelectronic transport imaging of individual semiconducting carbon nanotubes. *Applied Physics Letters*, 84(13):2400–2402, 2004.

[92] Y Gu, E-S Kwak, JL Lensch, JE Allen, Teri W Odom, and Lincoln J Lauhon. Near-field scanning photocurrent microscopy of a nanowire photodetector. *Applied Physics Letters*, 87(4):043111, 2005.

[93] Jiří Marek. Light-beam-induced current characterization of grain boundaries. *Journal of applied physics*, 55(2):318–326, 1984.

[94] Jonathan E Allen, Eric R Hemesath, and Lincoln J Lauhon. Scanning photocurrent microscopy analysis of si nanowire field-effect transistors fabricated by surface etching of the channel. *Nano letters*, 9(5):1903–1908, 2009.

[95] Yi Gu, John P Romankiewicz, John K David, Jessica L Lensch, and Lincoln J Lauhon. Quantitative measurement of the electron and hole mobility- lifetime products in semiconductor nanowires. *Nano Lett.*, 6(5):948–952, 2006.

[96] Jerome K Hyun and Lincoln J Lauhon. Spatially resolved plasmonically enhanced photocurrent from au nanoparticles on a si nanowire. *Nano letters*, 11(7):2731–2734, 2011.

[97] Michael D Kelzenberg, Daniel B Turner-Evans, Brendan M Kayes, Michael A Filler, Morgan C Putnam, Nathan S Lewis, and Harry A Atwater. Photovoltaic measurements in single-nanowire silicon solar cells. *Nano letters*, 8(2):710–714, 2008.

[98] Marko Burghard and Alf Mews. High-resolution photocurrent mapping of carbon nanostructures. *ACS nano*, 6(7):5752–5756, 2012.

[99] Maria Barkelid, Gary A Steele, and Val Zwiller. Probing optical transitions in individual carbon nanotubes using polarized photocurrent spectroscopy. *Nano letters*, 12(11):5649–5653, 2012.

[100] YH Ahn, AW Tsen, Bio Kim, Yung Woo Park, and Jiwoong Park. Photocurrent imaging of p- n junctions in ambipolar carbon nanotube transistors. *Nano letters*, 7(11):3320–3323, 2007.

[101] Eduardo JH Lee, Kannan Balasubramanian, Ralf Thomas Weitz, Marko Burghard, and Klaus Kern. Contact and edge effects in graphene devices. *Nature nanotechnology*, 3(8):486–490, 2008.

[102] Jiwoong Park, YH Ahn, and Carlos Ruiz-Vargas. Imaging of photocurrent generation and collection in single-layer graphene. *Nano letters*, 9(5):1742–1746, 2009.

[103] Xiaodong Xu, Nathaniel M Gabor, Jonathan S Alden, Arend M Van Der Zande, and Paul L McEuen. Photo-thermoelectric effect at a graphene interface junction. *Nano letters*, 10(2):562–566, 2010.

[104] Gareth Melin. *Spatial Dependence of Photocurrent & Photogeneration Mechanisms in Graphene Field Effect Transistors*. PhD thesis, Concordia University, 2019.

[105] A Jesche, M Fix, A Kreyssig, W R Meier, and P C Canfield. X-Ray diffraction on large single crystals using a powder diffractometer. *Philosophical Magazine*, 96(20):2115–2124, 2016.

[106] Haiming Zhu, Kiyoshi Miyata, Yongping Fu, Jue Wang, Prakriti P Joshi, Daniel Niesner, Kristopher W Williams, Song Jin, and X-Y Zhu. Screening in crystalline liquids protects energetic carriers in hybrid perovskites. *Science*, 353(6306):1409–1413, 2016.

[107] Martin Ledinsky, Tereza Schonfeldova, Jakub Holovsky, Erkan Aydin, Zdenka Hajkova, Lucie Landová, Neda Neyková, Antonín Fejfar, and Stefaan De Wolf. Temperature dependence of the urbach energy in lead iodide perovskites. *The journal of physical chemistry letters*, 10(6):1368–1373, 2019.

[108] Tyson Lanigan-Atkins, Xing He, MJ Krogstad, DM Pajerowski, DL Abernathy, Guangyong NMN Xu, Zhijun Xu, D-Y Chung, MG Kanatzidis, Stephan Rosenkranz, et al. Two-dimensional overdamped fluctuations of the soft perovskite lattice in cspbbr3. *Nature materials*, 20(7):977–983, 2021.

[109] Christian Gehrmann, Sebastián Caicedo-Dávila, Xiangzhou Zhu, and David A Egger. Transversal halide motion intensifies band-to-band transitions in halide perovskites. *Advanced Science*, 9(16):2200706, 2022.

[110] Claudine Katan, Aditya D Mohite, and Jacky Even. Entropy in halide perovskites. *Nature materials*, 17(5):377–379, 2018.

[111] Hui Zhang and Nam-Gyu Park. Polaron in perovskite solar cells: its effect on photovoltaic performance and stability. *Journal of Physics: Energy*, 2023.

[112] Arman Mahboubi Soufiani, Fuzhi Huang, Peter Reece, Rui Sheng, Anita Ho-Baillie, and Martin A Green. Polaronic exciton binding energy in iodide and bromide organic-inorganic lead halide perovskites. *Appl. Phys. Lett.*, 107(23):231902, 2015.

[113] Erika Penzo, Anna Loiudice, Edward S Barnard, Nicholas J Borys, Matthew J Jurow, Monica Lorenzon, Igor Rajzbaum, Edward K Wong, Yi Liu, Adam M Schwartzberg, et al. Long-range exciton diffusion in two-dimensional assemblies of cesium lead bromide perovskite nanocrystals. *ACS Nano*, 14(6):6999–7007, 2020.

[114] Shibin Deng, Enzheng Shi, Long Yuan, Linrui Jin, Letian Dou, and Libai Huang. Long-range exciton transport and slow annihilation in two-dimensional hybrid perovskites. *Nat. Commun.*, 11(1):664, 2020.

[115] David Giovanni, Marcello Righetto, Qiannan Zhang, Jia Wei Melvin Lim, Sankaran Ramesh, and Tze Chien Sum. Origins of the long-range exciton diffusion in perovskite nanocrystal films: photon recycling vs exciton hopping. *Light Sci. Appl.*, 10(1):31, 2021.

[116] Ibrahim Dursun and Burak Guzelturk. Exciton diffusion exceeding 1 μm: run, exciton, run! *Light, Science & Applications*, 10, 2021.

[117] Xuelu Hu, Xiao Wang, Peng Fan, Yunyun Li, Xuehong Zhang, Qingbo Liu, Weihao Zheng, Gengzhao Xu, Xiaoxia Wang, Xiaoli Zhu, et al. Visualizing carrier transport in metal halide perovskite nanoplates via electric field modulated photoluminescence imaging. *Nano Lett.*, 18(5):3024–3031, 2018.

[118] Rui Xiao, Yasen Hou, Yongping Fu, Xingyue Peng, Qi Wang, Eliovardo Gonzalez, Song Jin, and Dong Yu. Photocurrent mapping in single-crystal methylammonium lead iodide perovskite nanostructures. *Nano Lett.*, 16(12):7710–7717, 2016.

[119] Octavi E Semonin, Giselle A Elbaz, Daniel B Straus, Trevor D Hull, Daniel W Paley, Arend M Van der Zande, James C Hone, Ioannis Kymissis, Cherie R Kagan, Xavier Roy, et al. Limits of carrier diffusion in n-type and p-type ch3nh3pbi3 perovskite single crystals. *J. Phys. Chem. Lett.*, 7(17):3510–3518, 2016.

[120] Shuhao Liu, Lili Wang, Wei-Chun Lin, Sukrit Sucharitakul, Clemens Burda, and Xuan PA Gao. Imaging the long transport lengths of photo-generated carriers in oriented perovskite films. *Nano Lett.*, 16(12):7925–7929, 2016.

[121] Xi Wang, Yichuan Ling, Yu-Che Chiu, Yijun Du, Jorge Luis Barreda, Fernando Perez-Orive, Biwu Ma, Peng Xiong, and Hanwei Gao. Dynamic electronic junctions in organic–inorganic hybrid perovskites. *Nano Lett.*, 17(8):4831–4839, 2017.

[122] Henry J Snaith and Peter Hacke. Enabling reliability assessments of pre-commercial perovskite photovoltaics with lessons learned from industrial standards. *Nature Energy*, 3(6):459–465, 2018.

[123] Rui Xiao, Yasen Hou, Matt Law, and Dong Yu. On the use of photocurrent imaging to determine carrier diffusion lengths in nanostructured thin-film field-effect transistors. *J. Phys. Chem. C*, 122(32):18356–18364, 2018.

[124] Christoph Gutsche, Raphael Niepelt, Martin Gnauck, Andrey Lysov, Werner Prost, Carsten Ronning, and Franz-Josef Tegude. Direct determination of minority carrier diffusion lengths at axial gaas nanowire p–n junctions. *Nano letters*, 12(3):1453–1458, 2012.

[125] AD Mohite, DE Perea, S Singh, SA Dayeh, IH Campbell, ST Picraux, and H Htoon. Highly efficient charge separation and collection across in situ doped axial vls-grown si nanowire p–n junctions. *Nano letters*, 12(4):1965–1971, 2012.

[126] Afsoon Soudi, Cheng-Han Hsu, and Yi Gu. Diameter-dependent surface photovoltage and surface state density in single semiconductor nanowires. *Nano letters*, 12(10):5111–5116, 2012.

[127] Yiming Yang, Jiao Li, Hengkui Wu, Eunsoon Oh, and Dong Yu. Controlled ambipolar doping and gate voltage dependent carrier diffusion length in lead sulfide nanowires. *Nano Lett.*, 12(11):5890–5896, 2012.

[128] Dehui Li, Gongming Wang, Hung-Chieh Cheng, Chih-Yen Chen, Hao Wu, Yuan Liu, Yu Huang, and Xiangfeng Duan. Size-dependent phase transition in methylammonium lead iodide perovskite microplate crystals. *Nat. Commun.*, 7:11330, 2016.

[129] M Ibrahim Dar, Gwénolé Jacopin, Simone Meloni, Alessandro Mattoni, Neha Arora, Ariadni Boziki, Shaik Mohammed Zakeeruddin, Ursula Rothlisberger, and Michael Grätzel. Origin of unusual bandgap shift and dual emission in organic-inorganic lead halide perovskites. *Sci. Adv.*, 2(10):e1601156, 2016.

[130] Hong-Hua Fang, Raissa Raissa, Mustapha Abdu-Aguye, Sampson Adjokatse, Graeme R Blake, Jacky Even, and Maria Antonietta Loi. Photophysics of organic–inorganic hybrid lead iodide perovskite single crystals. *Adv. Funct. Mater.*, 25(16):2378–2385, 2015.

[131] Rebecca L Milot, Giles E Eperon, Henry J Snaith, Michael B Johnston, and Laura M Herz. Temperature-dependent charge-carrier dynamics in ch3nh3pbi3 perovskite thin films. *Adv. Funct. Mater.*, 25(39):6218–6227, 2015.

[132] Kewei Wu, Ashok Bera, Chun Ma, Yuanmin Du, Yang Yang, Liang Li, and Tom Wu. Temperature-dependent excitonic photoluminescence of hybrid organometal halide perovskite films. *Phys. Chem. Chem. Phys.*, 16(41):22476–22481, 2014.

[133] Alexander Dobrovolsky, Aboma Merdasa, Eva L Unger, Arkady Yartsev, and Ivan G Scheblykin. Defect-induced local variation of crystal phase transition temperature in metal-halide perovskites. *Nat. Commun.*, 8(1):34, 2017.

[134] Jarvist Moore Frost. Calculating polaron mobility in halide perovskites. *Phys. Rev. B*, 96(19):195202, 2017.

[135] Melike Karakus, Søren A Jensen, Francesco D'Angelo, Dmitry Turchinovich, Mischa Bonn, and Enrique Canovas. Phonon–electron scattering limits free charge mobility in methylammonium lead iodide perovskites. *J. Phys. Chem. Lett.*, 6(24):4991–4996, 2015.

[136] Tom J Savenije, Carlito S Ponseca Jr, Lucas Kunneman, Mohamed Abdellah, Kaibo Zheng, Yuxi Tian, Qiushi Zhu, Sophie E Canton, Ivan G Scheblykin, Tonu Pullerits, et al. Thermally activated exciton dissociation and recombination control the carrier dynamics in organometal halide perovskite. *J. Phys. Chem. Lett.*, 5(13):2189–2194, 2014.

[137] Hee Taek Yi, Xiaoxi Wu, Xiaoyang Zhu, and Vitaly Podzorov. Intrinsic charge transport across phase transitions in hybrid organo-inorganic perovskites. *Adv. Mater.*, 28(30):6509–6514, 2016.

[138] A. Filippetti, A. Mattoni, C. Caddeo, M. I. Saba, and P. Delugas. Low electron-polar optical phonon scattering as a fundamental aspect of carrier mobility in methylammonium lead halide CH3nh3pbi3 perovskites. *Phys. Chem. Chem. Phys.*, 18(22):15352–15362, June 2016.

[139] Matthew Z. Mayers, Liang Z. Tan, David A. Egger, Andrew M. Rappe, and David R. Reichman. How lattice and charge fluctuations control carrier dynamics in halide perovskites. *Nano Lett.*, 18(12):8041–8046, 2018. PMID: 30387614.

[140] Alessandro Stroppa, Domenico Di Sante, Paolo Barone, Menno Bokdam, Georg Kresse, Cesare Franchini, Myung-Hwan Whangbo, and Silvia Picozzi. Tunable ferroelectric

polarization and its interplay with spin–orbit coupling in tin iodide perovskites. *Nature communications*, 5:5900, 2014.

[141] Mikaël Kepenekian, Roberto Robles, Claudine Katan, Daniel Sapori, Laurent Pedesseau, and Jacky Even. Rashba and dresselhaus effects in hybrid organic–inorganic perovskites: from basics to devices. *ACS nano*, 9(12):11557–11567, 2015.

[142] Yongping Fu, Haiming Zhu, Jie Chen, Matthew P Hautzinger, X-Y Zhu, and Song Jin. Metal halide perovskite nanostructures for optoelectronic applications and the study of physical properties. *Nat. Rev. Mater.*, page 1, 2019.

[143] Xin Yu Chin, Daniele Cortecchia, Jun Yin, Annalisa Bruno, and Cesare Soci. Lead iodide perovskite light-emitting field-effect transistor. *Nat. Commun.*, 6:7383, 2015.

[144] Masoumeh Keshavarz, Martin Ottesen, Steffen Wiedmann, Michael Wharmby, Robert Küchler, Haifeng Yuan, Elke Debroye, Julian A Steele, Johan Martens, Nigel E Hussey, et al. Tracking structural phase transitions in lead-halide perovskites by means of thermal expansion. *Adv. Mater.*, 31(24):1900521, 2019.

[145] Haiming Zhu, Yongping Fu, Fei Meng, Xiaoxi Wu, Zizhou Gong, Qi Ding, Martin V Gustafsson, M Tuan Trinh, Song Jin, and XY Zhu. Lead halide perovskite nanowire lasers with low lasing thresholds and high quality factors. *Nat. Mater.*, 14(6):636–642, 2015.

[146] Haiming Zhu, M Tuan Trinh, Jue Wang, Yongping Fu, Prakriti P Joshi, Kiyoshi Miyata, Song Jin, and X-Y Zhu. Organic cations might not be essential to the remarkable properties of band edge carriers in lead halide perovskites. *Adv. Mater.*, 29(1):1603072, 2017.

[147] Chan La-o vorakiat, Huanxin Xia, Jeannette Kadro, Teddy Salim, Daming Zhao, Towfiq Ahmed, Yeng Ming Lam, Jian-Xin Zhu, Rudolph A Marcus, Maria-Elisabeth Michel-Beyerle, et al. Phonon mode transformation across the orthohombic–tetragonal phase transition in a lead iodide perovskite ch3nh3pbi3: a terahertz time-domain spectroscopy approach. *J. Phys. Chem. Lett.*, 7(1):1–6, 2015.

[148] Shreetu Shrestha, Gebhard J Matt, Andres Osvet, Daniel Niesner, Rainer Hock, and Christoph J Brabec. Assessing temperature dependence of drift mobility in methylammonium lead iodide perovskite single crystals. *J. Phys. Chem. C*, 122(11):5935–5939, 2018.

[149] Yin Chen, HT Yi, X Wu, R Haroldson, YN Gartstein, YI Rodionov, KS Tikhonov, A Zakhidov, X-Y Zhu, and Vitaly Podzorov. Extended carrier lifetimes and diffusion in hybrid perovskites revealed by hall effect and photoconductivity measurements. *Nat. Commun.*, 7:12253, 2016.

[150] Constantinos C Stoumpos, Christos D Malliakas, and Mercouri G Kanatzidis. Semiconducting tin and lead iodide perovskites with organic cations: phase transitions, high mobilities, and near-infrared photoluminescent properties. *Inorg. Chem.*, 52(15):9019–9038, 2013.

[151] Hikaru Oga, Akinori Saeki, Yuhei Ogomi, Shuzi Hayase, and Shu Seki. Improved understanding of the electronic and energetic landscapes of perovskite solar cells: high local charge carrier mobility, reduced recombination, and extremely shallow traps. *JACS*, 136(39):13818–13825, 2014.

[152] Jun Xing, Xin Feng Liu, Qing Zhang, Son Tung Ha, Yan Wen Yuan, Chao Shen, Tze Chien Sum, and Qihua Xiong. Vapor phase synthesis of organometal halide perovskite nanowires for tunable room-temperature nanolasers. *Nano Lett.*, 15(7):4571–4577, 2015.

[153] Yajie Jiang, Arman Mahboubi Soufiani, Angus Gentle, Fuzhi Huang, Anita Ho-Baillie, and Martin A Green. Temperature dependent optical properties of ch3nh3pbi3 perovskite by spectroscopic ellipsometry. *Appl. Phys. Lett.*, 108(6):061905, 2016.

[154] Rui Su, Jun Wang, Jiaxin Zhao, Jun Xing, Weijie Zhao, Carole Diederichs, Timothy CH Liew, and Qihua Xiong. Room temperature long-range coherent exciton polariton condensate flow in lead halide perovskites. *Sci. Adv.*, 4(10):eaau0244, 2018.

[155] Christopher L Davies, Marina R Filip, Jay B Patel, Timothy W Crothers, Carla Verdi, Adam D Wright, Rebecca L Milot, Feliciano Giustino, Michael B Johnston, and Laura M Herz. Bimolecular recombination in methylammonium lead triiodide perovskite is an inverse absorption process. *Nat. Commun.*, 9(1):293, 2018.

[156] J. Pollmann and H. Büttner. Effective hamiltonians and binding energies of wannier excitons in polar semiconductors. *Phys. Rev. B*, 16:4480–4490, Nov 1977.

[157] R. T. Senger and K. K. Bajaj. Optical properties of confined polaronic excitons in spherical ionic quantum dots. *Phys. Rev. B*, 68:045313, Jul 2003.

[158] Wayne A. Bowers. The classical polarizability of the hydrogen atom. *Am. J. Phys.*, 54(4):347–350, April 1986.

[159] Laura M. Herz. How lattice dynamics moderate the electronic properties of metal-halide perovskites. *J. Phys. Chem. Lett.*, 9(23):6853–6863, 2018.

[160] Jarvist M Frost, Keith T Butler, Federico Brivio, Christopher H Hendon, Mark Van Schilfgaarde, and Aron Walsh. Atomistic origins of high-performance in hybrid halide perovskite solar cells. *Nano Lett.*, 14(5):2584–2590, 2014.

[161] Adam D Wright, Carla Verdi, Rebecca L Milot, Giles E Eperon, Miguel A Pérez-Osorio, Henry J Snaith, Feliciano Giustino, Michael B Johnston, and Laura M Herz.

Electron–phonon coupling in hybrid lead halide perovskites. *Nat. Commun.*, 7:11755, 2016.

[162] Tyler Otto, Chris Miller, Jason Tolentino, Yao Liu, Matt Law, and Dong Yu. Gate-dependent carrier diffusion length in lead selenide quantum dot field-effect transistors. *Nano Lett.*, 13(8):3463–3469, 2013.

[163] Duyen H Cao, Constantinos C Stoumpos, Omar K Farha, Joseph T Hupp, and Mercouri G Kanatzidis. 2d homologous perovskites as light-absorbing materials for solar cell applications. *J. Am. Chem. Soc.*, 137(24):7843–7850, 2015.

[164] Andreas Gärtner, Alexander W Holleitner, JP Kotthaus, and Dieter Schuh. Drift mobility of long-living excitons in coupled gaas quantum wells. *Appl. Phys. Lett.*, 89(5):052108, 2006.

[165] Shahab Ahmad, Pawan K Kanaujia, Harry J Beeson, Antonio Abate, Felix Deschler, Dan Credgington, Ullrich Steiner, G Vijaya Prakash, and Jeremy J Baumberg. Strong photocurrent from two-dimensional excitons in solution-processed stacked perovskite semiconductor sheets. *ACS Appl. Mater. Interfaces*, 7(45):25227–25236, 2015.

[166] Ya Yi, Changming Wu, Hongchao Liu, Jiali Zeng, Hongtao He, and Jiannong Wang. A study of lateral schottky contacts in wse 2 and mos 2 field effect transistors using scanning photocurrent microscopy. *Nanoscale*, 7(38):15711–15718, 2015.

[167] Peng Chen, Timothy L Atallah, Zhaoyang Lin, Peiqi Wang, Sung-Joon Lee, Junqing Xu, Zhihong Huang, Xidong Duan, Yuan Ping, Yu Huang, et al. Approaching the intrinsic exciton physics limit in two-dimensional semiconductor diodes. *Nature*, 599(7885):404–410, 2021.

[168] Jenya Tilchin, Dmitry N Dirin, Georgy I Maikov, Aldona Sashchiuk, Maksym V Kovalenko, and Efrat Lifshitz. Hydrogen-like wannier–mott excitons in single crystal of methylammonium lead bromide perovskite. *ACS Nano*, 10(6):6363–6371, 2016.

[169] T Thu Ha Do, A Granados del Águila, Chao Cui, Jun Xing, Zhijun Ning, and Qihua Xiong. Optical study on intrinsic exciton states in high-quality ch 3 nh 3 pbbr 3 single crystals. *Phys. Rev. B*, 96(7):075308, 2017.

[170] Le Quang Phuong, Yumi Nakaike, Atsushi Wakamiya, and Yoshihiko Kanemitsu. Free excitons and exciton–phonon coupling in ch3nh3pbi3 single crystals revealed by photocurrent and photoluminescence measurements at low temperatures. *J. Phys. Chem. Lett.*, 7(23):4905–4910, 2016.

[171] Fabian Ruf, Meltem F Aygüler, Nadja Giesbrecht, Bettina Rendenbach, Alice Magin, Pablo Docampo, Heinz Kalt, and Michael Hetterich. Temperature-dependent studies of exciton binding energy and phase-transition suppression in (cs, fa, ma) pb (i, br) 3 perovskites. *APL Mater.*, 7(3):031113, 2019.

[172] Michele Saba, Francesco Quochi, Andrea Mura, and Giovanni Bongiovanni. Excited state properties of hybrid perovskites. *Acc. Chem. Res.*, 49(1):166–173, 2016.

[173] Xihan Chen, Haipeng Lu, Ye Yang, and Matthew C Beard. Excitonic effects in methylammonium lead halide perovskites. *J. Phys. Chem. Lett.*, 9(10):2595–2603, 2018.

[174] Bo Wu, Huy Tiep Nguyen, Zhiliang Ku, Guifang Han, David Giovanni, Nripan Mathews, Hong Jin Fan, and Tze Chien Sum. Discerning the surface and bulk recombination kinetics of organic–inorganic halide perovskite single crystals. *Adv. Energy Mater.*, 6(14):1600551, 2016.

[175] Michal Baranowski and Paulina Plochocka. Excitons in metal-halide perovskites. *Adv. Energy Mater.*, 10(26):1903659, 2020.

[176] Ye Yang, Mengjin Yang, Kai Zhu, Justin C Johnson, Joseph J Berry, Jao Van De Lagemaat, and Matthew C Beard. Large polarization-dependent exciton optical stark effect in lead iodide perovskites. *Nat. Commun.*, 7(1):12613, 2016.

[177] Verena A Hintermayr, Lakshminarayana Polavarapu, Alexander S Urban, and Jochen Feldmann. Accelerated carrier relaxation through reduced coulomb screening in two-dimensional halide perovskite nanoplatelets. *ACS Nano*, 12(10):10151–10158, 2018.

[178] Feng Chen, Can Zhu, Chunxiang Xu, Peng Fan, Feifei Qin, A Gowri Manohari, Junfeng Lu, Zengliang Shi, Qingyu Xu, and Anlian Pan. Crystal structure and electron transition underlying photoluminescence of methylammonium lead bromide perovskites. *J. Mater. Chem. C*, 5(31):7739–7745, 2017.

[179] Giselle A Elbaz, Daniel B Straus, Octavi E Semonin, Trevor D Hull, Daniel W Paley, Philip Kim, Jonathan S Owen, Cherie R Kagan, and Xavier Roy. Unbalanced hole and electron diffusion in lead bromide perovskites. *Nano Lett.*, 17(3):1727–1732, 2017.

[180] Bernard Wenger, Pabitra K Nayak, Xiaoming Wen, Sameer V Kesava, Nakita K Noel, and Henry J Snaith. Consolidation of the optoelectronic properties of ch 3 nh 3 pbbr 3 perovskite single crystals. *Nat. Commun.*, 8(1):1–10, 2017.

[181] Ye Yang, Mengjin Yang, Zhen Li, Ryan Crisp, Kai Zhu, and Matthew C Beard. Comparison of recombination dynamics in ch3nh3pbbr3 and ch3nh3pbi3 perovskite films: influence of exciton binding energy. *J. Phys. Chem. Lett.*, 6(23):4688–4692, 2015.

[182] Yiting Liu, Haizhou Lu, Jiaxin Niu, Huotian Zhang, Shitao Lou, Chunlei Gao, Yiqiang Zhan, Xiaolei Zhang, Qingyuan Jin, and Lirong Zheng. Temperature-dependent photoluminescence spectra and decay dynamics of mapbbr3 and mapbi3 thin films. *AIP Adv.*, 8(9):095108, 2018.

[183] Shuai Zhang, Qiuyu Shang, Wenna Du, Jia Shi, Zhiyong Wu, Yang Mi, Jie Chen, Fengjing Liu, Yuanzheng Li, Mei Liu, et al. Strong exciton–photon coupling in hybrid inorganic–organic perovskite micro/nanowires. *Adv. Opt. Mater.*, 6(2):1701032, 2018.

[184] Charles L Braun. Electric field assisted dissociation of charge transfer states as a mechanism of photocarrier production. *J. Chem. Phys.*, 80(9):4157–4161, 1984.

[185] Roger Häusermann, Evelyne Knapp, Michael Moos, Nils A Reinke, Thomas Flatz, and Beat Ruhstaller. Coupled optoelectronic simulation of organic bulk-heterojunction solar cells: Parameter extraction and sensitivity analysis. *J. Appl. Phys.*, 106(10):104507, 2009.

[186] Raymond Fuoss and Filippo Accascina. *Electrolytic conductance*. Interscience Publishers, 1959.

[187] Meghnad N Saha. On a physical theory of stellar spectra. *Proc. R. Soc. London, Ser. A*, 99(697):135–153, 1921.

[188] Fabrizio Mariano, Arianna Cretì, Luigi Carbone, Armando Genco, Stefania D'Agostino, Sonia Carallo, Giovanni Montagna, Mauro Lomascolo, and Marco Mazzeo. The enhancement of excitonic emission crossing saha equilibrium in trap passivated ch3nh3pbbr3 perovskite. *Commun. Phys.*, 3(1):1–10, 2020.

[189] Zhengwei Xu, Xingxing Jiang, Hua-peng Cai, Keqiu Chen, Xiaolong Yao, and Yexin Feng. Toward a general understanding of exciton self-trapping in metal halide perovskites. *The Journal of Physical Chemistry Letters*, 12(43):10472–10478, 2021.

[190] Lei Zhou, Jin-Feng Liao, and Dai-Bin Kuang. An overview for zero-dimensional broadband emissive metal-halide single crystals. *Advanced Optical Materials*, 9(17):2100544, 2021.

[191] Chunyang Yin, Liyang Chen, Nan Song, Yan Lv, Fengrui Hu, Chun Sun, W Yu William, Chunfeng Zhang, Xiaoyong Wang, Yu Zhang, et al. Bright-exciton fine-structure splittings in single perovskite nanocrystals. *Physical Review Letters*, 119(2):026401, 2017.

[192] Michael A Becker, Roman Vaxenburg, Georgian Nedelcu, Peter C Sercel, Andrew Shabaev, Michael J Mehl, John G Michopoulos, Samuel G Lambrakos, Noam Bernstein, John L Lyons, et al. Bright triplet excitons in caesium lead halide perovskites. *Nature*, 553(7687):189, 2018.

[193] Philippe Tamarat, Maryna I Bodnarchuk, Jean-Baptiste Trebbia, Rolf Erni, Maksym V Kovalenko, Jacky Even, and Brahim Lounis. The ground exciton state of formamidinium lead bromide perovskite nanocrystals is a singlet dark state. *Nature Materials*, 18(7):717–724, 2019.

[194] Hélène Seiler, Daniela Zahn, Victoria CA Taylor, Maryna I Bodnarchuk, Yoav William Windsor, Maksym V Kovalenko, and Ralph Ernstorfer. Direct observation of ultrafast lattice distortions during exciton–polaron formation in lead halide perovskite nanocrystals. *ACS nano*, 2022.

[195] Colin D Sonnichsen, Dallas P Strandell, Patrick J Brosseau, and Patanjali Kambhampati. Polaronic quantum confinement in bulk cspb br 3 perovskite crystals revealed by state-resolved pump/probe spectroscopy. *Physical Review Research*, 3(2):023147, 2021.

[196] Kenichiro Tanaka, Ryuichi Ozawa, Tsutomu Umebayashi, Keisuke Asai, Kazuhiro Ema, and Takashi Kondo. One-dimensional excitons in inorganic–organic self-organized quantum-wire crystals [nh2c (i)= nh2] 3pbi5 and [ch3sc (= nh2) nh2] 3pbi5. *Physica E: Low-dimensional Systems and Nanostructures*, 25(4):378–383, 2005.

[197] Paolo Giannozzi, Stefano Baroni, Nila Bonini, Matteo Calandra, Roberto Car, Carlo Cavazzoni, Davide Ceresoli, Guido L Chiarotti, Matteo Cococcioni, Ismaila Dabo, Andrea Dal Corso, Stefano de Gironcoli, Stefano Fabris, Guido Fratesi, Ralph Gebauer, Uwe Gerstmann, Christos Gougoussis, Anton Kokalj, Michele Lazzeri, Layla Martin-Samos, Nicola Marzari, Francesco Mauri, Riccardo Mazzarello, Stefano Paolini, Alfredo Pasquarello, Lorenzo Paulatto, Carlo Sbraccia, Sandro Scandolo, Gabriele Sclauzero, Ari P Seitsonen, Alexander Smogunov, Paolo Umari, and Renata M Wentzcovitch. QUANTUM ESPRESSO: a modular and open-source software project for quantum simulations of materials. *J. Phys.: Condens. Matter*, 21(39):395502, 2009.

[198] John P. Perdew, Kieron Burke, and Matthias Ernzerhof. Generalized gradient approximation made simple. *Phys. Rev. Lett.*, 77:3865–3868, 1996.

[199] Kuntal Talit and David A. Strubbe. Stress effects on vibrational spectra of a cubic hybrid perovskite: A probe of local strain. *The Journal of Physical Chemistry C*, 124(50):27287–27299, 2020.

[200] Sujin Lee, Rijan Karkee, Azza Ben-Akacha, Derek Luong, JS Winfred, Xinsong Lin, David A Strubbe, and Biwu Ma. Bulk assembly of organic metal halide nanoribbons. *arXiv preprint arXiv:2211.07597*, 2022.

[201] Jack Deslippe, Georgy Samsonidze, David A.Strubbe, Manish Jain, Marvin L.Cohen, and Steven G.Louie. Berkeleygw: A massively parallel computer package for the calculation of the quasiparticle and optical properties of materials and nanostructures. *Comp. Phys. Commun.*, 183:1269–1289, 2012.

[202] J.-C. Blancon, A. V. Stier, H. Tsai, W. Nie, C. C. Stoumpos, B. Traoré, L. Pedesseau, M. Kepenekian, F. Katsutani, G. T. Noe, J. Kono, S. Tretiak, S. A. Crooker, C. Katan, M. G. Kanatzidis, J. J. Crochet, J. Even, and A. D. Mohite. Scaling law for excitons in 2d perovskite quantum wells. *Nat. Commun.*, 9:2254, 2018.

[203] Ying Han, Yiwei Dong, Hao Gu, Teng Cheng, Yipeng Xie, Yufan Lin, Guichuan Xing, Jun Yin, and Bin-Bin Cui. Efficient room-temperature phosphorescence of 1d organic–inorganic hybrid metal halides. *Small Structures*, page 2200110, 2022.

[204] Jun Xu, Sai Li, Chaochao Qin, Zongjing Feng, and Yaping Du. Identification of singlet self-trapped excitons in a new family of white-light-emitting zero-dimensional compounds. *The Journal of Physical Chemistry C*, 124(21):11625–11630, 2020.

[205] Viktoriia Morad, Yevhen Shynkarenko, Sergii Yakunin, Alexandra Brumberg, Richard D Schaller, and Maksym V Kovalenko. Disphenoidal zero-dimensional lead, tin, and germanium halides: Highly emissive singlet and triplet self-trapped excitons and x-ray scintillation. *Journal of the American Chemical Society*, 141(25):9764–9768, 2019.

[206] Yuyu Jing, Ying Liu, Jing Zhao, and Zhiguo Xia. Sb3+ doping-induced triplet self-trapped excitons emission in lead-free cs2sncl6 nanocrystals. *The Journal of Physical Chemistry Letters*, 10(23):7439–7444, 2019.

[207] Zhiwei Ma, Qian Li, Jiajun Luo, Shunran Li, Laizhi Sui, Dianlong Zhao, Kaijun Yuan, Guanjun Xiao, Jiang Tang, Zewei Quan, et al. Pressure-driven reverse intersystem crossing: New path toward bright deep-blue emission of lead-free halide double perovskites. *Journal of the American Chemical Society*, 143(37):15176–15184, 2021.

[208] Alyssa Kostadinov-Mutzafi, Jenya Tilchin, Arthur Shapiro, Dmitry N Dirin, Maksym V Kovalenko, Liang Z Tan, and Efrat Lifshitz. Impact of anisotropy in spin-orbit coupling on the magneto-optical properties of bulk lead halide perovskites. *Physical Review B*, 106(3):035303, 2022.

[209] Zhenqi Hua, Azza Ben-Akacha, Qingquan He, Tianhan Liu, Gillian Boyce, Margaret van Deventer, Xinsong Lin, Hanwei Gao, Biwu Ma, and Peng Xiong. Intrinsic ion migration dynamics in a one-dimensional organic metal halide hybrid. *ACS Energy Letters*, 7:3753–3760, 2022.

[210] Smritakshi P Sarmah, Victor M Burlakov, Emre Yengel, Banavoth Murali, Erkki Alarousu, Ahmed M El-Zohry, Chen Yang, Mohd S Alias, Ayan A Zhumekenov, Makhsud I Saidaminov, et al. Double charged surface layers in lead halide perovskite crystals. *Nano Letters*, 17(3):2021–2027, 2017.

[211] Michael Seitz, Alvaro J Magdaleno, Nerea Alcázar-Cano, Marc Meléndez, Tim J Lubbers, Sanne W Walraven, Sahar Pakdel, Elsa Prada, Rafael Delgado-Buscalioni, and Ferry Prins. Exciton diffusion in two-dimensional metal-halide perovskites. *Nature communications*, 11(1):2035, 2020.

[212] Alexander Urich, Karl Unterrainer, and Thomas Mueller. Intrinsic response time of graphene photodetectors. *Nano Letters*, 11(7):2804–2808, 2011.

[213] Dong Sun, Grant Aivazian, Aaron M Jones, Jason S Ross, Wang Yao, David Cobden, and Xiaodong Xu. Ultrafast hot-carrier-dominated photocurrent in graphene. *Nature Nanotechnology*, 7(2):114, 2012.

[214] Byung Hee Son, Jae-Ku Park, Jung Taek Hong, Ji-Yong Park, Soonil Lee, and Yeong Hwan Ahn. Imaging ultrafast carrier transport in nanoscale field-effect transistors. *ACS nano*, 8(11):11361–11368, 2014.

[215] Yasuhiro Yamada, Hirofumi Mino, Takuya Kawahara, Kenichi Oto, Hidekatsu Suzuura, and Yoshihiko Kanemitsu. Polaron masses in $ch_3nh_3PbX_3$ perovskites determined by landau level spectroscopy in low magnetic fields. *Phys. Rev. Lett.*, 126:237401, Jun 2021.

[216] Sigismund Teunis Alexander George Melissen, Frédéric Labat, Philippe Sautet, and Tangui Le Bahers. Electronic properties of pbx3ch3nh3 (x = cl, br, i) compounds for photovoltaic and photocatalytic applications. *Phys. Chem. Chem. Phys.*, 17:2199–2209, 2015.

[217] DR Hamann. Optimized norm-conserving vanderbilt pseudopotentials. *Physical Review B*, 88(8):085117, 2013.

[218] M.J. van Setten, M. Giantomassi, E. Bousquet, M.J. Verstraete, D.R. Hamann, X. Gonze, and G.-M. Rignanese. The pseudodojo: Training and grading a 85 element optimized norm-conserving pseudopotential table. *Computer Physics Communications*, 226:39–54, 2018.

[219] Bradford A Barker, Jack Deslippe, Johannes Lischner, Manish Jain, Oleg V Yazyev, David A Strubbe, and Steven G Louie. Spinor g w/bethe-salpeter calculations in berkeleygw: Implementation, symmetries, benchmarking, and performance. *Physical Review B*, 106(11):115127, 2022.

Appendix A: $MAPbI_3$

A.1 Appended Figures: $MAPbI_3$

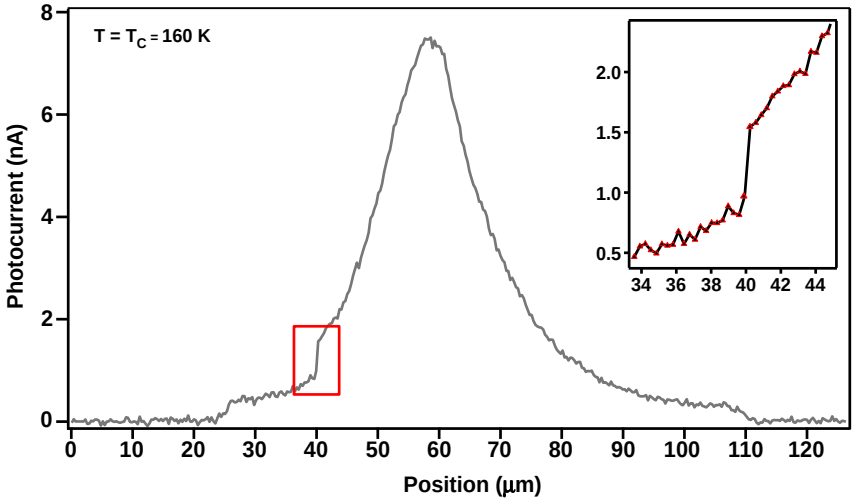

Figure A.1: SPCM profile from device in **Figure 3.2** taken exactly at T_c. Sharp jump in photocurrent (boxed in red) indicates moment of phase change during the scan. Laser scanned sample from left to right at 50 Hz over 400 data points. Since the phase change occurred between 2 points, this implies the transition probably completed in 10 $\pm$5 ms. Inset: Zoom-in of phase change jump.

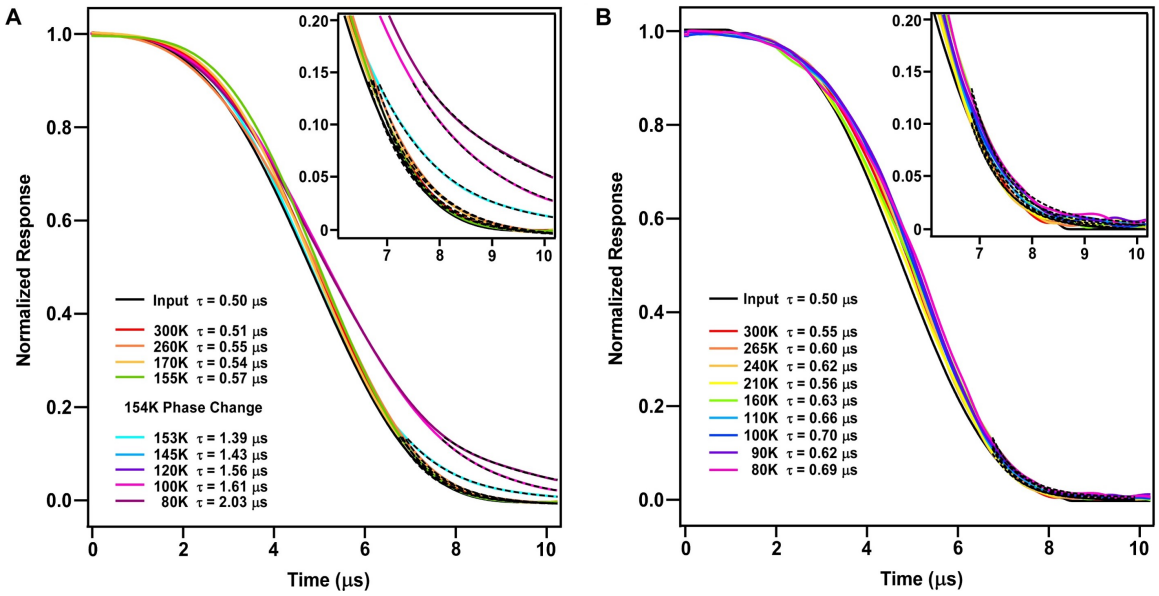

Figure A.2: (A) Time traces of photocurrent measured by an oscilloscope at various temperatures for the device in **Figure 3.2**. Lifetime is extracted from fitting the photocurrent decay after the excitation intensity drops toward zero. The maximum photoexcitation is approximately 1 μW / μm^2 at 532 nm focused onto the sample surface while a 3 V bias is applied. (B) Time traces of photocurrent for another device, measured at the same intensity as during SPCM measurements. Importantly, even when L_D is long (80 K) and laser intensity is low, τ is still short, again leading to large mobility values.

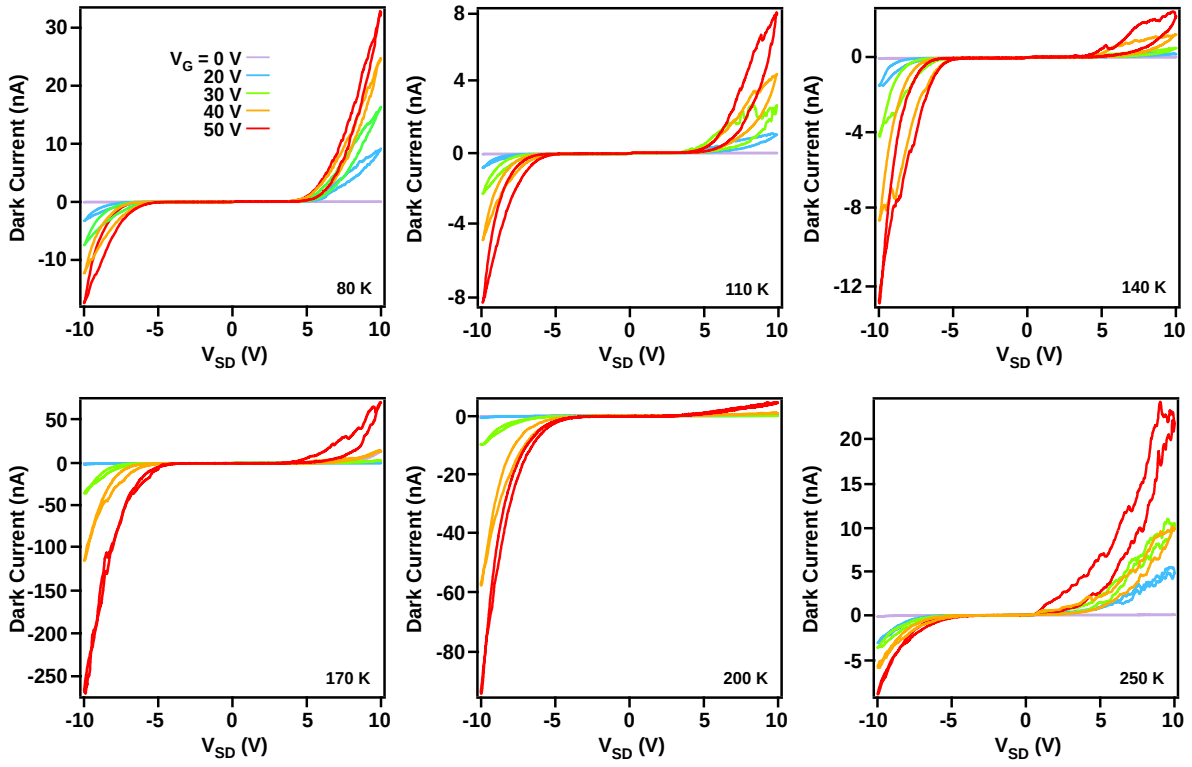

Figure A.3: Dark current-voltage (I-V_{SD}) curves as a function of V_G at various temperatures.

Appendix B: $MAPbBr_3$

B.2 Appended Figures: $MAPbBr_3$

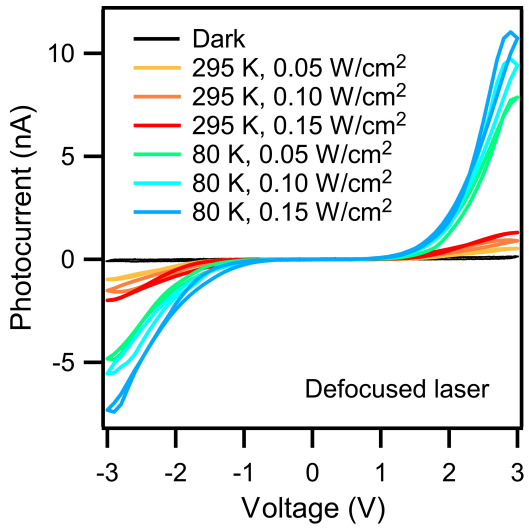

Figure B.4: Current-voltage curves. Current vs. source-drain voltage curves at various global illumination intensities, at 295 K and 80 K, respectively. The nonlinear curves indicate a large contact barrier.

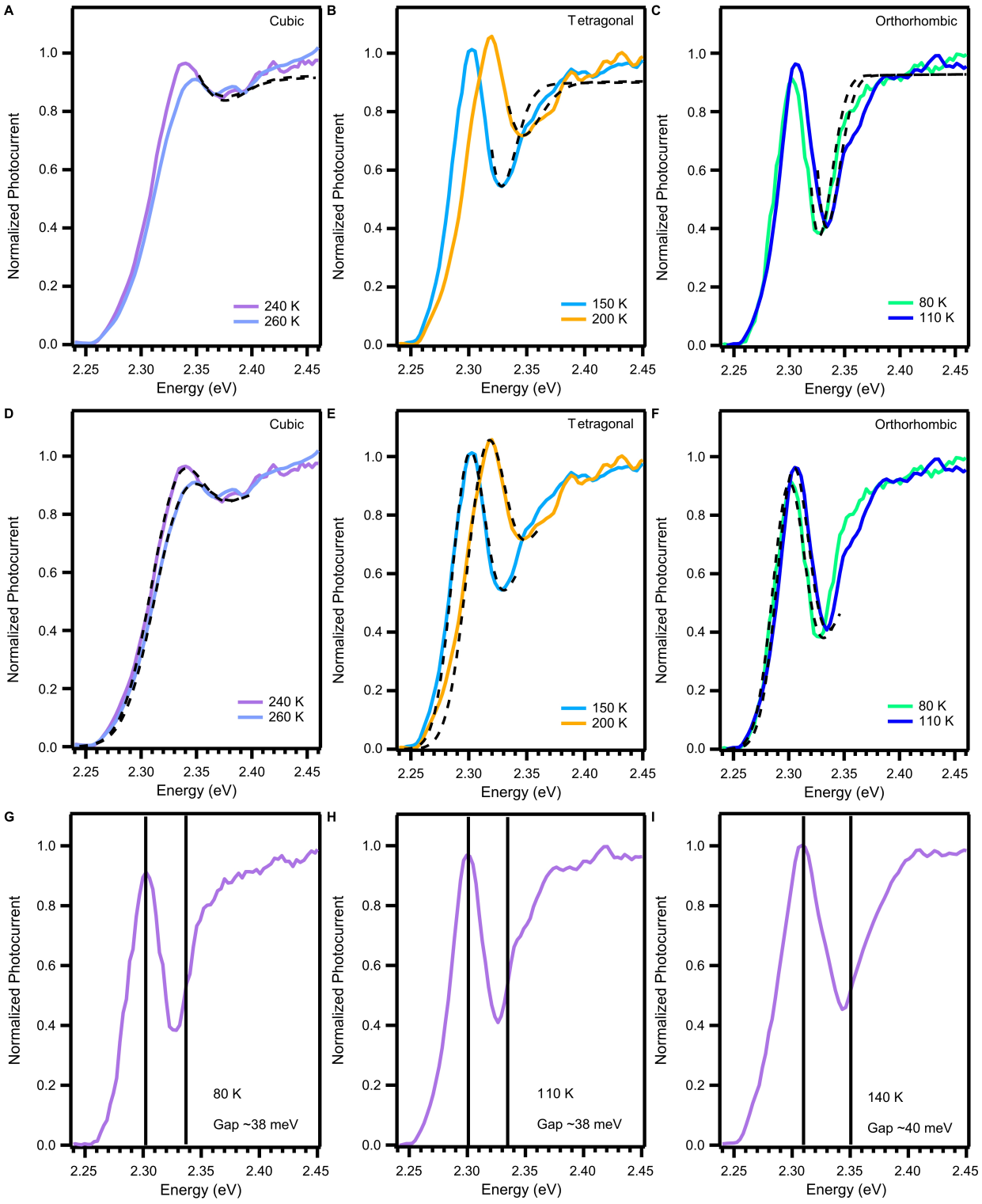

Figure B.5: Various Elliott fittings. (A-C) High energy fit examples. (D-F) Low energy fit examples. (G-I) E_B estimated from the energy difference between the exciton peak and the half height of the continuum edge.

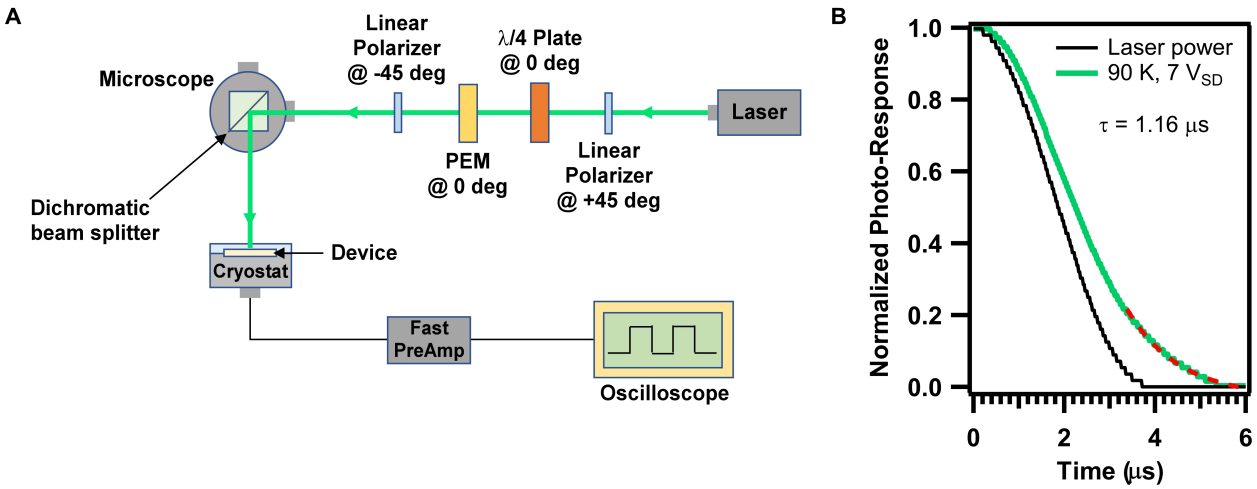

Figure B.6: Transient Photocurrent Measurement. We use a combination of a photoelastic modulator (PEM), quarter waveplate, and two crossed linear polarizers as an optical chopper to modulate the light intensity at 50 kHz with a light intensity decay of about 0.5 μs. A high-speed amplifier (Femto DHPCA-100) and a digital oscilloscope were used to measure the transient photocurrent.Time-resolved photocurrent (TRPC) measurements. (A) TRPC setup by using a photoelastic modulator (PEM) based chopper. (B) Transient photocurrent measurement at 90 K and $V_{SD} = 7$ V. The black curve is the laser power change over time. The dashed red curve is the exponential fitting of the photocurrent decay after the light is completely turned off.

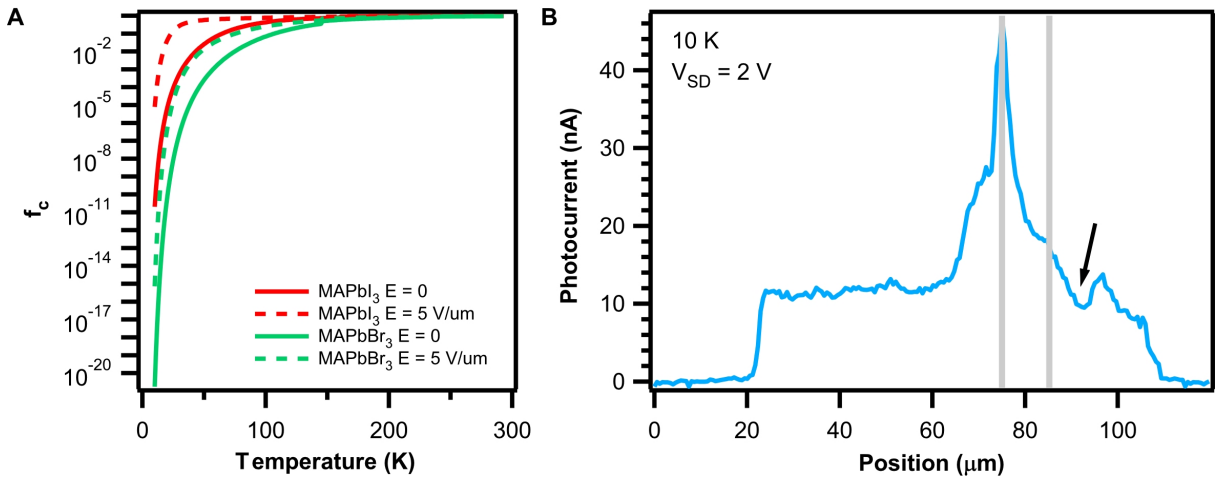

Figure B.7: (A) Calculated free carrier fraction (f_c) as a function of temperature. f_c is less than 10^{-19} at 10 K. (B) Long photocurrent decay length is experimentally observed with SPCM at 10 K. Black arrow indicates the position of a surface crack that formed in the crystal likely due to the thermal expansion coefficient mismatch and the phase transition at the very low temperature, which caused a dip in the photocurrent.

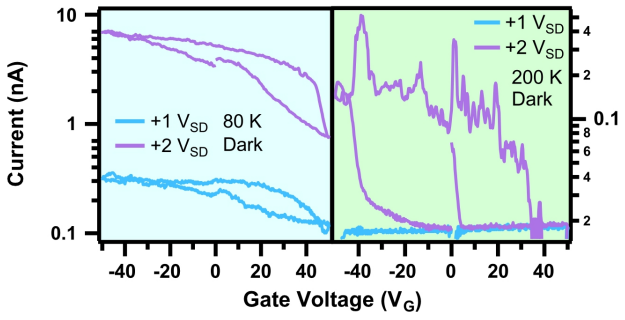

Figure B.8: I-V_G plots from another device, showing typical p-type behavior that was observed in most samples. V_G is scanned at 2.5 V/s.

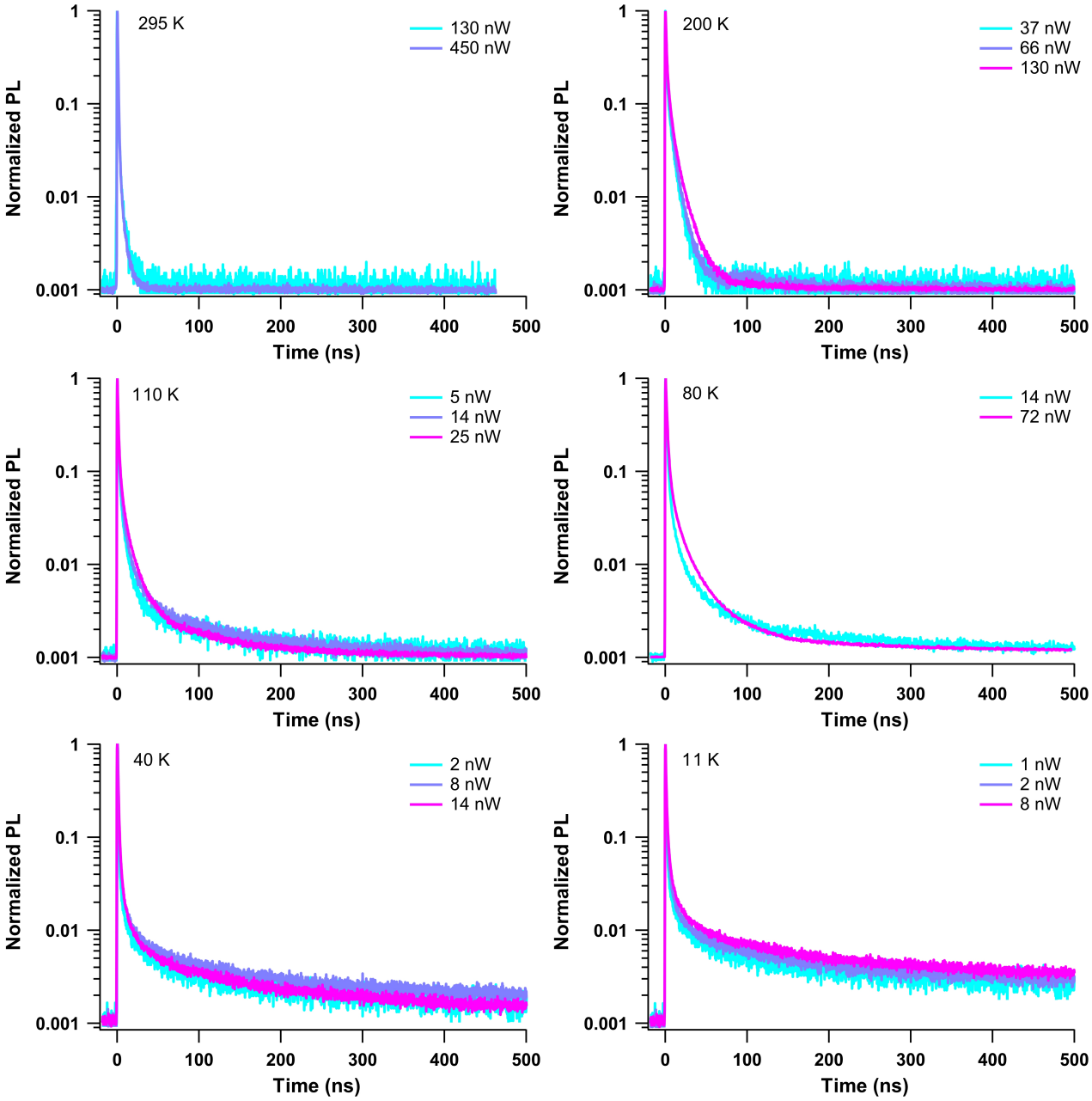

Figure B.9: Laser power dependence of TRPL measurements at various temperatures. TRPL lifetimes showed little to no power dependence across the full range of temperatures, indicating monomolecular recombination dominates in the intensity range used here (0.13 - 57 W/cm^2). Lower intensities had to be used at low temperature due to rapidly increasing PL emission over-saturating the detection system.

B.3 Temperature and Field-Dependent Exciton Fraction

We calculate the fraction of excitons over the total photoexcited carriers (f_{ex}) in both $MAPbI_3$ and $MAPbBr_3$ (**Figure 3.10F** in Chapter 3). The Saha equation[57] is used to calculate the exciton dissociation constant, $K(0) = np/n_x = \lambda^{-3}e^{-E_B/k_BT}$, where n_x is the exciton density, $\lambda = h/\sqrt{2\pi m_x^* k_B T}$ is the thermal de Broglie wavelength, and $m_x^* = m_e m_h/(m_e + m_h)$ is the effective mass of an exciton. The exciton fraction is given by $f_{ex} = n_x/(n_x + n) = p/[K(0) + p]$ for p-type devices at moderate laser excitation intensity as used in our experimental conditions. The exciton fraction increases exponentially as temperature decreases and the additional abrupt increases are caused by the sudden change of exciton binding energy across the phase transitions. f_{ex} is larger in $MAPbBr_3$ and saturates at 100% at 80 K. In addition, we also calculate f_{ex} at the contact metal junction. Because of the large electric field (estimated to be 5 V/μm) in the depletion region, excitons are more easily dissociated into free carriers. The dissociation constant is enhanced by a factor of $K(E)/K(0) = \frac{J_1(2\sqrt{-2b})}{\sqrt{-2b}}$, where J_1 is the Bessel function of order one and $b = \frac{e^3 E}{8\pi\epsilon_r\epsilon_0 k_B^2 T^2}$ [53] [186].

We also plot the free carrier fraction $f_c = 1 - f_{ex}$ in **Appendix Figure B.7A**. The free carrier fraction is about 10^{-2} at 80 K and 10^{-19} at 10 K. Such low free carrier concentrations at low temperatures indicate that the free carrier diffusion unlikely account for the observed nonlocal photocurrent. Furthermore, we performed additional SPCM measurements at 10 K, where the diffusion length remains extremely long (**Appendix Figure B.7B**). Hence, it is evident that excitons are responsible for the observed long diffusion lengths at low temperatures.

Symbol	Physical meaning	Orthorhombic	Tetragonal	Cubic
m_e^*	electron effective mass [215]	0.24	0.24	0.24
m_h^*	hole effective mass [215]	0.30	0.30	0.30
m_x^*	exciton effective mass	0.13	0.13	0.13
ϵ_0	static dielectric constant [112]	25	25	30
ϵ_∞	high frequency dielectric constant [216]	4.4	4.4	4.4
$\hbar\omega_{LO}$ (meV)	LO phonon energy [161]	8	15.3	15.3
E_B (meV)	exciton binding energy	40.5	25.9	23.6
a_0 (nm)	exciton Bohr radius	1.86	1.99	2.00
R_e (nm)	electron polaron radius	4.45	3.22	3.22
R_h (nm)	hole polaron radius	3.98	2.88	2.88
R_x (nm)	exciton polaron radius	5.98	4.32	4.32

Table 1: Physical parameters used in the calculation of exciton fractions and scattering rates in $MAPbBr_3$. The values of the last five quantities (exciton binding energy, exciton Bohr radius, and the polaron radii) are calculated by using a polaronic exciton model [157]. The γ values in the main text are calculated using the orthorhombic phase parameters. As the photocurrent decay length is determined by the minority carrier diffusion in absence of excitons, we used the electron (hole) polaron radius for p (n) type $MAPbBr_3$ ($MAPbI_3$).

Appendix C: $C_4N_2H_{14}PbBr_4$

C.4 Appended Figures: $C_4N_2H_{14}PbBr_4$

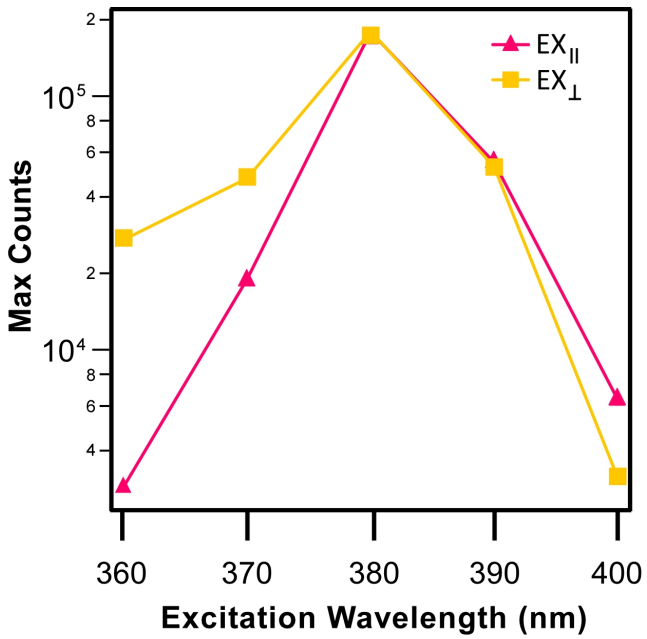

Figure C.10: Total PL emission counts as a function of excitation wavelength and orthogonal excitation polarizations. All PL counts are normalized to photoexcitation power, measured in Sample #4. Note that the trend is similar to the data collected from Sample #3, as shown in **Figure 4.2** in Chapter 4.

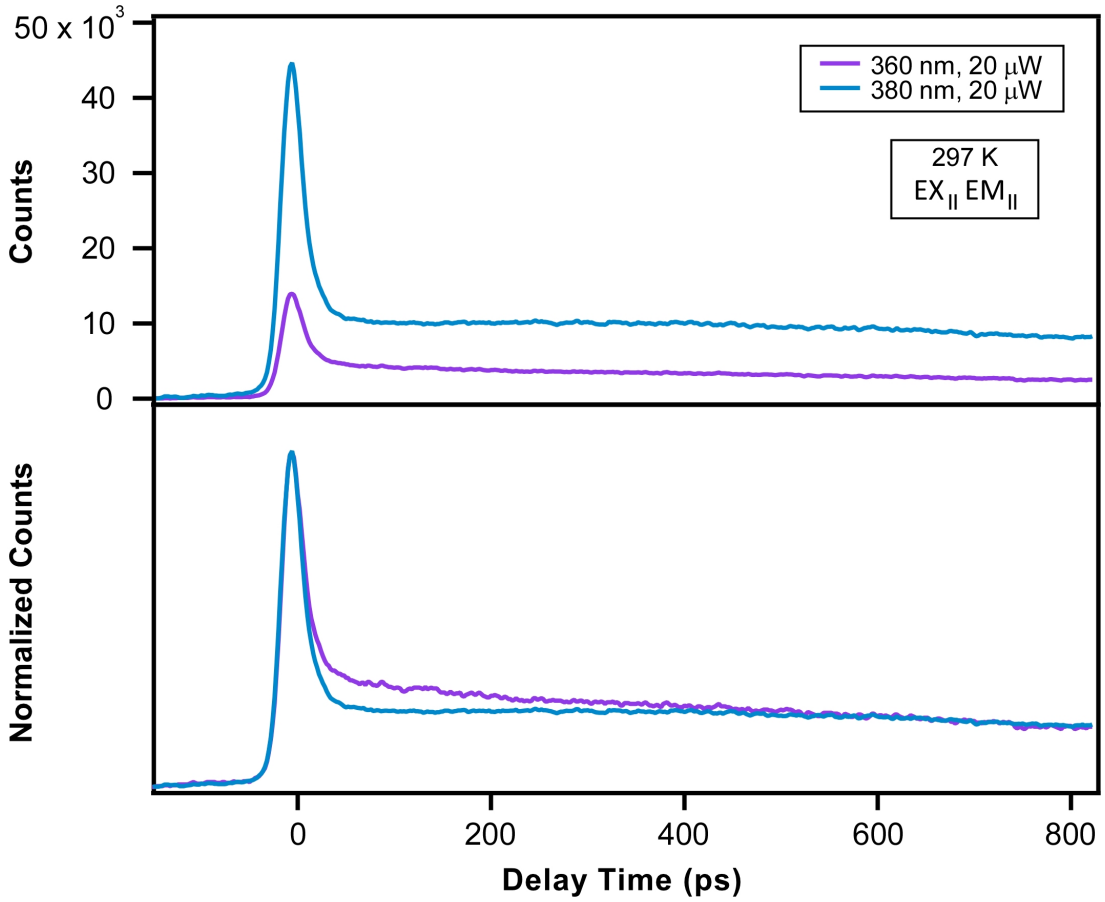

Figure C.11: Comparison of PL counts as a function of delay time after 360 nm and 380 nm pulsed excitation at room temperature (Sample #5).

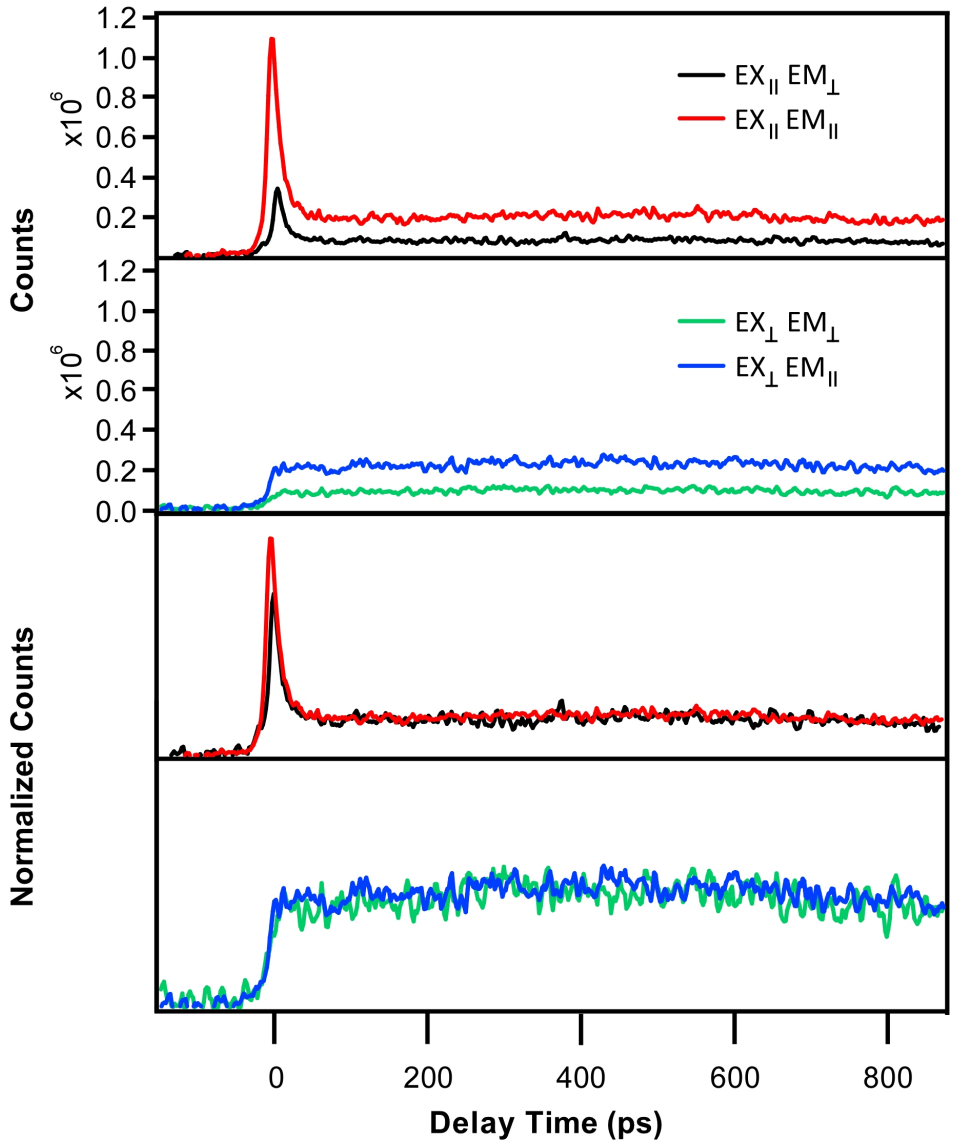

Figure C.12: PL counts as a function of delay time after 380 nm pulsed excitation at room temperature (Sample #4) with different excitation and emission polarization configurations. The trend is similar to the data taken from Sample #5 shown in **Figure 4.4** in Chapter 4, though a small initial sharp decay peak is also observed for perpendicular emission polarization in this sample.

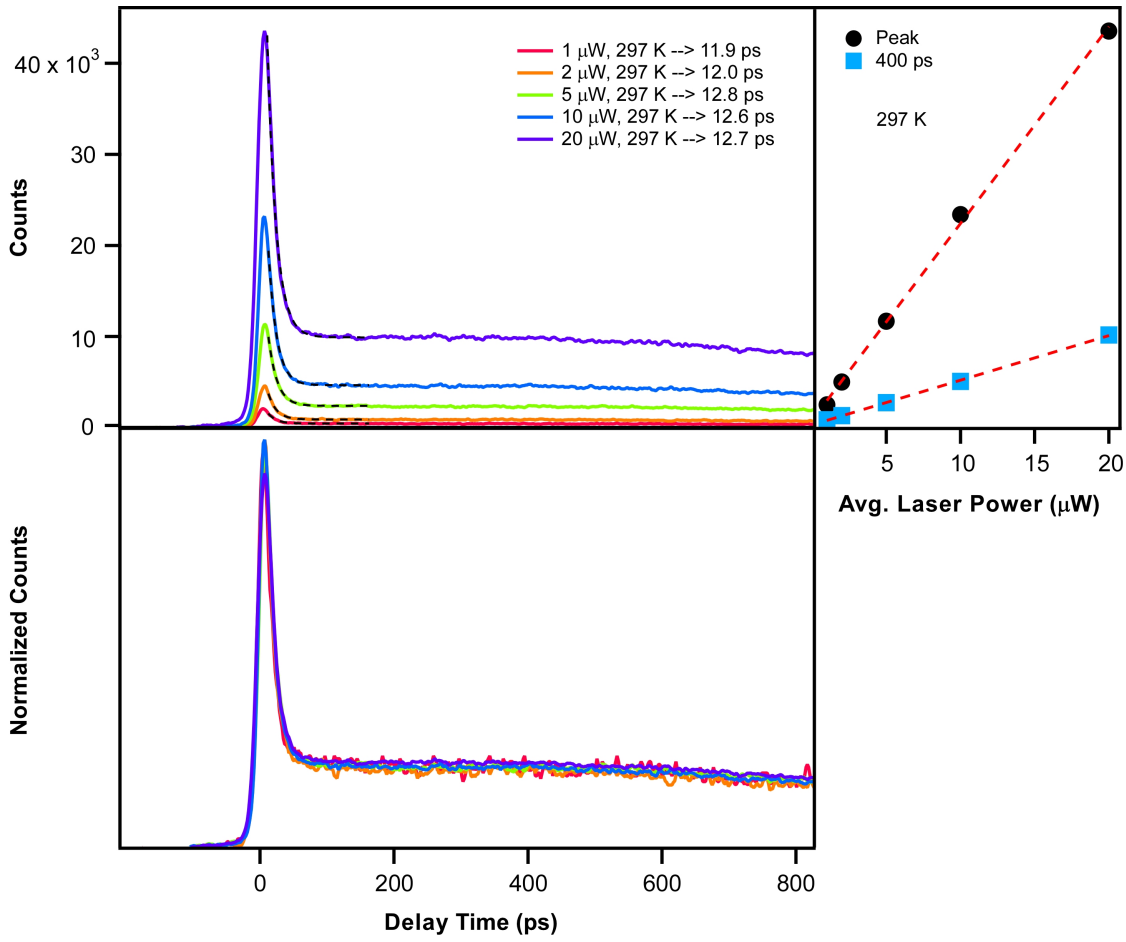

Figure C.13: Left - PL counts as a function of delay time after 380 nm pulsed excitation at room temperature (Sample #5) under varying laser intensities. The fittings correspond to decay times for the sharp feature and are listed in the legend. Right - Total counts at peak as well as 400 ps later as a function of average laser power. Red dashed lines are linear fittings.

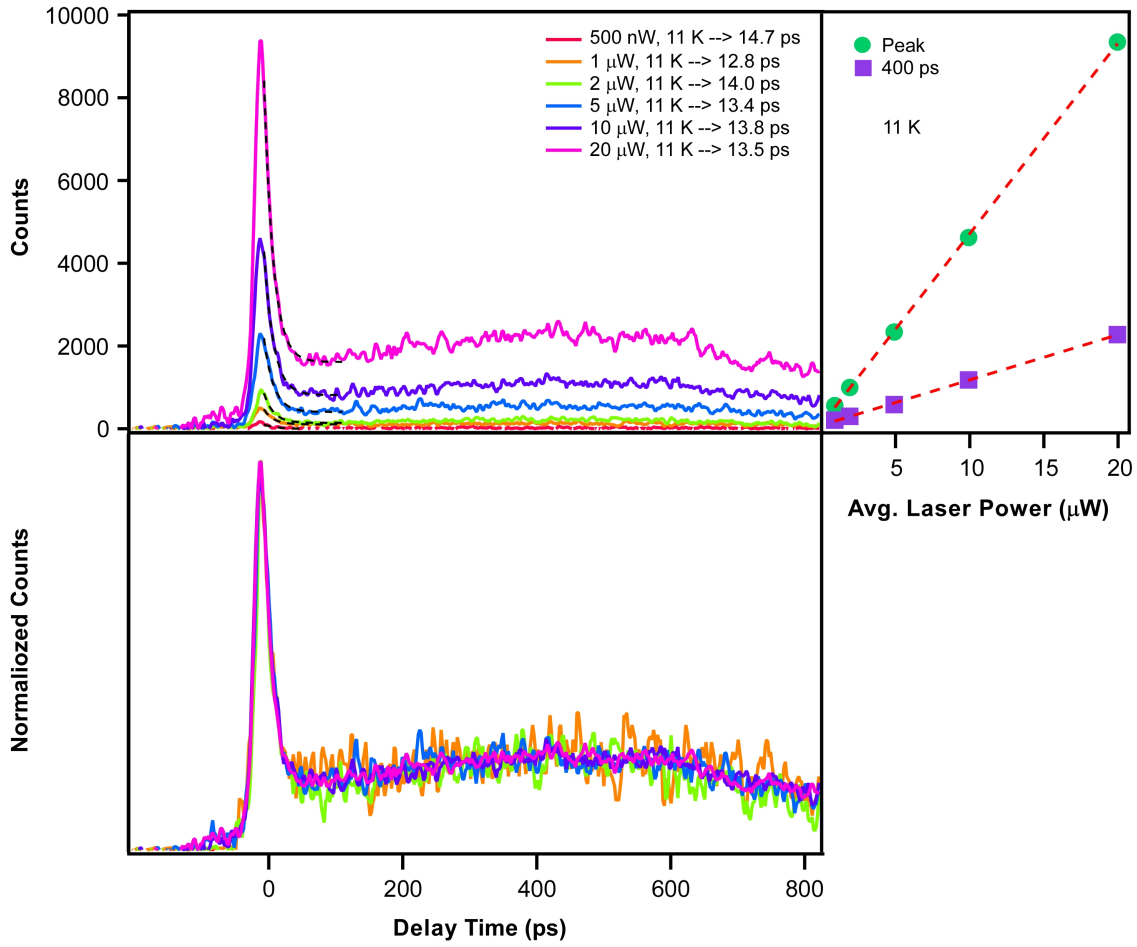

Figure C.14: Left - PL counts as a function of delay time after 380 nm pulsed excitation at 11 K (Sample #5) under varying laser intensities. The fittings correspond to decay times for the sharp feature and are listed in the legend. Right - Total counts at peak as well as 400 ps later as a function of average laser power. Red dashed lines are linear fittings.

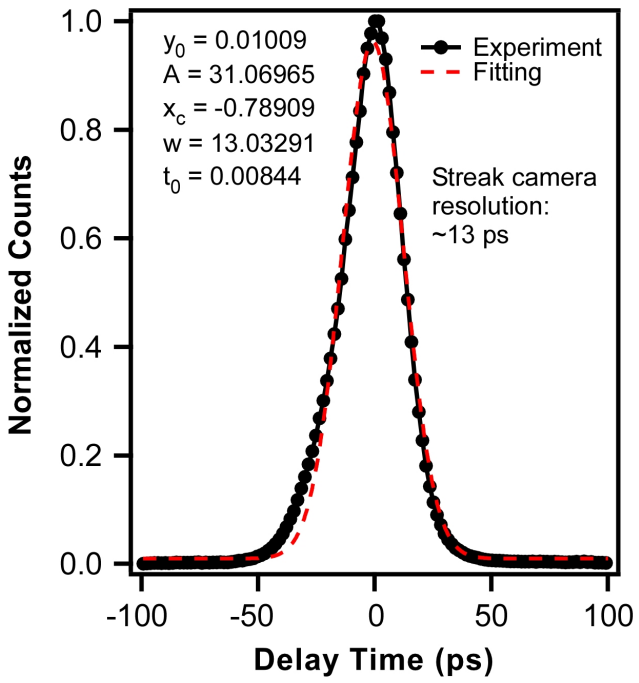

Figure C.15: Streak camera temporal resolution calibration, obtained by measuring the input laser pulse. Fitting equation: $y = y_0 + (A/t_0) * exp[0.5 * (w/t_0)^2 - (x - x_c)/t_0] * (erf(z/\sqrt{(}2)) + 1)/2$, where $z = (x - x_c)/w - w/t_0$. The fitting parameter w is the estimated temporal resolution in ps.

C.5 Simulation and Modeling

ONCV pseudopotentials[217] from PseudoDojo[218] were used. Most calculations were scalar relativistic. A wave-function energy cutoff of 816 eV and a 3 x 3 x 3 half-shifted k-grid were used for self-consistent field (SCF) calculations. Forces and stresses were relaxed below 10^{-4} Ry bohr^{-1} and 0.1 kbar, respectively. Density of states calculations used a 20 x 20 x 20 half-shifted k-grid and a broadening of 0.05 eV. For BerkeleyGW calculations, we found that 300 empty bands, a 4 x 4 x 4 q-grid, and a 204 eV screened-Coulomb cutoff converged GW quasiparticle corrections near the gap to within 100 meV. Optical absorption spectra computed with the Bethe-Salpeter equation in BerkeleyGW use 18 occupied states and 24 unoccupied states and an 8 x 8 x 8 fine k-grid and are plotted with 0.1 eV Gaussian broadening. To obtain a simple spin-orbit correction, fully relativistic DFT calculations were performed on the same structure. The band-structure had a gap reduced by 0.5 eV. This difference was then applied as a rigid shift to the GW, RPA, and BSE results, motivated by the typical finding that energy shifts due to spin-orbit are similar in DFT and GW.[219] Similarly, a rigid shift to the DFT PDOS was applied with the sum of the gap corrections from GW (+1.30 eV) and spin-orbit coupling.